Stellar elemental abundance determination using a Fabry-Pérot Interferometer

A thesis
submitted in partial fulfilment
of the requirements for the Degree
of
Masters of Science in Astronomy
in the
University of Canterbury

by

Jeffrey Simpson

University of Canterbury
August 3, 2009

Abstract

The Fabry-Pérot interferometer (FPI) was investigated as a potential tool for determining stellar elemental abundances. The FPI is a tunable narrow-band filter that makes it possible to obtain hundreds of stellar spectra simultaneously without the overhead associated with other multi-object spectroscopy techniques. This thesis used simulations and previously acquired data to investigate the FPI and develop data reduction techniques.

Using observations of a CaII spectral line, an algorithm was created for fitting a Voigt profile to the spectrum segments. The values for radial velocity & equivalent width were compared to the values found by the group who supplied the data and found to agree well for the radial velocity values but there was some definite scatter in the equivalent width. These differences are attributed to different placement of the continuum level in the spectra.

This curve-fitting script was modified to allow the fitting of synthetic spectra to simulated data. In this way it was possible to investigate how precise the abundance determination will be using the Robert Stobie Spectrograph's FPI mode. Large simulations showed that it will be possible to determine abundances to uncertainties of ± 0.1 dex. This is an excellent result and should mean that future work using the FPI will give the results desired for large-scale s-process elemental abundance determination in globular cluster stars.

Acknowledgements

First of all I would like to thank my supervisor, Associate Professor Peter Cottrell. He has helped immensely throughout this project, especially through the changing aims of this reseach.

Naseem Rangwala and Ted Williams of Rutgers kindly provided data and expertise. This data formed a large portion of this thesis and will prove invaluable for later research in this area. They also answered many questions that I had about the Fabry-Pérot interferometer.

The Department of Physics & Astronomy provided me with financial support which meant I could undertake this research without resorting to actually having to get a job.

Lastly, but by no means least, I would like to thank Rachel who proofread this thesis for me the day before it was due to be submitted. Thank you for finding all those commas in the wrong places.

Copyright and licensing

Contents

List of Figures

List of Tables

Chapter 1

Introduction

Globular clusters contain some of the oldest stars in the Universe, with ages often greater than 10 billion years. They consist of 10^4–10^6 population II stars in a radius of ~ 10 parsecs. The simplistic theory of their formation is that all the stars formed from the same cloud of gas and dust at about the same time. Naively, this could lead to the conclusion that the only difference between individual stars should be their masses.

But there is much evidence in the literature showing star-to-star variations of elemental abundances in globular clusters (e.g. Sneden 1999, Gratton et al. 2004, Cohen et al. 2005). Of most interest for the research of this thesis is Wylie et al. (2006), who found that the s-process elements yttrium, zirconium, neodymium and lanthanum are enhanced in a small sample of the giant stars in the globular cluster 47 Tuc. This is a surprising result, since there is no mechanism for creating such enhancements in these stars, meaning these enhancements must have been present in the primordial gas cloud from which the cluster formed.

In order to further explore these abundance variations, spectroscopic observations are required of a large sample of stars. Since telescope time is often at a premium, it is preferable to be able to measure many stars simultaneously.

One of the methods for doing this, currently utilized at the Southern African Large Telescope (SALT), is the multi-object spectroscopy mode of the Robert Stobie Spectrograph (RSS). To undertake this, one images the field photometrically and identifies the objects of interest in the field. Laser cutting machines produce precisely fabricated plates containing small slits at the location of the objects and the plates are placed in the spectrograph's entrance aperture. This allows for up to 100 objects to be imaged and a spectrum of each taken simultaneously.

A similar technique is used by the Two Degree Field (2dF) system at the Anglo-Australian Telescope. Instead of using manufactured masks, hundreds of optical fibres (400 in the case of 2dF) are placed in the focal plane by a computer-controlled robot gantry to simultaneously acquire the individual spectra.

The aim of this project is to investigate the use of an alternative method — a Fabry-Pérot interferometer (FPI). This can be thought of as a tunable narrow-band

filter, allowing a series of images to be taken of the field at specific wavelengths. These wavelengths can be chosen to step through a spectral feature of interest. Since every star is individually resolved, the spectrum of every star in the field can be obtained. Depending on the exposure time and the field, this could result in 1,000 simultaneous spectra.

The particular FPI that we plan to use for observations is the RSS, a prime-focus spectrograph providing long-slit, multi-object and imaging spectroscopic modes, together with polarimetric capability. The RSS was designed, built and commissioned as a collaboration between groups from the University of Wisconsin-Madison[1], Rutgers University and the South African Astronomical Observatory. This instrument is currently undergoing throughput improvements and will not be available for scientific use until the first-half of 2009.

The research which inspired this thesis was by Rangwala et al. (2009), who used Fabry-Pérot absorption line imaging spectroscopy to measure radial velocities using the spectral line of singly-ionized calcium (CaII) at 8542 Å in stars of the Milky Way's bar. This thesis investigates whether this same technique could be applied to the investigation of s-process element abundances in stars in the globular cluster 47 Tuc.

1.1 Why was 47 Tuc chosen as a target?

47 Tuc (NGC 104) is the second-brightest globular cluster in the night sky (after ω Cen) and is one of the most studied globular clusters. It is metal rich, [Fe/H]$= -0.67$ (Carretta et al. 2004), and contains stars of ages 11 to 14 billion years (Gratton et al. 2003). Located at a declination of 72°S, it is ideally placed in the sky for observations with SALT.

As discussed in the previous section, it was previously assumed that the stars in a globular cluster were all formed from the same cloud of gas and dust at about the same time. This meant that these clusters were excellent testing grounds for investigating initial mass functions of clusters because their Hertzsprung-Russell diagrams would show a single isochrone. If it is found that there is a star-to-star inhomogeneity in chemical abundance then there are two options — first the variations are caused by element production in the stars of the cluster; or there was some initial abundance variation in the cloud of gas and dust from which the cluster formed.

The assumption that all the stars in a particular cluster have the same chemical abundances has been known to be untrue for many years. For instance, the first confirmed star-to-star variation in ω Cen was seen by Freeman & Rodgers (1975), who found a spread in [Ca/H] from -1.6 to -0.6 in 25 RR Lyrae stars. Of course RR Lyrae stars represent only a small biased selection of stars in a cluster, as not all stars cross the instability strip.

[1]Their site for the RSS (originally known as Prime Focus Imaging Spectrograph or PFIS) is found at `http://www.sal.wisc.edu/PFIS/`

Later studies by authors such as Suntzeff & Kraft (1996) confirmed there is an intra-cluster abundance variation. They, along with other authors, have shown that there is an absence of stars below [Fe/H] = −1.8, a sharp peak in the distribution at [Fe/H] = −1.7 and then a long tail to higher metallicities.

1.1.1 S-process elements

The name of the s-process was chosen by Burbidge et al. (1957) to describe the nucleosynthesis process where elements were formed by slow-neutron capture. The basic process is as follows. In stellar interiors, a nuclide ${}^{A}_{Z}\mathrm{X}$ can capture a neutron n,

$$ {}^{A}_{Z}\mathrm{X} + \mathrm{n} \rightarrow {}^{A+1}_{Z}\mathrm{X} + \gamma. \tag{1.1} $$

If the new nuclide ${}^{A+1}_{Z}\mathrm{X}$ is unstable, decaying through β-decay, then the subsequent reaction will take place

$$ {}^{A+1}_{Z}\mathrm{X} \rightarrow {}^{A+1}_{Z+1}\mathrm{X} + e^{-} + \overline{\nu}_{e} + \gamma. \tag{1.2} $$

If there is a "slow"neutron flux compared to the half-life of ${}^{A+1}_{Z}\mathrm{X}$, then the reaction is known as the s-process. Although the flux of neutrons in the interior of stars can be as high as 100 billion per cm^2 per second, an individual nucleus will only capture one neutron per 100,000 years. There is a related process called the r-process for reactions were the half-life is long compared to the neutron capture time and occurs mainly in supernovae. The s-process runs up the "valley of β-stability" of the nuclide chart, with those elements to the right being produced by the r-process, while those to the left are created by the p-process, which represents proton capture.

An example of an s-process element is technetium (Tc). There are no stable isotopes of Tc but it has been observed in the spectra of stars, first in S stars by Merrill (1952). The observed isotope, ${}^{99}\mathrm{Tc}$, has a half-life of about 2.6 million years and is formed in the nuclear-burning regions in the interior of stars. In order for it to be visible in the spectra of stars (which only sample the outer layer of a star) it must be mixed to the surface in a short time-scale compared to the age of the star — 10^5 years compared to 10^9 of years. This is conclusive evidence for the s-process occurring in stellar interiors.

One recent study that did concentrate on s-process elements was Wylie et al. (2006). Seven giant stars, including some asymptotic giant branch stars, in 47 Tuc were observed and the abundances determined. They found that there was a mean enhancement of the light s-process elements ([ls/Fe]) of $\sim +0.6$ dex and the heavy-s ([hs/Fe]) of $\sim +0.3$ dex. Results of this and other studies are presented in Table 1.1. But why did Wylie et al. (2006) investigate asymptotic giant branch stars? This needs to be examined as part of different aspects of stellar evolution.

Table 1.1: Element abundances from previous studies of RGB stars in 47 Tuc in dex. One of the key items of interest is the large range of abundance values of the light (Y and Zr) and heavy (Ba and La) s-process elements.

Parameter	BW92[a]	AB05[b]	J04[c]	W06[d]
No. of Stars	4	5	12	7
[Fe/H]	-0.81	-0.67	-0.69	-0.61 ± 0.08
[Na/Fe]	$+0.11$	$+0.03$	—	$+0.65 \pm 0.23$
[Sr/Fe]	—	—	$+0.36$	—
[Y/Fe]	$+0.45$	—	-0.11	$+0.65 \pm 0.19$
[Zr/Fe]	-0.39	-0.17	—	$+0.65 \pm 0.16$
[Ba/Fe]	—	-0.31	$+0.35$	—
[La/Fe]	$+0.18$	$+0.05$	—	$+0.31 \pm 0.19$
[Eu/Fe]	$+0.25$	$+0.33$	$+0.17$	$+0.14 \pm 0.12$
[hs/ls]	$+0.06$	$+0.35$	$+0.23$	-0.28 ± 0.11

[a]Brown & Wallerstein (1992); [b]Alves-Brito et al. (2005); [c]James et al. (2004); [d]Wylie et al. (2006)

1.2 Stellar evolution

The following discussion is based on Iben (1985) and provides a context for the various phases of evolution of 1–9 solar mass ($M_\odot$) stars. The various stages are shown in the context of a colour-magnitude diagram in Figure 1.1.

A 1 $M_\odot$ star spends 80% of its life or 10^{10} years on the main sequence. For a star of 9 $M_\odot$ this time on the main sequence reduces to 2×10^7 years. After exhausting the hydrogen in the core of the star, it will evolve to cooler temperatures and larger size. This is known as the main sequence turn-off (MSTO). With no outward radiation pressure supporting the overlying layers, the core contracts rapidly, while at the same time the envelope of the star expands. This expansion is caused by the nuclear burning of a thin hydrogen shell. A star becomes a red giant (SGB and RGB) because of this process.

It is at this point that a critical mass is encountered. Below a total stellar mass of 2.3 $M_\odot$, the helium core is degenerate, meaning the core has a constant temperature due to efficient electron conductivity. This also keeps the core from rising in temperature as quickly as for stars above this mass threshold. For stars with masses above 2.3 $M_\odot$, the core will rise in temperature enough for helium to begin to fuse. This occurs quickly enough that the hydrogen shell has enough time to increase the mass of the helium core sufficiently for it to overcome degeneracy.

For the lower mass stars, violent helium burning occurs after a longer time. The energy produced by the helium burning cannot be conducted away quickly enough and the core undergoes helium flashes. After these core flashes, the core is no longer degenerate and helium burning occurs as in stars over 2.3 $M_\odot$.

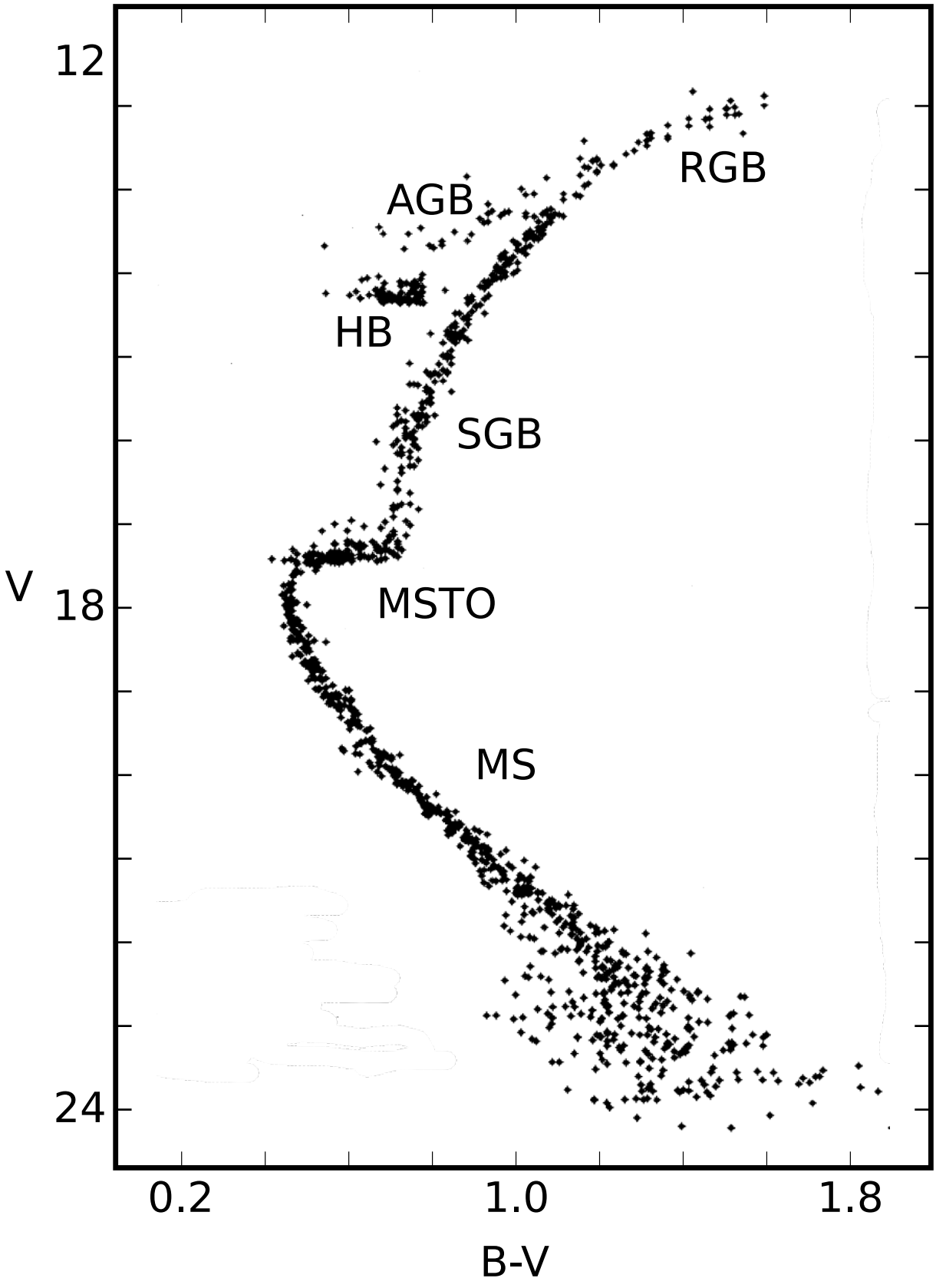

Figure 1.1: Colour-magnitude diagram of 47 Tuc, showing major sequences of stellar evolution. From top: RGB = red giant branch, AGB = asymptotic giant branch, HB = horizontal branch, SGB = sub giant branch, MSTO = main sequence turn-off and MS = main sequence. Figure from Hesser et al. (1987) who note that the diagram is intended to only show the locations of the principal sequences and is not representative of the true luminosity function.

The amount of time a star spends with a helium-burning core is determined by the mass of the core. For the lower mass ($< 2.3\ M_{\odot}$) stars, this is generally a constant time of about 10^8 years. For stars above the critical mass threshold of 2.3 $M_{\odot}$, the core size increases with stellar mass, giving a decreased time.

With the exhaustion of helium at its core, single stars with masses between 1 and 9 $M_{\odot}$ enter into the stage of evolution known as the thermally pulsing (TP) asymptotic giant branch (AGB). Such stars have a highly degenerate core of carbon and oxygen. But the temperature of the core is below that necessary to ignite carbon burning. The 10^8 K temperatures are maintained by the gravitational contraction caused by the increasing mass from the burning hydrogen and helium shells.

The thermal pulsing arises from the alternating burning of the helium and hydrogen shells. For 90% of the time it is the latter that provides the major source of energy that reaches the surface. As the hydrogen shell burns it increases the mass of the helium shell and the temperature at its base. When it reaches a temperature and density sufficient to start the triple-α process of helium burning, the energy released is produced too quickly for radiative transfer to carry it outwards. The shell increases in temperature and expands outwards, pushing material both outwards towards the surface and inwards towards the core. This expansion causes the hydrogen shell to be pushed outwards to a point where it cools enough that the hydrogen burning ceases. The expansion of the helium shell causes its burning rate to decrease, so it shrinks, allowing the hydrogen to return to a region with a temperature where it can resume fusion.

The period of these pulses depends on the mass of the star. At the higher end of the mass scale (5 $M_{\odot}$), they are on the order of thousands of years, while for stars less massive than the Sun, they can be hundreds of thousands of years (Padmanabhan 2001).

During the thermal pulse, the convective envelope that forms the top part of the star moves inwards in mass. Material enters the convective envelope and is mixed to the surface in a process known as third dredge-up. This third dredge-up is the key to why AGB stars are astrophysically interesting. 47 Tuc's AGB stars are believed to be less than 1 $M_{\odot}$ (Gilliland et al. 1998). Stars of this mass should not have undergone the third dredge-up. As such the s-process elements would not be mixed to the surface where they can be observed spectroscopically. Hence the dilemma with the enhanced s-process element abundances of Wylie et al. (2006) and others. This is the reason for extending this analysis to a larger sample of stars.

1.3 Outline

This research is about utilizing the FPI, so it is necessary to first understand the instrument. The mathematics and properties of an ideal FPI are discussed in Chapter 2, along

with those of the FPI of the RSS.

Chapter 3 discusses actual FPI data that taken by Rangwala (2008) and provided by them for this research. The data were for stars in Baade's Window[2] and centred on a CaII line. The original aim of their research was to investigate stellar kinematics, the common reason for FPI observations. In addition they were able to extract abundance information for the stars. The stars and the line itself are not representative of 47 Tuc, but the experience gained from the reduction of these images is invaluable for processing the images and data for 47 Tuc.

Two different datasets were provided. The first was reduced to the point of spectrum segments and was used for understanding how to fit spectra to data points. The second consisted of images of an area of the sky. Using this, it was possible to learn about the photometry of such images and the normalization that is required.

Chapter 4 moves to looking at s-process elements in 47 Tuc through spectrum simulation and the fitting scheme that has been developed during this project for determining the elemental abundance of the star. It discusses how synthetic data were used for testing this scheme. In the final concluding chapter is a description of the set of observations of 47 Tuc (and potentially other globular clusters) that are proposed with the FPI on the RSS on SALT.

[2]Baade's Window is a region of the sky in the general direction of the Milky Way's centre in the constellation of Sagittarius, which is relatively free of obscuring interstellar dust.

Chapter 2

Fabry-Pérot interferometer

The Fabry-Pérot interferometer (FPI) consists of two parallel, flat, semi-transparent mirrors separated by a fixed distance. If monochromatic light enters at an arbitrary angle to the normal, multiple reflections and transmissions take place that result in a circular interference pattern. It was first described by Charles Fabry and Alfred Pérot (Fabry & Pérot 1901), who soon began using the instrument for remeasuring the wavelength of spectral lines in the solar spectrum (e.g. Fabry & Pérot 1902). Two reviews of Fabry-Pérot interferometers in astronomical settings, as well as more generally, can be found in Hernandez (1986) and Vaughan (1989).

This chapter looks at a brief history of the FPI (Section 2.1), the mathematics of an ideal FPI (Section 2.2), the characteristics of the SALT FPI (Section 2.3), and a comparison with other multi-object spectroscopy techniques (Section 2.4).

2.1 Brief history of the Fabry-Pérot interferometer

The first extrasolar astronomical use was by Fabry in 1914 (Buisson et al. 1914), who observed the Orion Nebula. They determined that the mean radial velocity with respect to the Sun of the region surrounding the Trapezium to be $+15.8\ \mathrm{km\,s^{-1}}$. This value agrees well with modern values, which range from 19 to 25 $\mathrm{km\,s^{-1}}$ (O'Dell 2001). They also measured the wavelengths of "nebulium", which is now known to be lines formed by a forbidden transition of oxygen.

Like the first use of the Fabry-Pérot techniques in astronomical research, later research has focused on galactic and extra-galactic radial velocity studies. De Vaucouleurs developed a combination Fabry-Pérot interferometer and a cascaded intensifier image tube for measuring galaxy rotation curves, the "galaxymeter" (de Vaucouleurs 1981).

FPI instruments are used regularly on large telescopes — the Yepun telescope (UT4) of the Very Large Telescope as part of the NAOS-CONICA instrument (Lenzen et al. 2003, Hartung et al. 2004) and the Kyoto tridimensional spectrograph II on Subaru (Sugai et al. 2006).

The instrument with which it is planned to take observations as part of this long-term

project is the Robert Stobie Spectrograph (RSS) of the Southern African Large Telescope (SALT). The RSS is a prime-focus spectrograph which provides long-slit, multi-object and imaging spectroscopic modes. It was designed, built and commissioned as a collaboration between groups at the University of Wisconsin-Madison, the South African Astronomical Observatory and Rutgers University, the latter providing the expertise for the Fabry-Pérot mode.

2.2 Ideal Fabry-Pérot interferometer

This section looks at the properties of an ideal Fabry-Pérot interferometer and is based upon Hernandez (1986). It ignores effects caused by the limited size of the mirrors and diffraction.

An ideal FPI consists of two parallel glass plates, which is known as an étalon (Figure 2.1), with highly reflective coatings applied to the inside surfaces and anti-reflection coatings on the outer surfaces. Light enters at an angle θ. At the first surface there is reflection and transmission of the wave, which is repeated at each subsequent surface interface. This causes a phase lag between two successive transmitted waves of

$$\Phi = 4\pi f c^{-1} n d \cos\theta, \tag{2.1}$$

where f is the frequency of the light in a vacuum, c is the speed of light in a vacuum, n is the refractive index of the material between the plates and d is the separation of the plates.

Each reflective surface can be described by complex reflection and transmission amplitude coefficients of r_i and t_i. Let r_1 and t_1 be the reflection and transmission coefficients for a wave travelling from the surrounding medium towards the glass plates, while r_2 and t_2 are for a wave travelling from the plates towards the surrounding medium. If a wave is incident on the plate with unit amplitude, the amplitude of each successive wave reflected from the plate is

$$r_1, t_1^2 r_2 e^{i\Phi}, t_1^2 r_2^3 e^{2i\Phi}, \ldots, \tag{2.2}$$

while the transmitted amplitudes are

$$t_1 t_2, t_1 t_2 r_2^2 e^{i\Phi}, t_1 t_2 r_2^4 e^{i\Phi}, \ldots. \tag{2.3}$$

The total reflected and transmitted amplitudes (A_r and A_t respectively) are the sum

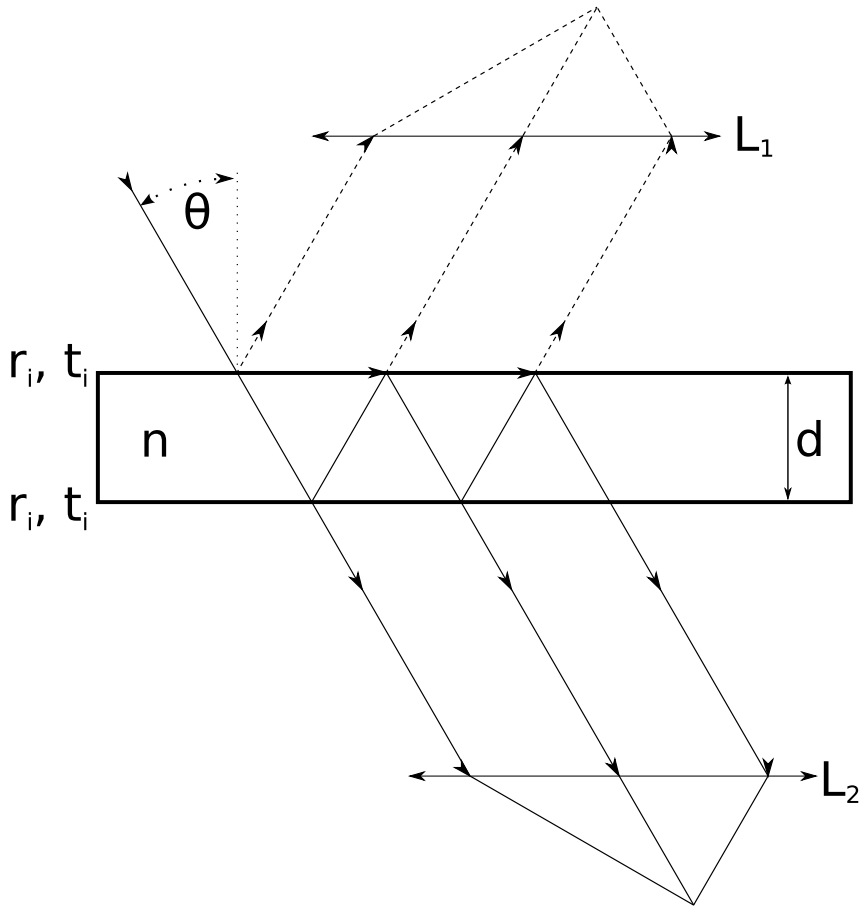

Figure 2.1: A schematic of the design of an ideal Fabry-Pérot interferometer. Light enters at an angle θ through the glass plate into a region of refractive index n. It undergoes multiple reflections and an interference pattern is formed at L_1 and L_2. Image taken from Hernandez (1986).

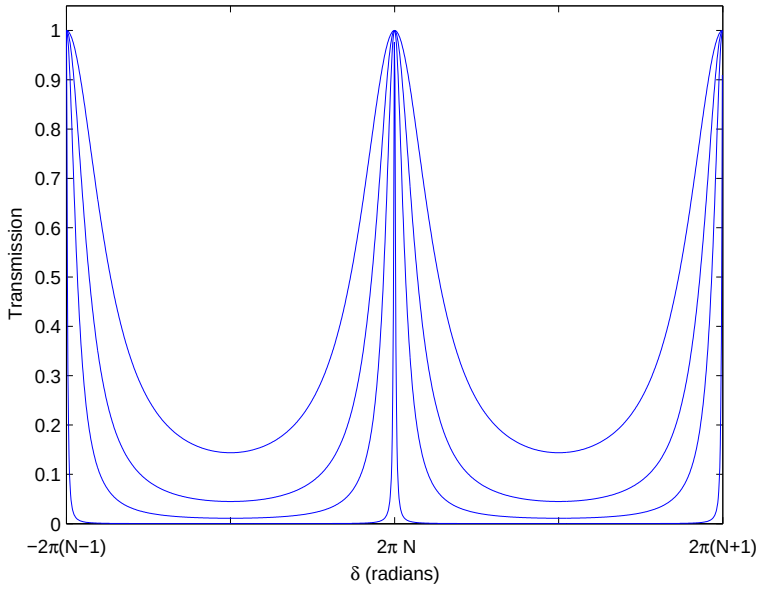

Figure 2.2: The transmitted radiation of the étalon as a function of the phase retardation $\delta = \Phi + 2\chi$ for various values of the reflectivity, R (0.98, 0.81, 0.65, 045 from narrowest to widest). These curves were calculated using the form of Equation 2.9 given in Equation 2.24.

of the amplitudes given in Equations 2.2 and 2.3,

$$\begin{aligned} A_r(\Phi) &= r_1 + t_1^2 r_2 e^{i\Phi} + \cdots \\ &= \left[\left(1 - e^{i\Phi}(R+\tau)\right)\sqrt{R}\right]\left(1 - Re^{i\Phi}\right)^{-1} \qquad (2.4) \\ A_t(\Phi) &= t_1 t_2 + t_1 t_2 r_2^2 e^{i\Phi} + \cdots = \tau\left(1 - Re^{i\Phi}\right)^{-1}. \qquad (2.5) \end{aligned}$$

This uses the relations from Born & Wolf (1964)

$$\begin{aligned} t_1 t_2 &= \tau, \qquad (2.6) \\ r_1^2 = r_2^2 &= R, \qquad (2.7) \\ \delta &= \Phi + 2\chi, \qquad (2.8) \end{aligned}$$

where χ represents the phase changes upon reflection on each of the surfaces.

Using these, it can be shown that the transmitted intensity is given by

$$Y_t(\delta) = \tau^2(1 + R^2 - 2R\cos\delta)^{-1}. \qquad (2.9)$$

This equation is presented graphically in Figure 2.2, showing how the transmitted flux is affected by changing the reflectivity. The maxima of this function are when δ equals

integral values of 2π. In other words

$$N = \frac{\delta}{2\pi} = \frac{2nd\cos\theta}{\lambda}, \tag{2.10}$$

where N is the order of interference. This can be rearranged to give

$$2nd\cos\theta = N\lambda. \tag{2.11}$$

It is common for FPIs to have air in the gap between the plates. As such it can be assumed that the refractive index $n \approx 1$, so the above equation becomes

$$2d\cos\theta = N\lambda. \tag{2.12}$$

The FPI produces a resultant transmitted pattern of a set of bright circular annuli on a dark background. The reflected pattern is the complement — dark fringes on a bright background.

A single wavenumber (λ^{-1}) appears at a multiple number of angles given by Equation 2.12. Rearranging this we find that the angle is a function of the wavenumber and the spacing of the mirrors. If the spacing is held constant, then the necessary change in wavenumber to move from the N to the $N+1$ order is called the free spectral range (FSR) and for the same θ,

$$\text{FSR} = \frac{1}{2nd}. \tag{2.13}$$

Another way to think of the FSR is as follows. Two superimposed, equally intense monochromatic lines are observed with the FPI. The wavelength of one of the lines is changed until they can be seen as two separate maxima. If the wavelength is changed more, they will once again be superimposed. It is now impossible to tell the difference in wavenumber between the lines. The wavenumber separation is unambiguous over the free spectral range.

The width of the transmitted fringes is governed by R (Equation 2.7), with the half-width at half-height (HWHH) being

$$a = 2\sin^{-1}\left(\frac{1-R}{2\sqrt{R}}\right). \tag{2.14}$$

For R close to unity this can be approximated to

$$a \approx \frac{1-R}{\sqrt{R}}. \tag{2.15}$$

Due to the nature of the FPI, these functions have a period of 2π. The normalized HWHH

is defined as the ratio of the width to the period,

$$a^* = \frac{a}{2\pi} = \pi^{-1} \sin^{-1}\left(\frac{1-R}{2\sqrt{R}}\right). \tag{2.16}$$

The inverse of this equation is called the reflective finesse, a measure of the sharpness of the interference fringes of the étalon,

$$\mathcal{F}_R = (2a^*)^{-1} = \pi\left[2\sin^{-1}\left(\frac{1-R}{2\sqrt{R}}\right)\right] \approx \pi\sqrt{R}(1-R)^{-1}. \tag{2.17}$$

If we define an **F** parameter as

$$\mathbf{F} = \frac{4R}{(1-R)^2}, \tag{2.18}$$

and using the approximation part of Equation 2.17

$$\mathbf{F} = (2\mathcal{F}_R\pi^{-1})^2 = 4a^{-2} = (\pi a^*)^{-2}. \tag{2.19}$$

Since the fringes of the FPI have a finite width, then the FPI has a finite resolving power. One criteria of resolving power is the Houston Criterion (Ramsey & Cleveland 1941); two equal-intensity lines are considered resolved when their maxima are separated by their full-width at half-maximum (FWHM). So the resolving power would be

$$\mathbf{R} = (2a\lambda_m)^{-1}, \tag{2.20}$$

where λ_m is the mean wavelength of the two lines.

We have been considering an ideal FPI, but in the real world there are a number of factors that need to be taken into account — absorption of light by the coatings and the plates not being flat and/or parallel. The former means that $T = 1 - R - A$ (instead of $T = 1 - R$), where A is the absorption coefficient. This absorption affects the transmission of the fringes, but does not affect the finesse or spectral resolution. With modern coatings, it is possible to lower A to about 0.005. The non-flatness of the plates leads to a defect finesse, $\mathcal{F}_D$, which changes the effective finesse by

$$\frac{1}{\mathcal{F}^2} = \frac{1}{\mathcal{F}_R^2} + \frac{1}{\mathcal{F}_D^2}. \tag{2.21}$$

The other important difference between the ideal FPI described above and one in an astronomical setting is that sources do not consist of monochromatic light. For a source consisting of bright emission lines, this would not be a problem for a detector able to discriminate colours — e.g. the human eye. But for the standard CCD detectors used in astronomy, filters are commonly used to separate the different colours. This is

obviously essential for absorption line sources which are embedded in a continuous bright background.

There is one more feature of an FPI to discuss. The passband shifts blueward from the centre to the edge of the field. The rays from off-axis points in the telescope focal plane pass through the collimated section at non-zero angles with respect to the optical axis and give rise to the effect. This variation is quadratically varying with radius and for the FPI of SALT is given by

$$\lambda(R) = \frac{\lambda_0}{\sqrt{1 + (R/F)^2}}, \tag{2.22}$$

where R is the radius from the optical axis (centre of image), λ_0 is the central wavelength to which the FPI is tuned and F is the focal length of the camera optics. For RSS, F is about 330 mm (22,000 unbinned detector pixels). Thus at the edge of the field of view (4 arc-min radius, or 1,920 pixels), $\lambda(R_{\max}) = 0.996\lambda_0$ or a 25 Å shift at $\lambda \sim 6500$ Å, the wavelength of the BaII line that is discussed in Chapter 4.

2.3 SALT FPI

The Southern African Large Telescope (SALT) is a 10-metre class telescope located in South Africa. It is operated by a consortium of international partners, which include the University of Canterbury. Its design is based on that of the Hobby-Eberly Telescope, using a fixed elevation to reduce costs to about a fifth of those of similar-sized telescopes, such as Keck. When observing, its azimuth is fixed and the prime-focus tracker, containing the instruments, follows the image.

One of these instruments is the Robert Stobie Spectrograph (RSS). It is a multi-purpose instrument, providing long-slit, multi-object and imaging spectroscopic modes. Of interest to this research is the Fabry-Pérot imaging capabilities. Its design is an evolution and adaption from previous FPI instruments operated by Rutgers — the Rutgers Fabry-Pérot at Cerro Tololo Observatory and the ARIES instrument for the SOAR telescope. For more details about the FPI of RSS and its characteristics see Rangwala et al. (2008).

The FPI of RSS is designed to operate over a wavelength range of 430–860 nm. The imaging capabilities cover the entire 8 arcminute field of view of SALT. With three different étalons it is designed to operate at four different spectral resolutions — at $\lambda = 650$ nm $R \sim 350$, 500, 2,500 or 12,500. It is foreseen that greater wavelength coverage could be achieved in the future with new étalons to cover the ultraviolet.

The size of the collimated beam (150 mm) dictates the size of the mirrors of the étalons. For this size, the surface irregularities cannot be reduced below about $\lambda/100$,

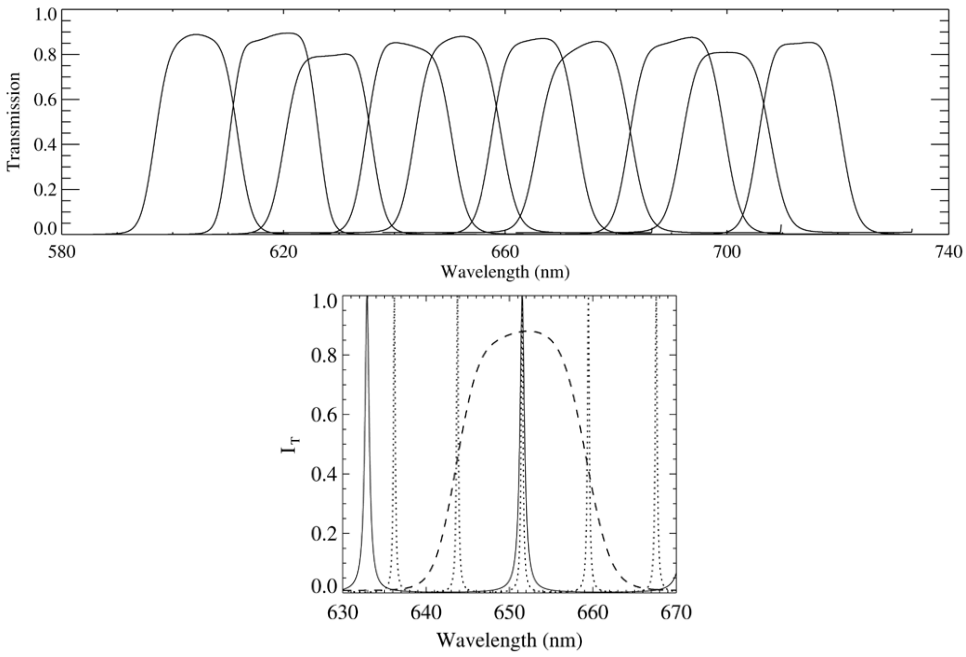

Figure 2.3: (Top) Examples of the transmission curves of the order-selecting interference filter set. (Bottom) Order selection with interference filter and dual étalons. The transmission curve with the solid line is for the low resolution étalon and dotted curve is the transmission curve for the medium resolution étalon. The dashed curve shows the transmission of the filter. Figures from Rangwala et al. (2008).

giving $\mathcal{F}_D \sim 50$. This gives an overall finesse of $\mathcal{F} \sim 25$.

The three étalons are used in a dual-étalon system. For low-resolution work, only the low-resolution étalon is used. For the higher resolutions it is used in combination with either the medium- and high-resolution étalons. This is because in order to isolate the transmission order of interest a blocking filter is required. For the low-resolution mode only 40 such filters are required (top of Figure 2.3). These filters are designed to adequately suppress the transmission of neighbouring orders even in the worst case scenario of the FPI being tuned to the cross-over wavelengths of the filters.

At the higher resolution using blocking filters becomes completely impracticable. One would require a very large number of narrow and expensive blocking filters due to the smaller free spectral range of the higher resolution étalons. For medium- and high-resolution modes, the FPI uses the low-resolution étalon together with a blocking filter and either the medium- or high-resolution étalon in sequence. The low-resolution étalon is tuned to the same wavelength as the other étalon and it suppresses adjacent orders as shown in the bottom panel of Figure 2.3. In this case the total transmission, which would be the product of the three curves, is not shown on the figure. For the highest resolution, 5% of the transmitted signal is parasitic light from adjacent orders. For the medium resolution it is practically zero.

The other reason for using a dual-étalon system is that it increases the resolution by its very nature. Consider an FPI consisting of two identical étalons with a gap between them being large relative to the spacing of the plates of the étalons. Their transmission function can be written in the form

$$Y_{2e}(\delta) = \left(1 - \frac{A}{1-R}\right)^4 \left[1 + \mathbf{F}\sin^2(\delta/2)\right]^{-2}, \tag{2.23}$$

where A is the absorption/scattering coefficient. The equivalent function for a single-étalon system is

$$Y_t(\delta) = \left(1 - \frac{A}{1-R}\right)^2 \left[1 + \mathbf{F}\sin^2(\delta/2)\right]^{-1}. \tag{2.24}$$

When $A = 0$, then the maximum of Equation 2.23 is at $\delta = 0$, while the minimum transmission is at $\delta = \pm\pi$ and the minimum transmission is the square of that obtained for just one étalon.

In the general case of n étalons, the HWHH can be approximated for R values close to unity as

$$a_n^* = a^*\sqrt{2^{1/n} - 1}, \tag{2.25}$$

where a^* is the normalized HWHH for one étalon. Using Equation 2.20, this shows that increasing the number of étalons increases the resolving power of the system. It should be noted that this is for an idealized situation. The étalons of SALT are not identical. But it can be shown that for non-identical étalons, the qualitative result of holds increasing the resolution by adding more étalons.

Although the design specifications called for spectral resolutions ranging from 500 to 12,500, over the wavelength range from 430 to 860 nm, laboratory measurements of the provided FPI components have shown this not to be the case (Rangwala et al. 2008). Due to more apparent plate curvature than expected, the resolution only peaks at around 9,000, as well as there being lower finesse and throughput. This has been attributed to the broadband reflectance coatings of the étalons.

2.4 Comparison of FPI with other MOS techniques

There are many other astronomical multi-object spectroscopy techniques available.

One type uses a graphite mask and small slits are cut with a laser at the location of the stars in the field of view. This is used at SALT on RSS, the FOCAS instrument of Subaru (Kashikawa et al. 2002) and the Gemini Multi-Object Spectrographs (GMOS) (Hook et al. 2004). Of course the slits cannot overlap and it is desirable that the dispersed spectra from one slit do not overlap with those from another slit. As such there is a physical limit on the number of slits that can be cut in the mask. The instrument can

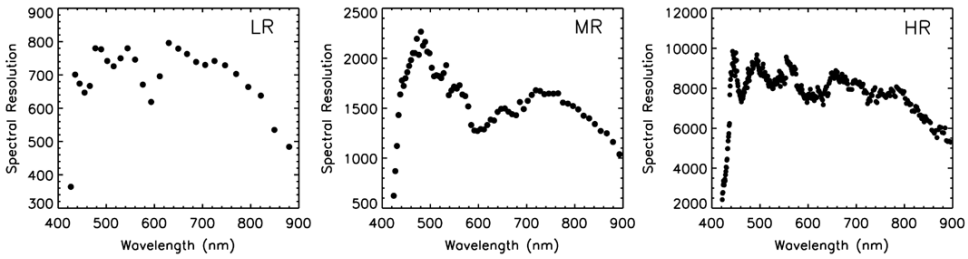

Figure 2.4: Plots of measured spectral resolution for the modes of the FPI of RSS. Although designed to have spectral resolution up to 12,500, in reality the FPI only has a peak of about 10,000. Fortunately for this research, the spectral line of interest (Chapter 4) is at 6900 Å meaning it will still be in a region where the resolution is at least 8,000. Figure from Rangwala et al. (2008).

only hold a certain number of masks at one time, with overhead related to the time it takes to change between masks. The other constraint on the process is that an image of the field is required before the slit mask can be produced. With FOCAS, the images of the field of view have to be made 1–3 months before the MOS observations.

The other commonly used multi-object spectroscopy technique is to use multiple optical fibres. This is the case with the Anglo-Australian Telescope's AAOmega instrument, which in part uses the 2dF robotic fibre positioner. In the case of AAOmega, there are up to 392 fibres with a spectral resolution of 1,300–8,000 (Sharp et al. 2006).

2.5 Conclusion

The Fabry-Pérot interferometer can be thought of as a tunable narrow-band filter. This allows a portion of the sky to be imaged at a series of wavelengths, allowing a spectral line profile to be acquired for all the objects in the field of view. Although limited in spectral resolution, it makes up for this in not having to create masks for specific fields of view, and being able to image all the objects in that field of view simultaneously.

Since the eventual aim of this research is to make observations with the FPI on the RSS, it is important to not only understand the mathematics of the FPI, but to understand how to work with FPI data. This is discussed in the following chapter.

Chapter 3

Data reduction

In order to gain experience at developing the data reduction techniques needed for the SALT data, work was done on observations of Milky Way stars previously acquired by Rangwala (2008).

The original aim of their observations had been related to the stellar kinematics in Baade's Window. They had made observations with the Rutgers Fabry Perot on the CTIO 1.5 m telescope of a strong, infrared, singly-ionized calcium (CaII) spectral line at 8542 Å. They also used the data to find the metallicity of stars using the strength of the CaII line as a proxy. They found the mean metallicity of stars in the Galactic Bulge to be super-solar (Rangwala et al. 2009).

As discussed in the introduction, there were two sets of data provided by the Rutgers' group. The first had already been reduced and consisted of spectrum segments covering 8530 Å to 8555 Å of 300 stars. There was about a six magnitude range in brightness of the stars. An example of one of the spectrum segments is shown in Figure 3.1. Using this set it was possible to learn about the best approach to fitting curves and synthetic spectra to a set of data, without the added complication of performing the photometry on the images.

The second set of data consisted of 16 images covering the same region of the Milky Way and the same spectral line (Figure 3.2 shows an example of one of these images). These images were reduced using the DAOPHOT package and gave first-hand experience of performing photometry on images. It also provided experience in extracting spectral data from a series of photometric images at a range of wavelengths throughout the chosen spectral line (8542 Å of CaII).

Section 3.1 explains the Voigt profile of the CaII line. Section 3.2 covers the MATLAB script that was developed for curve fitting. Section 3.3 compares the results of the thesis script to those found by code provided by Rangwala. Moving from the spectrum segments, Section 3.4 discusses the photometry of the images and Section 3.5 talks about how these data were subsequently normalized. Section 3.6 discusses of the results of this photometry.

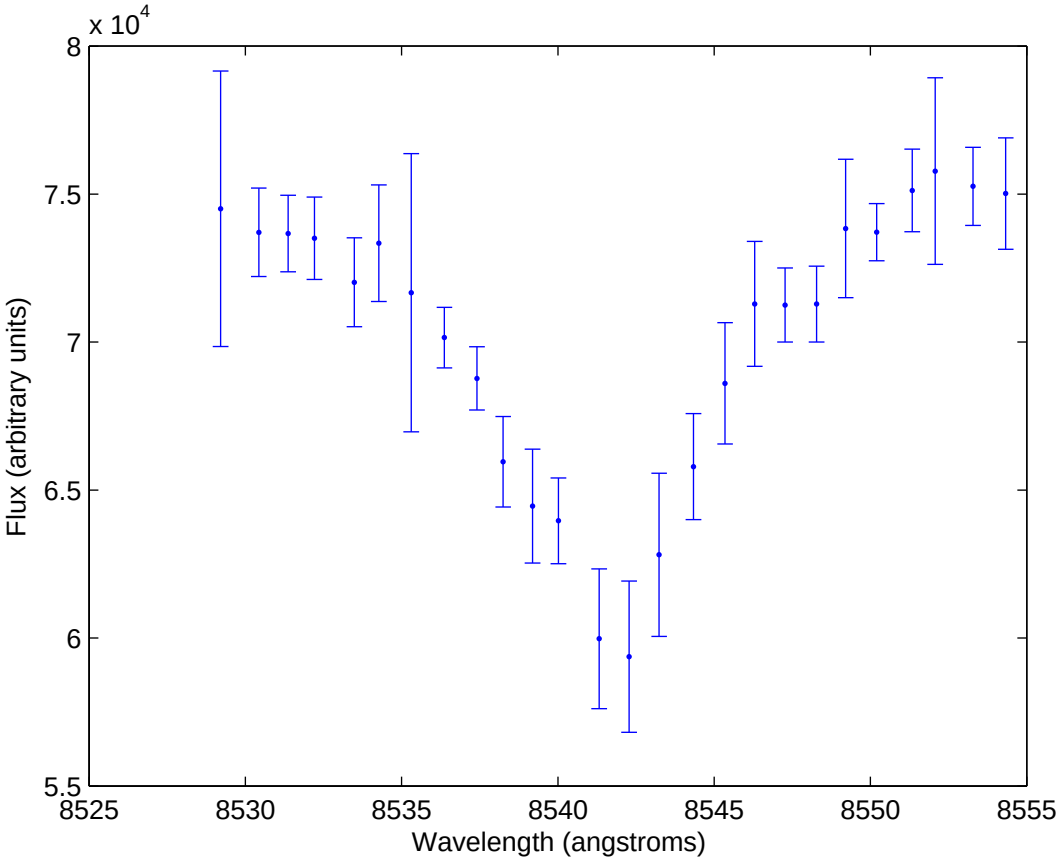

Figure 3.1: An example of one of the lines from the CaII dataset.

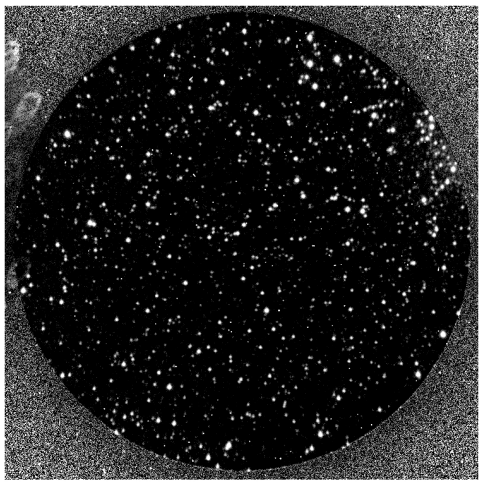

Figure 3.2: Example of an FPI image of the Milky Way. The image is centred at RA 18^{h} and dec $-30°$, with a central wavelength of 8534 Å.

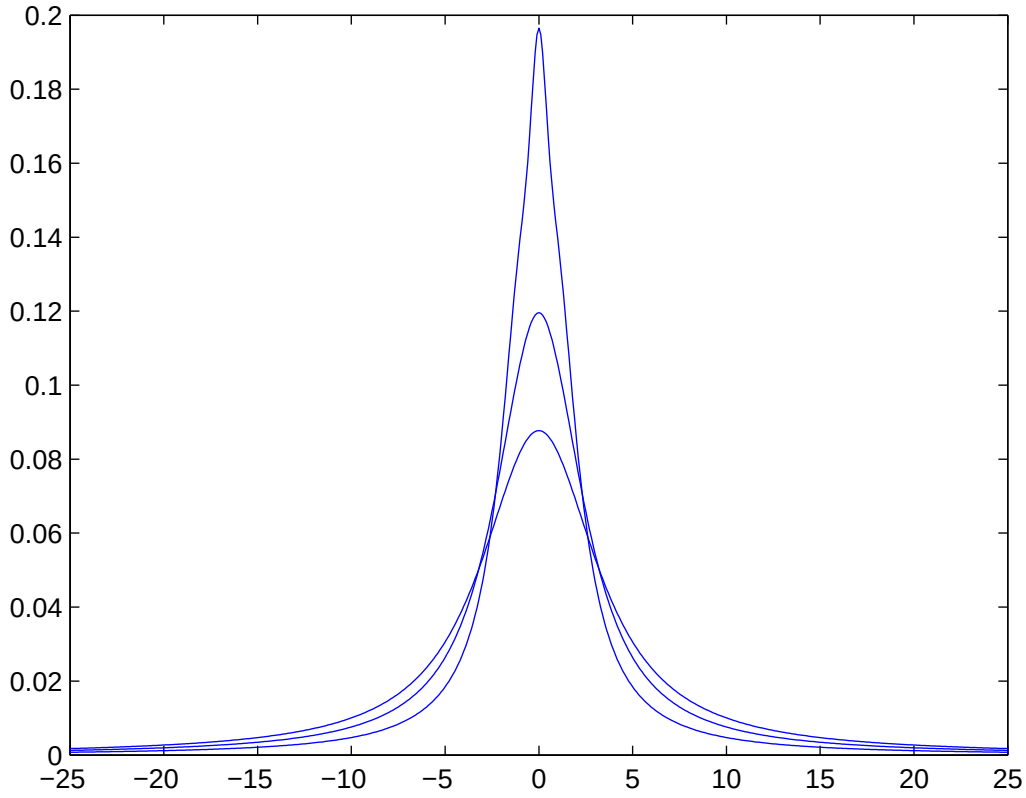

Figure 3.3: Example of three Voigt profiles produced using the code from MOOG based upon Lamla et al. (1965) and given in Appendix A.1. From tallest to shortest, they have $\alpha = 1.5, 2.5, 3.5$.

3.1 The Voigt profile

The CaII line is strong enough to exhibit a Voigt profile, the convolution of a Gaussian and Lorentzian profile. Its basic shape is a Gaussian core with Lorentzian wings. Examples of its shape can be seen in Figure 3.3.

The Voigt function is given by

$$V(\beta_l, \beta_g, \nu) = \int_{-\infty}^{+\infty} \frac{\beta_l/\pi}{\beta_l^2 + (\nu - \nu')^2} \frac{1}{\sqrt{\pi}\beta_g} \exp\left[-\left(\frac{\nu'}{\beta_g}\right)^2\right] d\nu', \tag{3.1}$$

where ν is the independent variable, β_l & β_g are the Lorentzian and Gaussian component widths respectively and the constant factors normalize V to unit area. This function can

only be integrated numerically, with tabulated forms created that utilize an infinite series (e.g. Harris 1948).

In order to numerically calculate the Voigt profile, code from MOOG (Sneden 1973) was used. This code uses the algorithm from Lamla et al. (1965). This code was converted to a MATLAB script and this is reproduced in full in Appendix A.1. They use a function closely allied with the Voigt profile, called the Hjerting function. This has the form

$$H(\alpha,\nu) = \frac{\alpha}{\pi}\int_{-\infty}^{+\infty}\frac{\exp(-y^2)}{\alpha^2+(\nu-y^2)}dy, \tag{3.2}$$

where

$$2\alpha = \frac{\gamma}{\Delta\omega_D}; \nu = \frac{\Delta\omega}{\Delta\omega_D} = \frac{\Delta\lambda}{\Delta\lambda_D}. \tag{3.3}$$

The relationship between the Voigt function V and the Hjerting function H is

$$V(\alpha,\nu) = \frac{H(\alpha,\nu)}{\sqrt{\pi}\Delta\omega_D}. \tag{3.4}$$

In the limits, it gives a Gaussian and Lorentzian profile,

$$\begin{aligned} \alpha = 0: &\quad H(\alpha,\nu) = \exp(-\nu^2) \\ \lim\alpha\to\infty: &\quad H(\alpha,\nu) = \tfrac{1}{\sqrt{\pi}}\tfrac{\alpha}{\alpha^2+\nu^2}. \end{aligned}$$

$H(\alpha,\nu)$ (Equation 3.2) is normalized in the code such that

$$\int_{-\infty}^{+\infty} H(\alpha,\nu)d\nu = 1. \tag{3.5}$$

So in order for it to fit to the data, it needs to be multiplied by a scaling factor to give the strength of the spectral line, the equivalent width.

3.2 Application of line fitting methods

Along with the spectrum segments, FORTRAN code was provided by Rangwala (2008) that could fit Voigt profiles to the data. However it was decided to develop a new scheme[1], since such a function-fitting method would not work for more complicated profiles that it was known would be encountered with the work discussed in Chapter 4.

The spectrum segments came in the form of:

```
   1  26  456.77  373.11   66.86
55.38 11.517 0.008 52.39 11.537 0.008 49.34 11.591 0.009 46.41 11.709 0.008
...
```

[1] based on MATLAB scripts

The top line gives the information on the star — a star number, number of frames, x and y position in the field and the distance from the centre of the field of view (FOV). In the following lines the first column is the wavelength information, the second the brightness in an arbitrary magnitude scale (mag) and the third is the error in the brightness values (σ_{mag}). This is repeated across the columns. The other important file provided contained the normalization factors. Since each image was taken at a different time over the course of a night, the fluxes must be normalized (see Section 3.5 for more discussion of normalization).

The data were processed so as to normalize them and convert to flux units, using the following equations,

$$\log F = 10.0 - 0.40 \times \text{mag}, \tag{3.6}$$

where mag is the magnitude information of the star and F is the flux in arbitrary units. Thus

$$F_n = \text{normalization} \times F. \tag{3.7}$$

The error is calculated by

$$\sigma = 1.0857 F_n \sqrt{F_n^2 + \sigma_{\text{mag}}^2}. \tag{3.8}$$

These equations came from the code provided by Rangwala (2008). The fitting process could then begin.

Since the data were known to be centred on the spectral line it was reasonable to assume that the short wavelength and long wavelength portions of the data would be the continuum. Even if the spectral line was shifted by radial velocity and/or position in the FOV, either the left or right side should have contained the continuum.

From preliminary work, it was found to be important to make sure to compare the left and right side to each other. If the left and right sides were just averaged, then a highly depressed side could drag the continuum level down. So if the continuum levels of the left and right sides differed by more than 1%, then the code selected the highest value.

This next portion of the script determined the minimum of the spectral line in flux and the wavelength of this minimum. There were a number of checks that were made for this.

Firstly the script determined the minimum data point. Casual inspection of the spectrum segments showed that, in general, the minimum data point was at the minimum of any fitted Voigt function. Due to the limitations of the script, if the minimum data point was shifted too far left or right, the star was ignored. This was because it needed to fit a two-degree polynomial to five points — the minimum point and the two points either side.

The data point with the smallest value had to be checked to ensure that it was really near the minimum of the profile. There were instances where there was an anomalous data point which had a flux value well below the rest of the data. The script compared the previously found minimum with the points either side of it. If they differed by 15% then that point was rejected and the next smallest flux value was found.

As stated above, a two-degree polynomial was fitted to five points. The minimum of this polynomial was calculated and used as the central wavelength of the line. The reason for using this procedure was that in some cases, there was a gap in the data at the true central wavelength which resulted in the minimum point not being at the central wavelength. So the fitted Voigt function was therefore shifted erroneously in wavelength and gave an incorrect radial velocity.

Along with the minimum flux, it was necessary to know the HWHH of the data. This placed a constraint on the width of the fitted Voigt function.

The half-depth was simply defined as the distance halfway from the continuum to the minimum value found in the previous part of the script. Using the `findnearest`[2] function, the nearest data point to the half-depth on the left and right side of the central wavelength was found. Both sides were found, since in some cases there could be anomalous data which would result in an erroneous half-width. Instead of naively taking this point nearest to the half-depth as being at the half-width, some refinement was made. This was for two reasons. One was that there could be bad data. The second was that there could be a gap in the data at the half-depth. This, for instance, could result in the nearest point being at only the third-depth.

Using the data-point closest to the half-depth, a straight line was fitted to this point and the points either side. If the slope of this fitted line was of the wrong sign, that side of the line is rejected (e.g. the left-hand side of the line has a positive slope when it should have a negative slope). If both have the wrong sign, then the star is rejected for fitting purposes. Looking at all the stars for which both sides were determined, it was found that there was an average standard deviation of 2 Å between the left- and right-side values. This standard deviation gave the range over which the fitting scheme was allowed to look when fitting the Voigt function.

The reason for determining the depth and width of the data was that it provided constraints on the fitting process. Without them, it could often just diverge to infinity.

It was decided that the easiest method for fitting was a brute-force parameter space search. In this case there were two parameters — the Voigt parameter (α) and the scaling factor.

The determination of how good the fit of the Voigt profile to the data is ascertained

[2]This function is not part of the standard MATLAB package. At the time of this thesis it can be found at `http://www.mathworks.com/matlabcentral/fileexchange/2838`.

using a least-squares method. A straight line was fitted to a plot of the data ($x \pm \sigma$ and $w_i = 1/\sigma_i^2$) against the equivalent point at the same wavelength on the Voigt profile (y). The least-squares fit is given by

$$\begin{aligned} m &= \frac{\sum w \sum wxy - \sum wx \sum wy}{\Delta}, \\ c &= \frac{\sum wx^2 \sum wy - \sum wx \sum wxy}{\Delta}, \\ \Delta &= \sum w \sum wx^2 - \left(\sum wx\right)^2, \end{aligned} \tag{3.9}$$

where m is the slope of a straight line and c is the y-intercept of the line. A perfect fit would result in $m = 1$ and $c = 0$, so the best fit is found by minimizing what is known in this thesis as the "R-statistic"

$$R = |1 - m| + |c|. \tag{3.10}$$

From testing, this was shown to more often produce values closer to the true value than using the correlation coefficient[3] or just the y-intercept or slope alone.

One obvious improvement, which should be made in future work, is some refinement of the continuum and central wavelength values during the parameter space search. Since this would increase the search to over four parameters, it may become necessary to use some sort of "random walk" parameter space search.

Although the Voigt profile fitting was useful it was not the overall aim of this research. This meant that there was no effort to investigate the uncertainties in the fitting scheme.

3.3 Discussion of results

Using the script described above, the Rangwala data was fitted with Voigt profiles. This section presents a comparison of its results to those found with the FORTRAN code provided with the Rangwala data. Table 3.1 gives the complete dataset and the detailed discussion follows.

The first figures to look at are Figures 3.4 and 3.5. These illustrate the best and worst fits of the script as judged by the R-statistic described in Equation 3.10. The good fits show that the script can provide very good fits to the data covering a wide range of brightnesses.

[3]The correlation coefficient is given by

$$r = \frac{\sum (x_i - \overline{x})(y_i - -\overline{y})}{\sqrt{\sum (x_i - \overline{x})^2 \sum (y_i - -\overline{y})^2}}.$$

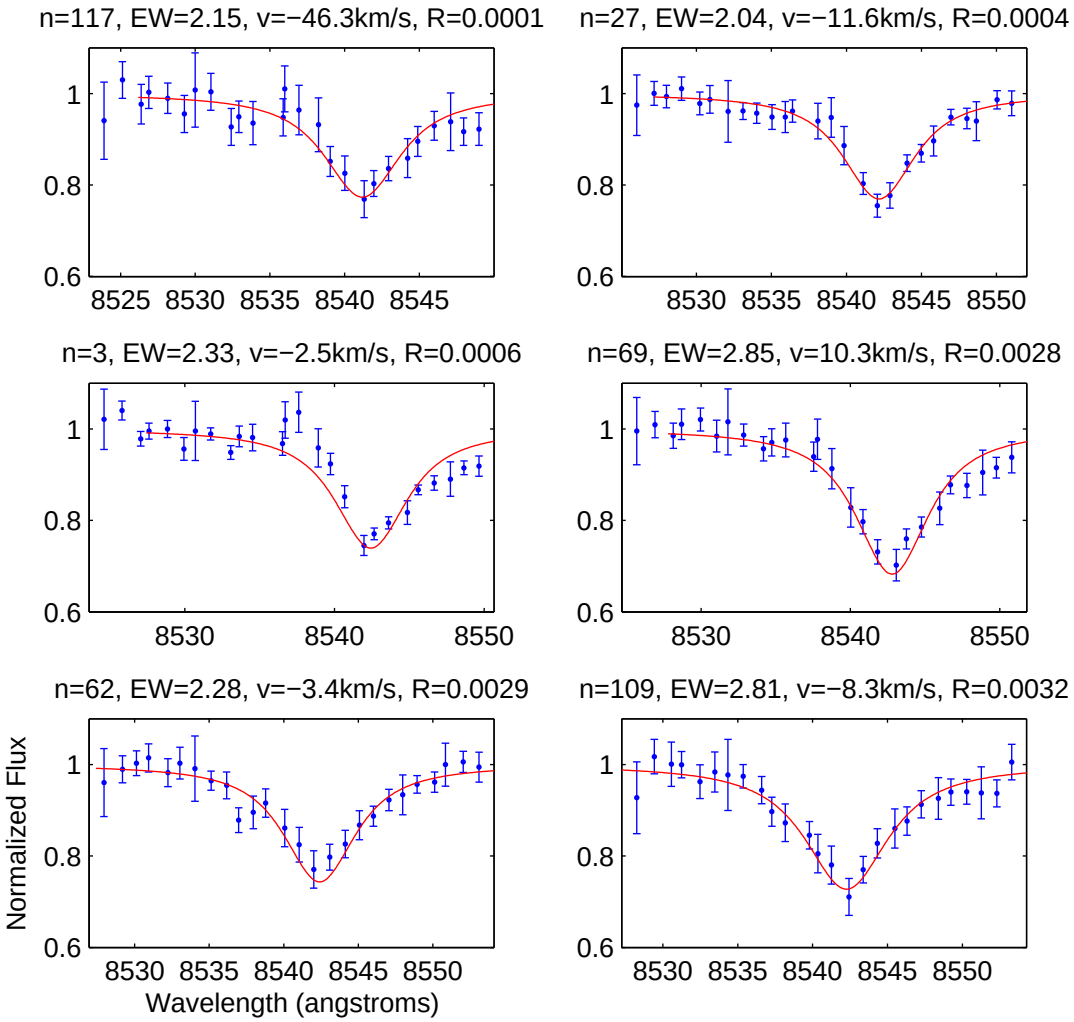

Figure 3.4: Some examples of the good fits produced by the code written. n is the star number, EW is the equivalent width in angstroms, v is the radial velocity in $\mathrm{km\,s^{-1}}$ and R is the value of the fitting statistic given by Equation 3.10. See Section 3.3 for more discussion.

The common element amongst the bad fits is that the stars do not have simple CaII Voigt profiles, but also some emission or extra absorption. This is particularly obvious in the middle-left plot of Figure 3.5. Here the left-hand side of the line is blended with another absorption feature. This causes the script to try and compensate and fit a wider line profile than required.

A no fit occurred when the script failed to make a fit. An example of this would be if points defining the half-width could not be found on both sides of the centre of the line.

Looking at Table 3.1, the radial velocity is discussed in Section 3.3.1, the equivalent width in Section 3.3.2 and the continuum values in Section 3.3.3.

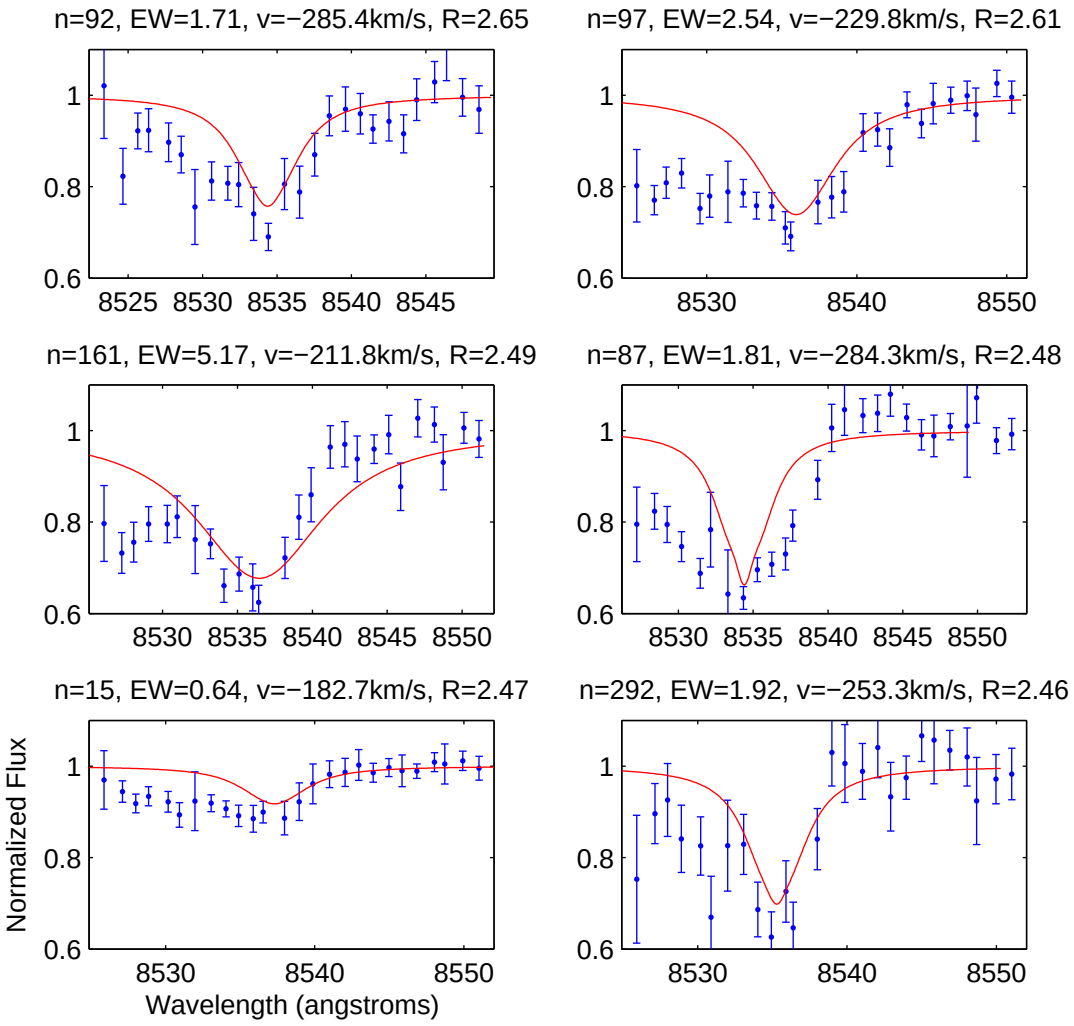

Figure 3.5: As for Figure 3.4 but for the worst fits. See Section 3.3 for more discussion.

Table 3.1: Data for all the stars from the spectrum segments provided by Rangwala. The star numbers are those used by Rangwala. Rows with "—" exist for stars for which no fit was found by the thesis script. The table continues until Page 31.

Star	EW (Å)	v_{rad} ($\mathrm{km\,s^{-1}}$)	Cont	R	HWHH (Å)
1	2.27	3.31	193426	0.02	3.19
2	1.27	−18.84	146153	1.58	3.06
3	2.33	11.93	133291	0.00	3.23
4	2.40	−17.28	123924	0.01	3.06
5	2.92	−5.90	74576	0.03	3.46
6	2.93	−56.36	59530	0.62	3.60
7	0.72	−43.90	56419	0.43	1.94
8	1.87	4.32	44656	0.74	2.55
9	0.94	21.76	37401	0.02	2.13
10	3.46	−183.63	25862	2.29	3.87
11	1.76	−213.33	24769	2.41	2.29
12	3.14	−21.71	22644	0.01	4.30
13	2.75	−72.07	21768	0.72	3.71
14	1.38	64.91	17830	0.85	1.82
15	0.64	−168.26	16808	2.47	6.29
16	0.92	−227.24	16457	2.43	4.03
17	—	—	—	—	—
18	3.64	−119.49	14467	1.53	3.12
19	1.98	18.06	13278	0.01	2.79
20	1.42	−145.54	12954	2.15	2.86
21	5.03	153.01	13459	1.21	2.42
22	—	—	—	—	—
23	—	—	—	—	—
24	1.53	−20.18	11496	0.89	4.35
25	2.42	−7.81	11194	0.60	5.56
26	—	—	—	—	—
27	2.04	2.78	11317	0.00	2.71
28	2.07	13.83	10634	0.14	2.88
29	3.36	42.32	9711	0.16	2.77
30	3.02	−42.91	9686	0.12	3.85
31	3.99	25.18	9682	0.27	4.29
32	5.27	−273.93	9447	2.15	3.89
33	6.03	−162.85	9725	1.71	3.74
34	1.33	−12.13	8893	0.26	2.15
35	3.81	−155.39	9198	1.63	4.15
36	4.48	−127.52	9006	1.62	3.26
37	—	—	—	—	—
38	3.86	19.54	8948	0.14	3.29
39	4.19	88.17	8708	0.65	2.96
40	2.18	−72.24	8054	0.04	2.85
41	4.54	−71.00	8249	0.95	3.17
42	3.31	77.34	7845	0.68	2.58
43	2.18	−85.23	7859	1.26	2.68
44	3.62	−85.98	7588	1.17	3.25
45	3.91	−132.79	7383	1.81	3.30
46	2.56	50.66	7210	0.38	4.66
47	3.09	−55.89	7293	0.09	3.15
48	3.87	−73.37	7232	0.72	4.11
49	1.86	−41.94	7117	0.01	2.71
50	3.60	−45.89	6940	2.00	7.20
51	4.00	75.73	6754	0.60	2.95
52	—	—	—	—	—
53	1.35	8.61	6341	0.10	2.45
54	1.04	−77.54	6032	1.18	6.16
55	—	—	—	—	—
56	2.97	−90.96	6291	0.66	2.10
57	2.46	−120.13	6147	0.78	4.27
58	—	—	—	—	—
59	—	—	—	—	—
60	3.55	−170.72	5494	2.18	3.07
61	3.16	97.50	5047	0.56	2.62
62	2.28	11.03	5134	0.00	4.01
63	4.69	−63.41	5173	0.80	4.05
64	0.00	−175.34	4658	2.00	0.68
65	3.86	69.34	5190	0.25	4.32
66	1.83	−55.12	4780	0.01	3.74
67	4.00	−70.68	4739	0.98	3.08
68	2.31	−26.67	4753	0.01	2.65
69	2.85	24.73	4710	0.00	3.09
70	3.41	−40.81	4449	0.37	3.94
71	1.32	−19.95	4214	0.65	4.28
72	0.43	−196.31	4001	2.36	1.76
73	2.99	−106.17	4139	1.79	2.59
74	3.59	129.22	4268	1.05	2.88
75	4.55	−162.06	3995	1.94	2.95
76	1.51	6.27	3868	0.00	3.03
77	1.86	20.51	3700	0.11	2.58

Star	EW (Å)	$v_{\rm rad}$ (km s^{-1})	Cont	R	HWHH (Å)
78	3.69	−0.17	3886	0.05	3.62
79	3.55	−95.54	3855	0.95	1.69
80	4.08	43.59	3853	0.13	0.50
81	6.27	−171.14	3831	1.90	3.74
82	3.20	−77.70	3673	1.06	3.00
83	4.10	90.67	3752	0.76	3.02
84	3.27	−38.62	3647	0.51	2.59
85	4.84	−203.38	3670	2.02	3.81
86	5.77	−150.68	3531	1.43	3.85
87	1.81	−269.86	3599	2.48	3.90
88	2.64	−23.35	3534	0.10	3.09
89	5.22	113.33	3537	0.85	3.54
90	—	—	—	—	—
91	3.97	−80.43	3457	0.26	6.51
92	1.71	−270.99	3521	2.65	4.59
93	4.17	−105.91	3342	1.30	2.11
94	2.65	−13.06	3198	0.27	2.43
95	—	—	—	—	—
96	3.76	−213.48	3286	2.32	3.21
97	2.54	−215.36	3410	2.61	6.83
98	—	—	—	—	—
99	4.09	−96.76	3304	0.80	6.06
100	2.55	−48.78	3122	0.34	2.99
101	3.76	−42.09	3104	0.70	3.03
102	—	—	—	—	—
103	4.39	−148.03	3118	0.83	4.85
104	3.00	110.61	3044	1.29	1.96
105	2.09	−47.88	2934	0.30	3.76
106	—	—	—	—	—
107	3.19	−45.46	3027	0.03	3.76
108	4.35	−121.95	2982	1.33	2.37
109	2.81	6.08	3060	0.00	3.60
110	3.86	−60.79	2957	0.55	4.55
111	3.51	−109.96	2917	1.14	2.96
112	0.46	183.96	2721	2.14	1.66
113	5.41	−116.79	2942	1.30	2.45
114	3.12	3.19	2809	0.22	3.43
115	4.50	−55.60	2917	0.61	2.23
116	2.64	91.57	2661	0.80	2.64
117	2.15	−31.83	2764	0.00	5.54
118	2.91	−100.00	2672	0.82	3.24
119	2.04	74.83	2653	0.68	3.30
120	3.70	−119.94	2617	1.62	1.91

Star	EW (Å)	$v_{\rm rad}$ (km s^{-1})	Cont	R	HWHH (Å)
121	3.83	−129.33	2643	1.61	3.08
122	3.07	−106.37	2547	1.58	1.57
123	0.69	−129.33	2602	2.18	-0.55
124	4.24	40.03	2631	0.26	3.04
125	4.49	−169.39	2682	2.33	4.41
126	4.18	−128.25	2496	1.77	3.68
127	3.36	−74.18	2454	1.22	2.62
128	3.01	77.42	2469	0.90	2.12
129	3.54	42.14	2541	0.06	4.06
130	3.88	−148.90	2514	1.78	6.41
131	—	—	—	—	—
132	—	—	—	—	—
133	3.44	120.31	2523	0.90	3.75
134	3.63	−186.74	2556	2.06	2.65
135	3.58	−34.17	2507	0.42	3.08
136	4.15	−229.02	2413	2.37	3.77
137	1.88	−30.77	2367	0.96	4.37
138	1.89	122.23	2450	1.19	0.24
139	3.63	−72.12	2396	1.19	2.15
140	5.53	84.19	2406	0.74	4.02
141	2.96	−57.10	2307	0.80	2.46
142	5.57	−97.75	2419	1.12	2.90
143	3.83	−8.16	2373	0.09	4.56
144	4.49	−123.19	2458	0.56	3.64
145	4.30	−42.70	2325	0.27	3.30
146	2.93	79.34	2242	0.40	4.71
147	—	—	—	—	—
148	5.41	−64.10	2301	0.89	3.20
149	5.04	102.23	2348	0.77	3.34
150	4.42	−87.58	2305	0.65	5.42
151	5.12	−103.70	2254	1.17	3.52
152	4.16	−50.91	2294	0.80	4.25
153	—	—	—	—	—
154	2.20	25.53	2209	1.01	2.27
155	2.34	71.99	2268	0.83	1.17
156	3.63	92.67	2148	1.04	6.81
157	2.43	−112.70	2148	1.22	3.66
158	2.67	23.25	2099	0.25	6.95
159	2.53	−121.84	2081	1.73	2.91
160	1.05	−327.83	2117	2.43	6.08
161	5.17	−197.40	2192	2.49	4.77
162	—	—	—	—	—
163	4.64	82.82	2067	0.60	2.49

Star	EW (Å)	$v_{\rm rad}$ (km s^{-1})	Cont	R	HWHH (Å)
164	3.38	89.16	2059	0.52	2.70
165	3.04	−188.40	2041	2.26	1.38
166	—	—	—	—	—
167	3.14	−189.60	1982	2.24	3.29
168	2.91	85.17	1915	0.93	2.50
169	—	—	—	—	—
170	6.08	−158.79	1681	1.76	3.81
171	2.84	−116.33	1858	1.67	2.47
172	—	—	—	—	—
173	2.69	−166.67	1918	1.24	3.87
174	4.33	−112.02	1949	1.48	2.08
175	4.40	35.18	1992	0.23	3.32
176	1.28	−244.25	1949	2.36	3.99
177	3.40	−102.39	1897	1.41	2.19
178	4.36	−199.43	1899	2.17	3.64
179	1.84	−65.24	1787	2.01	6.72
180	—	—	—	—	—
181	3.07	−256.35	1727	2.37	3.31
182	—	—	—	—	—
183	—	—	—	—	—
184	—	—	—	—	—
185	2.68	11.86	1738	0.23	3.03
186	3.11	−48.59	1787	0.53	2.67
187	2.99	−167.08	1773	2.19	2.74
188	3.53	203.36	1748	2.22	4.82
189	—	—	—	—	—
190	2.60	−35.56	1773	0.01	4.55
191	—	—	—	—	—
192	4.57	−94.43	1758	1.18	3.40
193	3.67	−104.46	1674	1.31	3.47
194	—	—	—	—	—
195	2.18	205.04	1418	1.45	5.40
196	1.41	−180.36	1792	2.41	5.51
197	3.61	−47.91	1662	0.57	3.36
198	5.08	−93.57	1666	1.13	4.30
199	3.56	−166.14	1645	1.82	4.15
200	4.23	−76.91	1631	0.92	3.63
201	1.98	−454.62	1624	2.26	4.71
202	4.76	74.68	1663	0.43	3.19
203	1.90	44.51	1495	0.78	3.75
204	3.75	−197.95	1643	2.17	4.51
205	4.50	−158.73	1610	0.99	3.32
206	3.25	31.83	1520	0.36	1.13

Star	EW (Å)	$v_{\rm rad}$ (km s^{-1})	Cont	R	HWHH (Å)
207	3.85	−122.69	1576	1.55	3.22
208	—	—	—	—	—
209	4.26	−226.73	1587	2.09	5.26
210	2.77	−55.37	1587	0.01	3.34
211	2.48	−48.17	1379	0.89	4.98
212	—	—	—	—	—
213	2.45	35.44	1491	0.68	5.30
214	5.88	106.45	1553	0.92	3.42
215	2.43	−4.10	1526	0.23	1.47
216	4.21	125.18	1479	1.41	2.74
217	4.01	−79.37	1527	0.92	2.84
218	4.53	−39.15	1528	0.04	2.65
219	2.98	−178.29	1493	2.16	3.58
220	3.44	−4.31	1526	0.18	5.32
221	3.50	116.22	1412	1.44	6.06
222	5.24	−128.77	1487	1.53	3.05
223	3.81	−132.35	1474	1.77	3.41
224	2.36	17.97	1458	0.36	5.05
225	3.57	−83.35	1475	0.98	3.13
226	4.19	−67.05	1432	1.10	6.36
227	5.33	−121.94	1482	1.68	2.91
228	4.14	74.61	1517	0.65	4.34
229	—	—	—	—	—
230	0.98	−356.35	1431	2.08	5.61
231	0.93	−325.52	1390	2.45	2.81
232	1.17	−217.95	1458	2.35	2.01
233	1.03	−83.97	1530	2.06	4.49
234	—	—	—	—	—
235	—	—	—	—	—
236	2.42	−36.49	1421	0.02	3.80
237	2.71	−43.81	1426	0.59	3.53
238	—	—	—	—	—
239	4.53	−75.53	1419	1.01	2.92
240	4.20	−145.75	1397	1.49	2.94
241	4.32	−159.50	1434	1.86	2.97
242	4.65	−61.17	1395	0.56	2.45
243	3.25	63.34	1373	0.95	2.61
244	—	—	—	—	—
245	—	—	—	—	—
246	—	—	—	—	—
247	3.46	−103.29	1348	1.50	3.45
248	—	—	—	—	—
249	3.42	−171.74	1376	2.17	2.31

Star	EW (Å)	$v_{\rm rad}$ (km s^{-1})	Cont	R	HWHH (Å)
250	3.90	−200.78	1403	1.92	-1.32
251	5.85	100.89	1309	1.03	3.46
252	—	—	—	—	—
253	3.33	−54.88	1287	1.01	3.92
254	4.82	−166.70	1304	2.04	3.45
255	2.34	−420.52	1267	2.06	5.75
256	—	—	—	—	—
257	—	—	—	—	—
258	1.89	−36.22	1265	0.03	2.12
259	5.05	−209.79	1341	1.60	3.90
260	2.93	−187.44	1301	2.23	2.90
261	0.44	261.57	1093	2.19	1.52
262	3.00	60.80	1250	0.60	3.25
263	1.35	45.73	1251	0.87	0.65
264	3.67	92.65	1296	0.77	4.21
265	3.04	−197.26	1302	2.14	3.80
266	—	—	—	—	—
267	3.00	−197.91	1275	2.40	2.51
268	—	—	—	—	—
269	—	—	—	—	—
270	4.17	60.26	1274	0.36	3.99
271	—	—	—	—	—
272	—	—	—	—	—
273	4.86	−150.50	1253	1.54	4.42
274	7.20	112.64	1957	1.12	4.62
275	—	—	—	—	—
276	5.42	−65.92	1236	0.78	3.23
277	1.79	−33.14	1130	1.16	1.30
278	4.38	−161.01	1252	1.26	4.07
279	5.13	−248.92	1233	1.78	4.17
280	4.19	83.99	1188	0.60	3.59
281	4.05	−163.35	1211	1.68	4.18
282	3.18	−18.65	1228	0.26	3.50
283	5.52	−97.54	1253	1.25	4.77
284	2.43	41.37	1197	0.40	2.40
285	—	—	—	—	—
286	2.31	−198.96	1179	2.27	3.44
287	3.16	124.65	1167	1.61	2.04
288	1.14	−259.49	1134	2.44	3.03
289	3.32	−10.21	1235	0.67	2.47
290	2.75	−166.21	1183	1.42	-4.40
291	1.86	−204.94	1167	2.46	2.54
292	1.92	−238.86	1199	2.46	4.15

Table 3.1 — concluded from previous page

Star	EW	$v_{\rm rad}$	Cont	R	HWHH
293	2.45	−36.07	1142	1.13	1.08
294	4.05	−248.40	1133	2.31	3.66
295	3.55	−32.81	1232	0.04	2.32
296	—	—	—	—	—
297	—	—	—	—	—
298	—	—	—	—	—
299	1.16	−58.52	1108	2.03	0.97
300	—	—	—	—	—

3.3.1 Radial velocity

The bad fits also have much larger absolute radial velocities compared to the good fits. This can be clearly seen in comparing Figures 3.6 and 3.7. By removing the stars which had $|R| > 1.5$, it removes all the stars for which the fitted radial velocity was greater than $\pm \sim 200$ km s^{-1}. This is because the script is using the left and right sides of the line. If the star has a large radial velocity, then it will be shifted sufficiently that one side of the line will not be imaged. This will cause a less than precise continuum value, which is critical to determining the abundance.

Along with Figures 3.6 and 3.7, it is useful to visualize the two data sets, the thesis script and Rangwala's fits separately in velocity space (Figures 3.8 and 3.9). These are histograms of the radial velocities from the two datasets. Both have been fitted with Gaussian distributions using `fminsearch`, an unconstrained nonlinear optimization function in MATLAB with the equation

$$f(x) = Ae^{-(x-\mu)^2/(2\sigma^2)}, \tag{3.11}$$

where A gives the peak of the distribution, μ the mean and σ the standard deviation.

Both datasets have resulted in similar peaks ($A = 12.9$ and 12.4 for the thesis and Rangwala scripts respectively), but the μ and σ values are somewhat different ($\mu = -63.0$ & -78.4 km s^{-1} and $\sigma = 115.7$ & 141.0 km s^{-1} respectively). The thesis script histogram was fitted with a narrower Gaussian and with a μ value closer to zero. The magnitude of the difference in μ is only 10 km s^{-1}, which is small compared to the σ values of over 100 km s^{-1}. This suggests that any overall differences in the radial velocity values between the thesis and Rangwala are minor deviations in the way the two methods calculate the central wavelength of the line.

The figures can be compared to those from other surveys of Milky Way bulge stars to see if the shape distributions shown in Figures 3.8 and 3.9 are reasonable and similar. Rich et al. (2007) undertook a "large-scale radial velocity survey of the Galactic bulge". For their sample they found a best-fit Gaussian of $\sigma = 119 \pm 5$ km s^{-1} with $\mu = -11 \pm 30$ km s^{-1}. This σ value is closer to the thesis value than the value found by Rangwala. On the other hand, the μ values are not within the uncertainty of the Rich et al. (2007) value. The reason for this is unknown, but could relate to heliocentric corrections that have not been applied to the data provided by Rangwala.

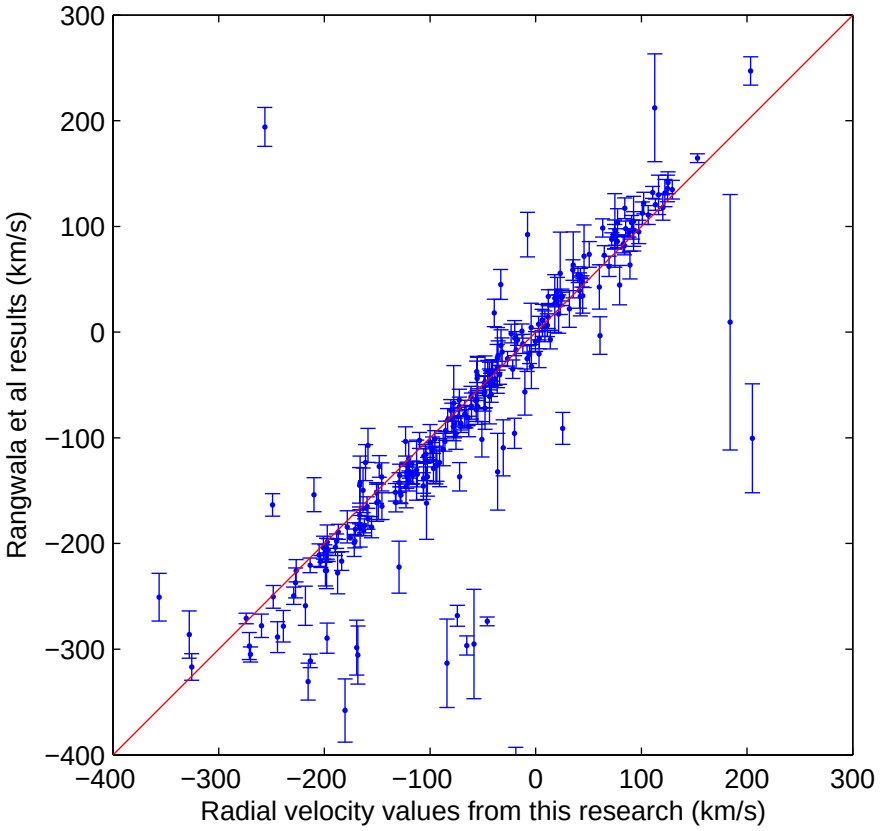

Figure 3.6: Comparison of the radial velocities found using the algorithm described in this thesis and those from the FORTRAN code of Rangwala. Overall there is a good correlation between the two, though it does appear that the slope between the two is greater than unity. There are also several outliers at highly negative velocities. One aspect common between the two data sets is that the peak of velocity is around -50 km s^{-1}, since the overall motion of the stars in that region is away from the Sun. See Section 3.3.1 for more discussion.

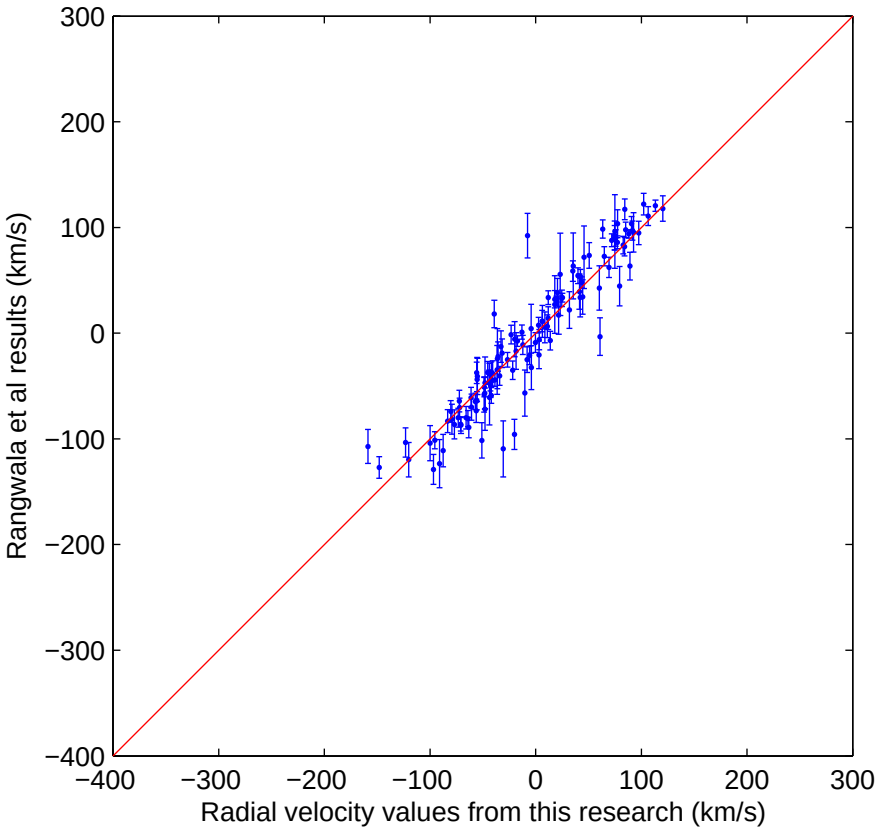

Figure 3.7: Comparison of the radial velocities found using the algorithm described in this thesis and those from the FORTRAN code of Rangwala. This plot shows stars where the $|R| < 1.5$. See Section 3.3.1 for more discussion.

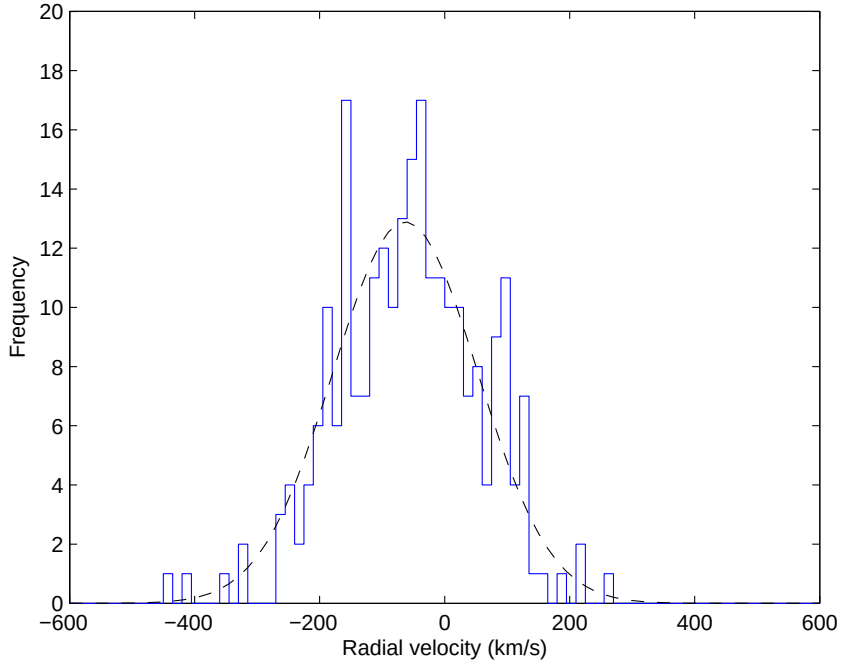

Figure 3.8: Distribution of velocities found by the thesis fitting scheme for the spectrum segments. This Gaussian has the parmeters $A = 12.9$, $\mu = -63.0$ km s^{-1} and $\sigma = 115.7$ km s^{-1}. See Section 3.3.1 for more discussion.

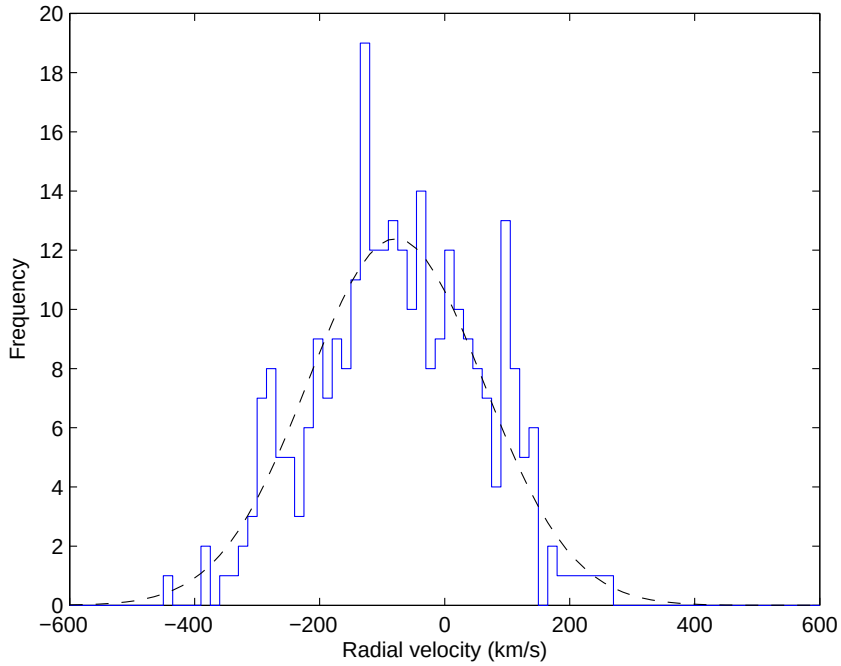

Figure 3.9: As for Figure 3.8 but with the Rangwala values. This Gaussian has the parmaters $A = 12.4$, $\mu = -78.4$ km s^{-1} and $\sigma = 141.0$ km s^{-1}. See Section 3.3.1 for more discussion.

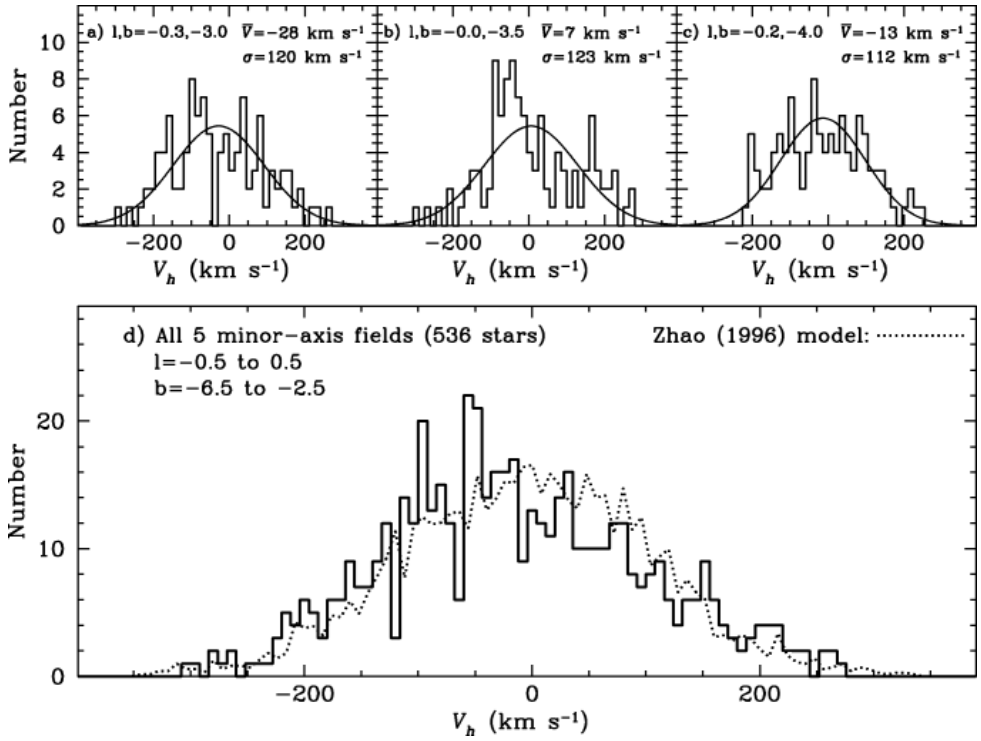

Figure 3.10: Figure from Rich et al. (2007). Velocity dispersion profile of three minor-axis fields ranging from $-4^\circ < b < -3^\circ$. The sum of the top three panels is shown in panel (d). See Section 3.3.1 for more discussion.

3.3.2 Equivalent width

The main aim of this thesis research was abundance determination. As with the radial velocity, the first thing to investigate is the comparison of the thesis values to those found by Rangwala. This is shown in Figure 3.11.

The most obvious feature is that the correlation is nowhere near as strong as that found for the radial velocity. Since the error bars crowd the figure, the bottom plot of Figure 3.11 shows the same data, without the error bars. This shows that there is a grouping of points below the one-to-one correlation line.

Since this shows all the stars, it is useful to see what the correlation is like for only those stars with reasonable fits, but still leaving a large enough sample size to make useful conclusions — this is shown in Figure 3.12. This removes the worst outliers but does show that in general the thesis values were larger than those found by Rangwala. A possible explanation comes from the placement of the continuum which is shown in this and the next section (3.3.3) to be of critical importance in the fitting process.

Not shown on these figures are the twelve points which fell well outside the range. The six worst absolute differences in equivalent width are shown in Figures 3.13 and 3.14.

For example, Star 2 (top-left plot of both figures) is an example of when the Rangwala scheme seems to not provide a good fit to the data. It fitted a Voigt profile with an

equivalent width of 47 ± 99 Å and a radial velocity of -451 ± 58 km s^{-1}. From Figure 3.6, when fits with bad R values are removed, then such high radial velocities also disappear. Compare to the fit from the thesis scheme, 1.27 Å and -33.3 km s^{-1}, which seems like these are much more realistic values.

The other big differences come not from bad curve fitting, but from bad continuum fitting. In the case of Star 97, the Rangwala code fitted a continuum of 4,000 (in unnormalized arbitrary flux units), while the thesis scheme gave a value of 3,400. This means that there was an equivalent width difference of ~ 11 Å. A similar result is seen with star 125, with the continuum fitted by Rangwala much higher than that fitted by the thesis scheme.

3.3.3 Continuum

From looking at the worst correlations, it became obvious that the continuum fitting is extremely important in correctly determining the equivalent width and therefore the abundance. As such, it is interesting to see what sort of correlation there was between the Rangwala code and the thesis script in the continuum values. Figure 3.15 compares the values for each star. It is plotted twice since a simple linear scale fails to properly show outliers and the data is highly bunched at the smaller values. Overall this shows that it is an excellent correlation with few outliers.

But even the log-log plot could be hiding some points that are true outliers. Another way of viewing this data is to create a histogram of the relative difference between the two continuum values, as is shown in Figure 3.16. In this case the values are given by

$$\frac{\text{Thesis} - \text{Rangwala}}{\text{Rangwala}}. \tag{3.12}$$

In other words, positive values mean that the thesis found a larger value than Rangwala and vice versa. The histogram shows that the difference distribution is offset from zero, with $\mu = -0.019$. The Rangwala values were generally larger than the thesis values.

Along with this offset, there is also the width of the distribution. With $\sigma = 0.019$, even those stars within one-sigma of the mean will differ by 2%. The width of the CaII line at the level of the continuum is about 15 Å. This would equate to a difference in

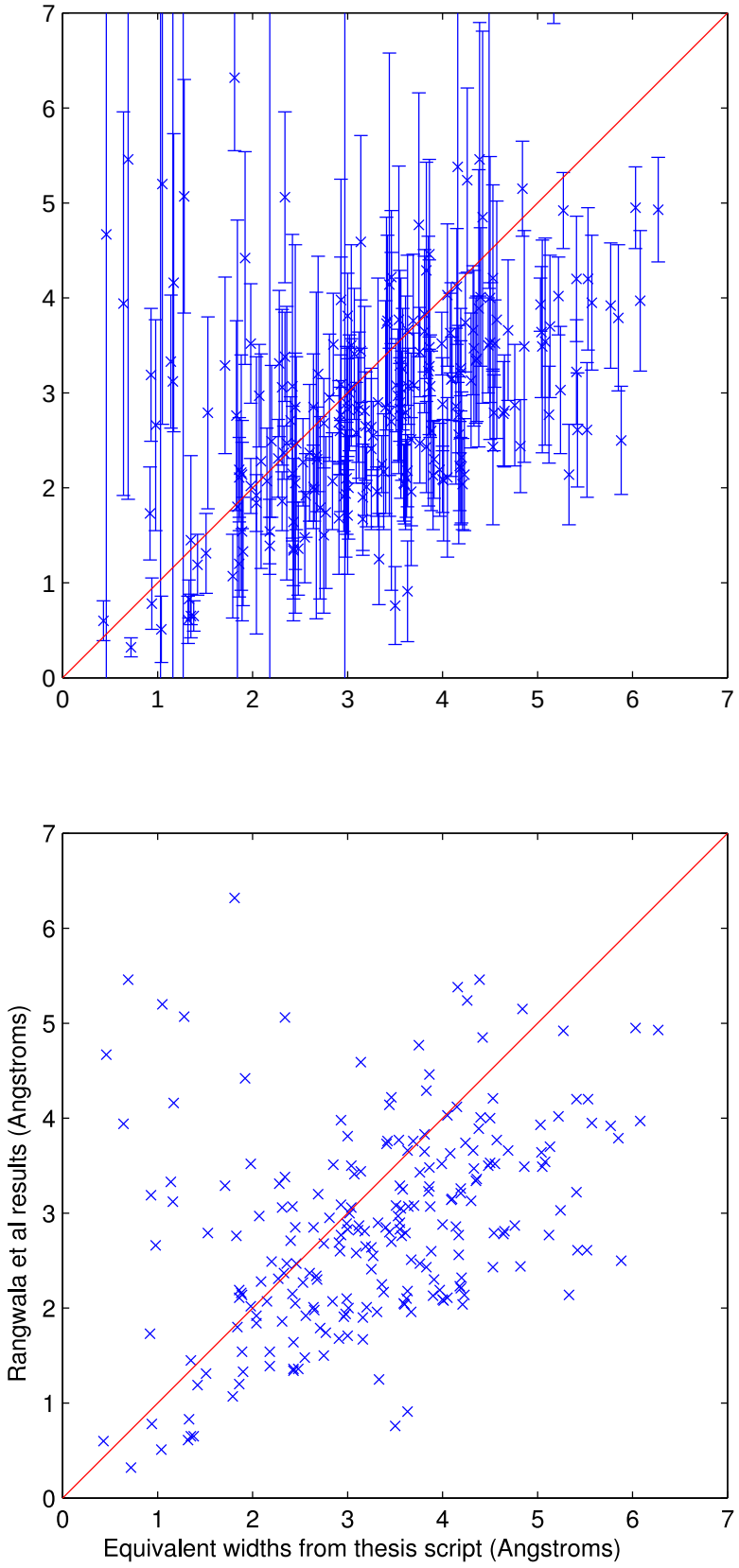

Figure 3.11: Comparison of the equivalent widths found using the algorithm described in this thesis and those from the FORTRAN code of Rangwala. This plot shows all the stars for which any fit was found. The two figures show the same data, with the bottom plot not having the error bars to make it easier to see the data points. See Section 3.3.2 for more discussion.

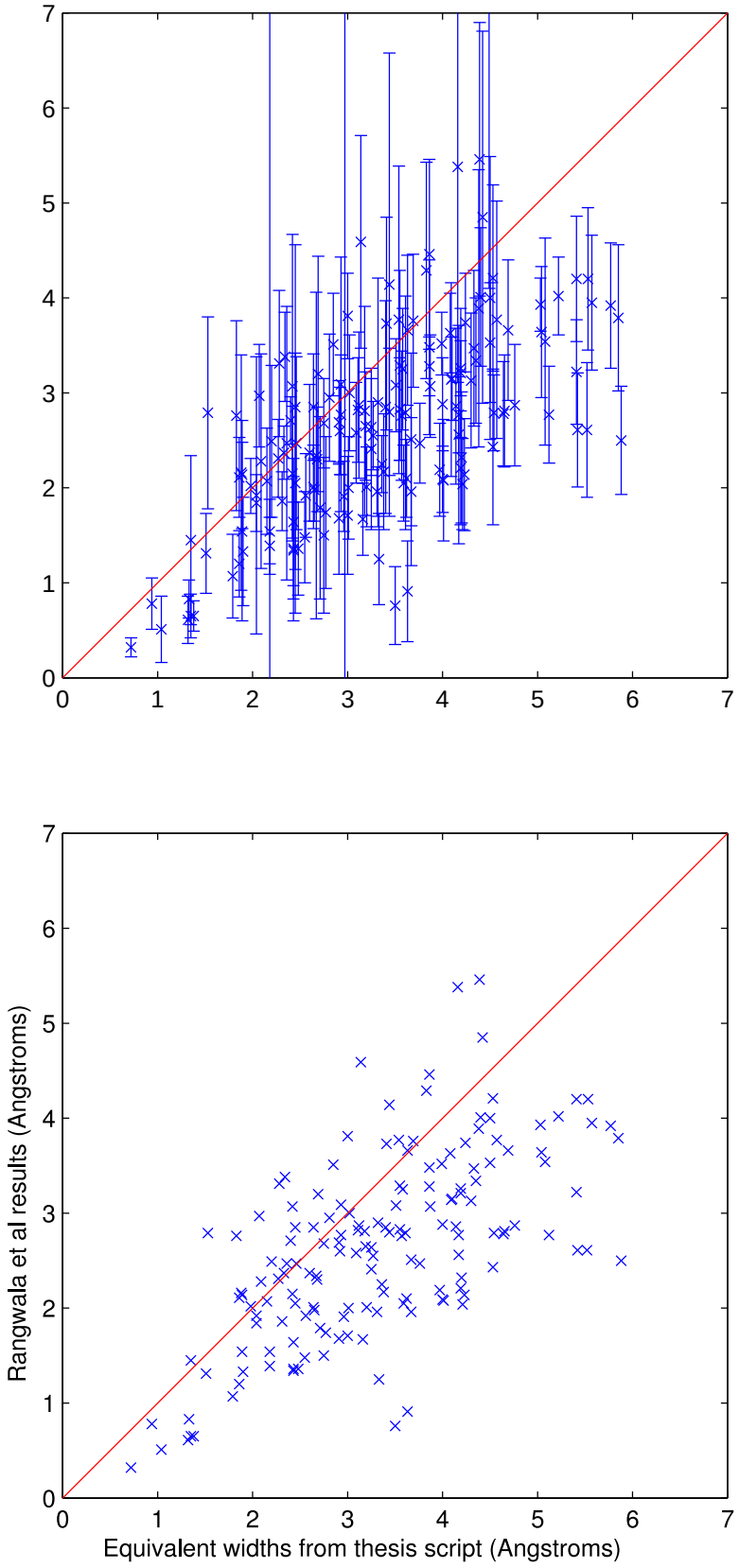

Figure 3.12: As for Figure 3.11 but showing only those stars for which the R statistic was less than 1.5. See Section 3.3.2 for more discussion.

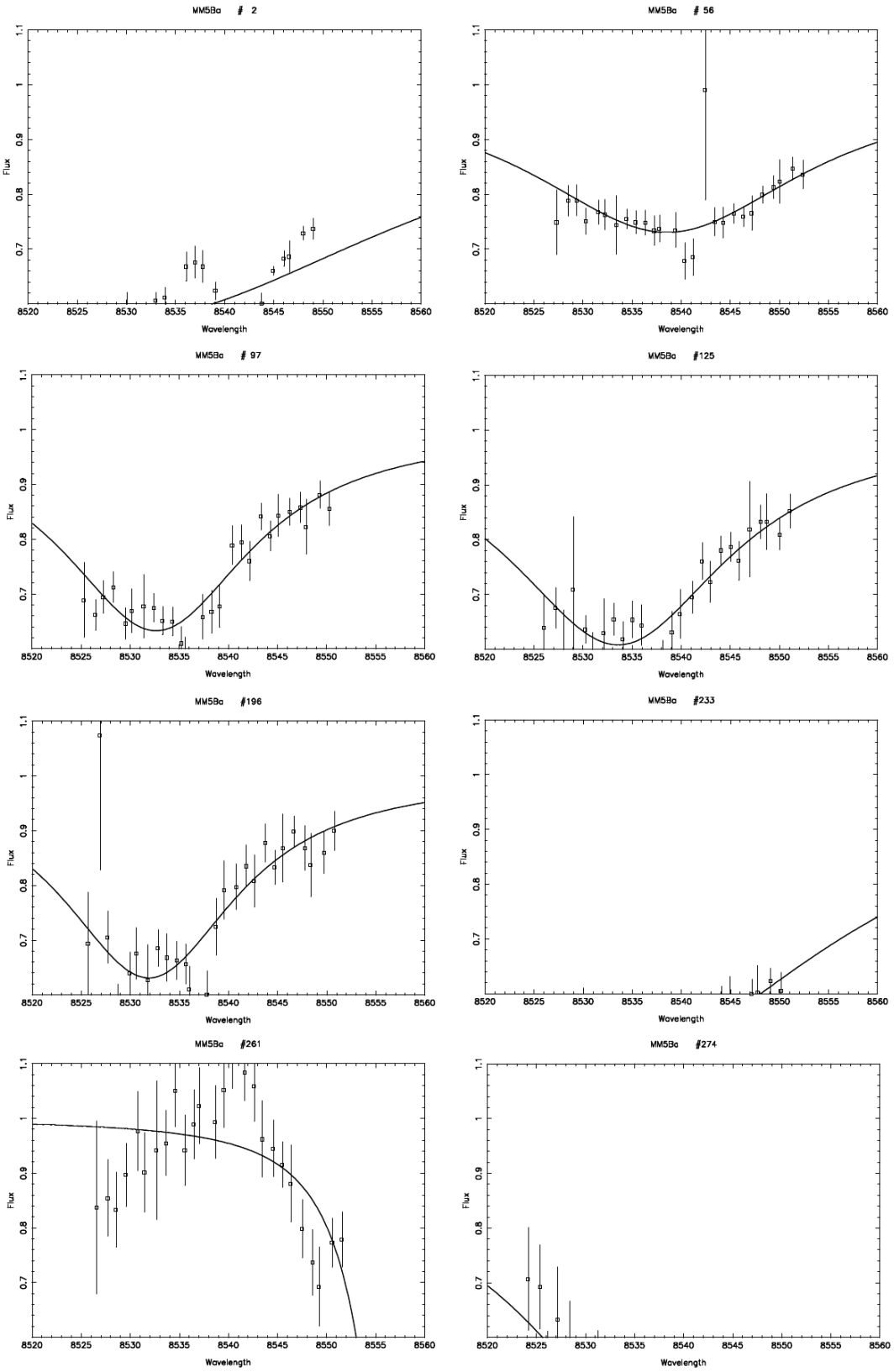

Figure 3.13: This figure is paired with Figure 3.14. It shows the fits from the Rangwala code which have the largest difference in equivalent width from the values found using the algorithm described in Section 3.2. Figures from Rangwala (2008). See Section 3.3.2 for more discussion.

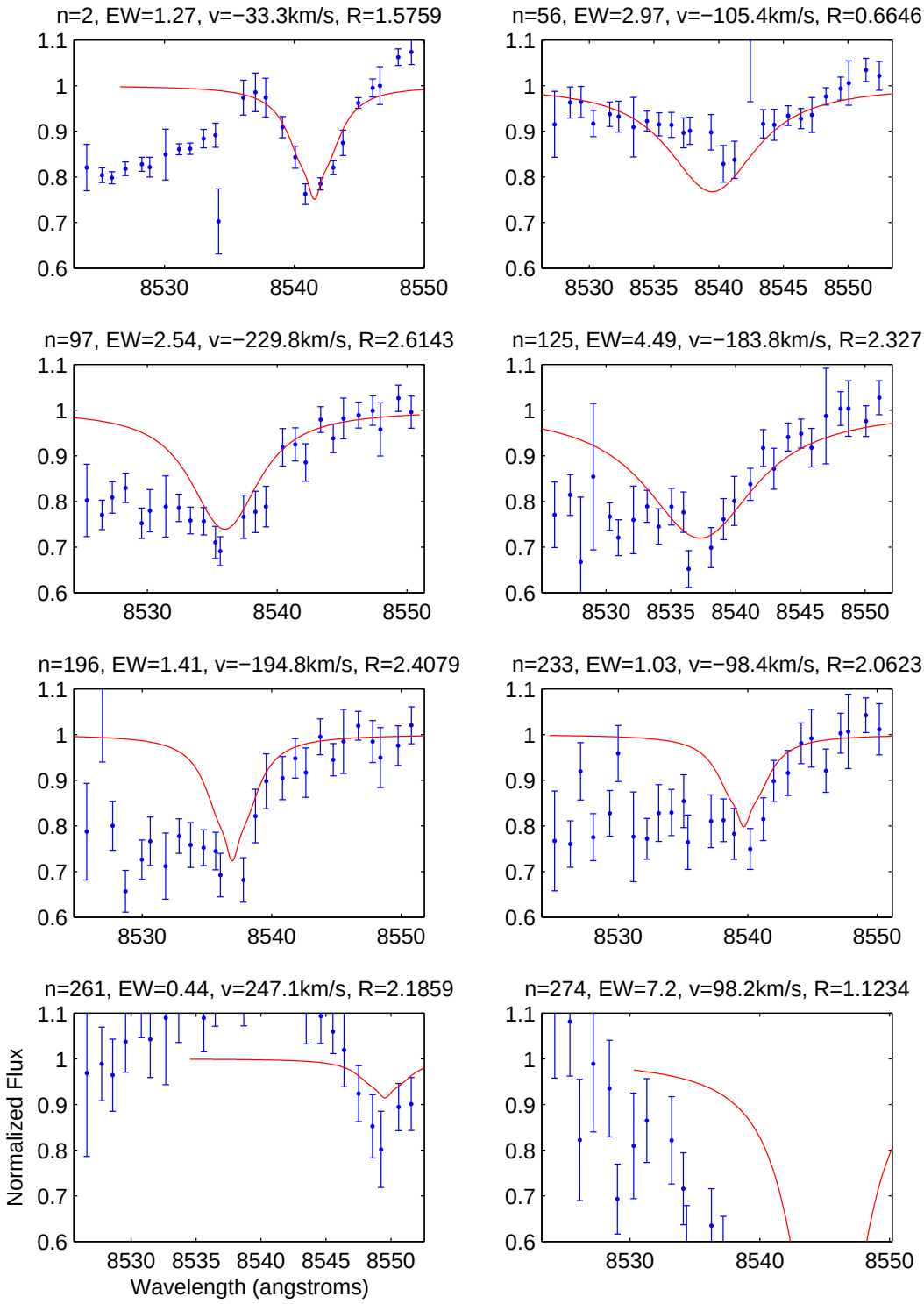

Figure 3.14: This figure is paired with Figure 3.13. It shows the fits from the code described in Section 3.2 for the same stars shown in the other figure. Comparing these figures shows that large differences between the two results are not caused by predominantly one of the fitting schemes. In some cases, it appears that the Rangwala code has fitted an erroneous continuum, while in other cases the scheme from this thesis has fitted a curve that is completely wrong. See Section 3.3.2 for more discussion.

equivalent width of 0.3 Å. This is of the order of the uncertainty in the equivalent widths found by Rangwala.

This underlines the importance of correctly determining the continuum level. Its placement can greatly affect the resulting equivalent width and any conclusions to be made from it in terms of finding the abundance of elements in stars.

The four biggest differences in continuum are shown in Figure 3.17. Here the Rangwala script is shown to be the culprit. Failing badly at determining the continuum values, it results in extremely large equivalent width values. This would be of critical importance to their research where they made conclusions about the metallicity of stars in the bulge based on their equivalent width values.

3.4 Photometry

The second dataset provided by Rangwala was 16 images of the same area of the sky as Section 3.3 and covering the same spectral line. They were taken in June 1999 on the 1.5-metre telescope of the Cerro Tololo Inter-American Observatory. The field of view was centred on RA 18:03:43.26 and Dec. -29:59:42.8 ($l = 1°$, $b = -4°$). They were all 900-second exposures.

Although the spectrum segments were useful in understanding the requirements for fitting to a discrete number of points, it removes the important steps of data reduction that go before it. In the case of FPI images these steps are performing photometry on the images and then normalizing the data.

The photometry step is well understood with a variety of tools available for such images. In this case DAOPHOT under PyRAF was used. DAOPHOT is a stellar photometry package designed by Peter Stetson at DAO to deal with crowded fields (Stetson 1987) and PyRAF is a command language for running IRAF tasks that is based on the Python scripting language.

A script was used to process the images individually. It is completely non-interactive, automatically accepting the PSF given for each star. In future work it would be desirable to understand this photometry to provide more precise data.

Although DAOPHOT does appear to have the ability to process images together and determine the common stars in each, this feature was not used. Instead a script was written in MATLAB that identified all the stars common to each image. This required

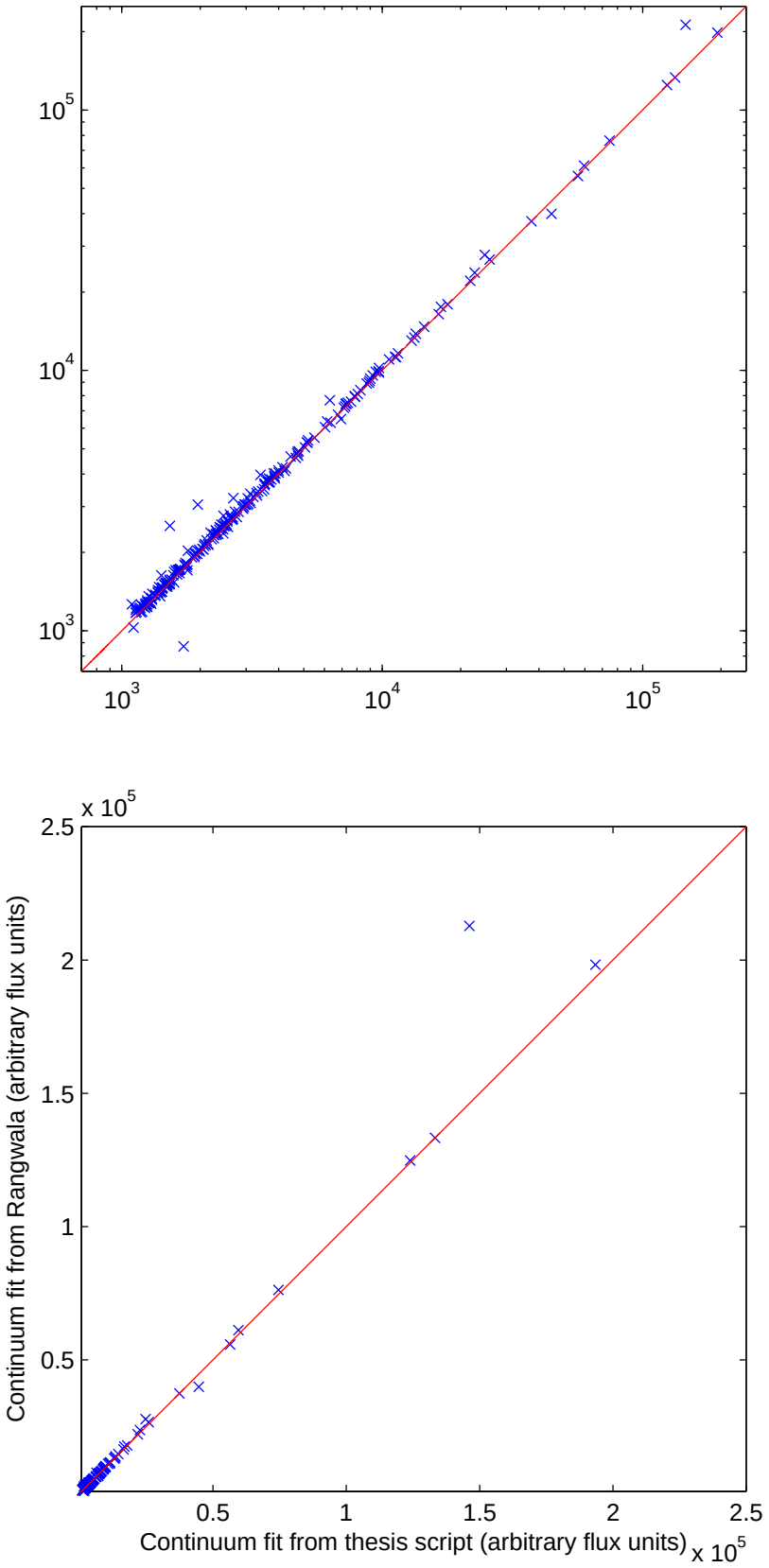

Figure 3.15: Comparison of the continua found by the two schemes. The top and bottom figures show the same data with the top figure plotted on a log-log scale to help show detail lost due to the large range in magnitude. See Section 3.3.3 for more discussion.

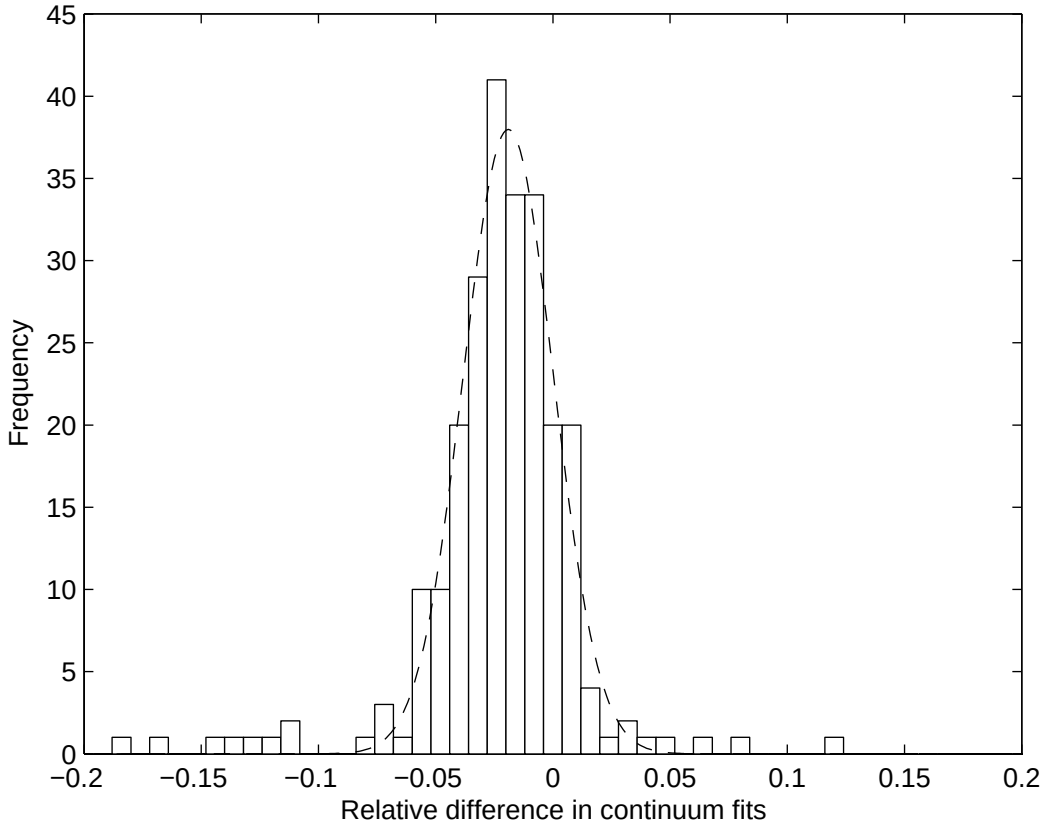

Figure 3.16: The relative difference between the continuum fits of Rangwala and the thesis. The fitted Gaussian has the parameters of $A = 38.0$, $\mu = -0.019$ and $\sigma = 0.019$. Not shown are the 4 stars which had difference greater than ± 0.2. Their profiles are given in Figure 3.17. See Section 3.3.3 for more discussion.

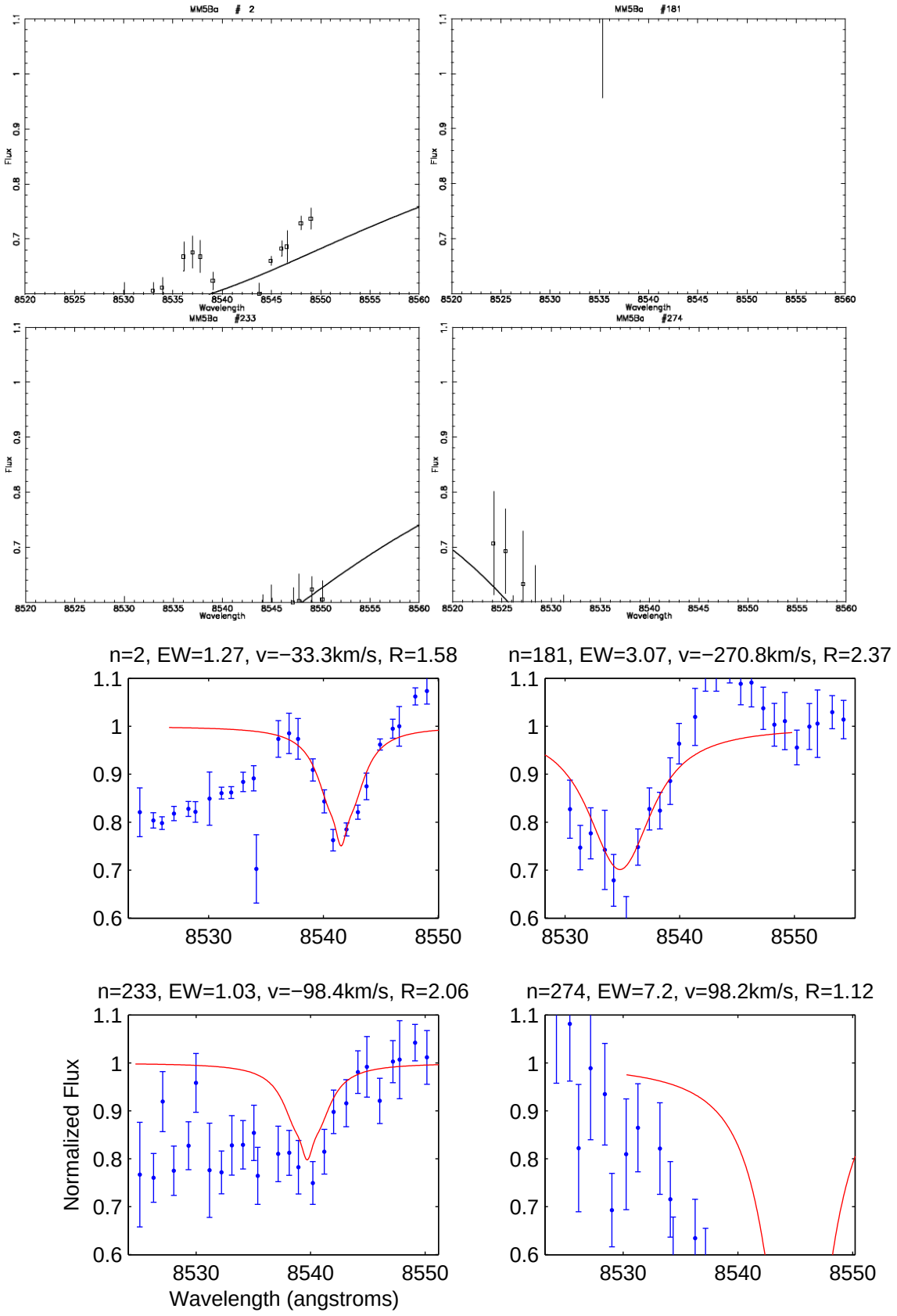

Figure 3.17: Plots from Rangwala (2008) and the thesis script showing those stars which had the biggest relative difference in continuum value from those found by the thesis script. These particular stars have abnormal spectra but the Rangwala method seems to have failed badly at determining the continuum level for them. See Section 3.3.3 for more discussion.

modifying an already existing MATLAB script for finding common elements in two arrays, to take, in theory, an infinite number of arrays. This code is included uncommented in Appendix A.2. With this it was possible to create an array for each star in the field with its magnitude and error from DAOPHOT.

With the images reduced it is now necessary to normalize them.

3.5 Flux normalization

One of the most important parts of the reduction process of FPI images is the flux normalization between each image. This is because in the time between the images, which can vary from minutes to years, the atmospheric transmission can change significantly. In the case of the images provided for this research, the images cover about 4.5 hours.

In instances of broad-bandpass photometry, it is usually possible to use standard stars for normalization. This star is known not to be varying intrinsically in brightness between the images and any variations are caused by effects in the Earth's atmosphere. In the case of narrow-bandpass photometry, as with an FPI, all the stars in the field can be assumed to be varying in brightness due to the changing positions in the spectral feature that is being sampled. In addition, due to the distance from the centre affecting the bandpass observed by the FPI, the stars will all be varying in different ways.

In theory for the FPI it would be possible to select a field that has a standard star in it. It would be required that this star have no spectral line in the wavelength range being imaged. This would severely limit the location of fields and the wavelength ranges observable. Since a standard star is not available, a different normalization scheme is required.

For an individual star, the spectral line being observed can be modelled by a Voigt profile. Assuming that most of the images were taken under average atmospheric transmission, a rough Voigt profile was fitted to the data. With a Voigt profile fitted to each star, the ratio of the data to the fitted function was then calculated. For each star, the signal-to-noise was calculated by finding the mean of the ratio of the flux value to the error. The stars with the 30 largest signal-to-noise ratios were used to find the mean flux normalization for each image. This process was iterated until the flux normalization required from the previous images converged to unity (Figure 3.19). The results of this can be seen in Figure 3.18. It shows how outliers are not really outliers but are images that were taken under less than ideal atmospheric conditions. The overall values found are given in Table 3.2.

This flux normalization method is also described in Rangwala et al. (2009), from where the idea originated.

One of the possible problems with such a normalization method is that it could create

Table 3.2: Flux normalizations found using the method described in Section 3.5. The wavelength is the central wavelength of the FPI used to acquire the image.

Wavelength (Å)	Flux normalization
8534	1.02
8535	0.98
8537	0.94
8538	1.09
8540	1.01
8541	1.04
8543	0.86
8544	1.07
8547	1.01
8549	1.04
8550	1.01
8552	0.89
8553	0.90
8555	1.17
8556	0.99
8558	1.01

"fake" signal out of noise. This is especially so if there is one very bright star, which drives all the Voigt profiles in a certain direction. Unfortunately there does not seem to be a way of avoiding this flux normalization scheme. With no standard stars in the field of view, there is no way of directly comparing images to determine how the sky has changed between exposures.

One task that should be undertaken is to apply the flux normalization scheme created for the second set of data from Rangwala on the spectrum segments. Since their normalizations values are known, it would make a good comparison and check for the method. With the caveat that their normalization values are for different images, their flux normalization values are much larger than those found in this thesis for the other images. Perhaps this is just an artifact of the particular images that they were using compared to the ones provided to for this thesis.

3.6 Results of photometry of images

There are no values with which to compare the data for this section (unlike Section 3.3), but the data can be compared to other studies of the Milky Way bulge region.

Figure 3.20 displays a histogram of the radial velocity determined for each star. It should be noted that there has been no heliocentric correction applied to these observations. Since all the images were acquired on one night this will be a constant systematic

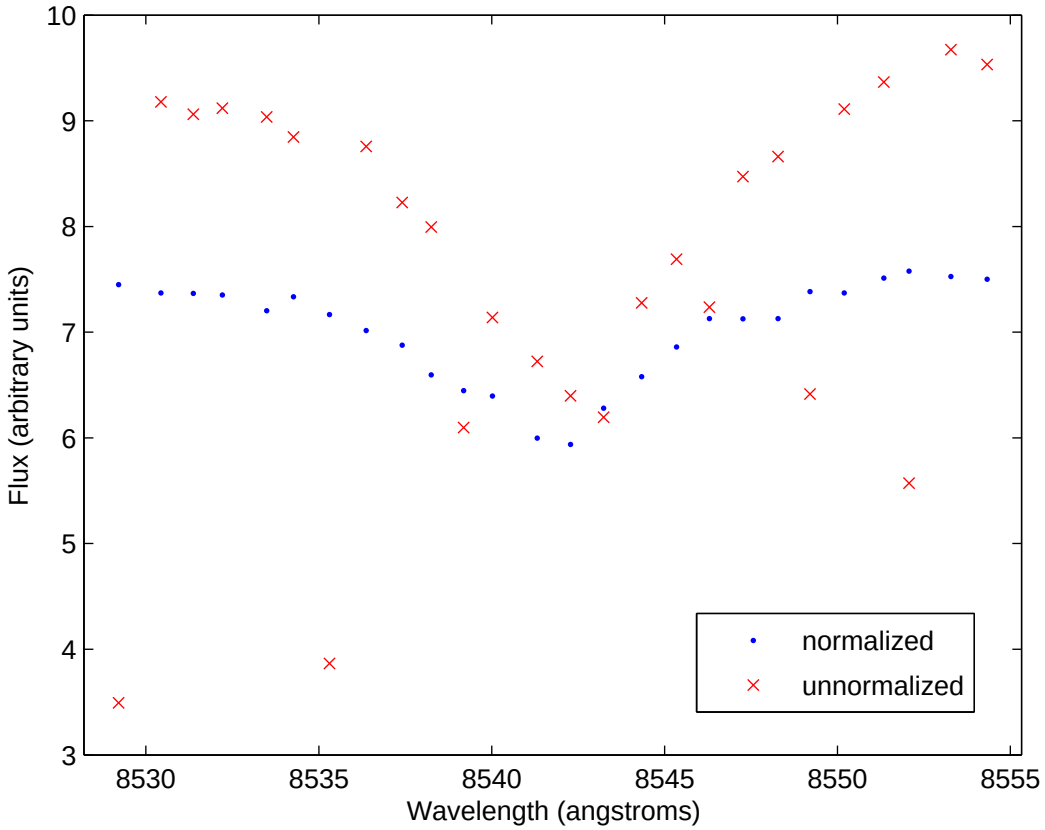

Figure 3.18: The difference between unnormalized and normalized data for one of the spectrum segments provided by Rangwala. The crosses show the raw data which follows the rough shape of a Voigt profile, except for some extreme outliers. These outliers disappear in the normalized data (dots). See Section 3.5 for more discussion of the flux normalization process.

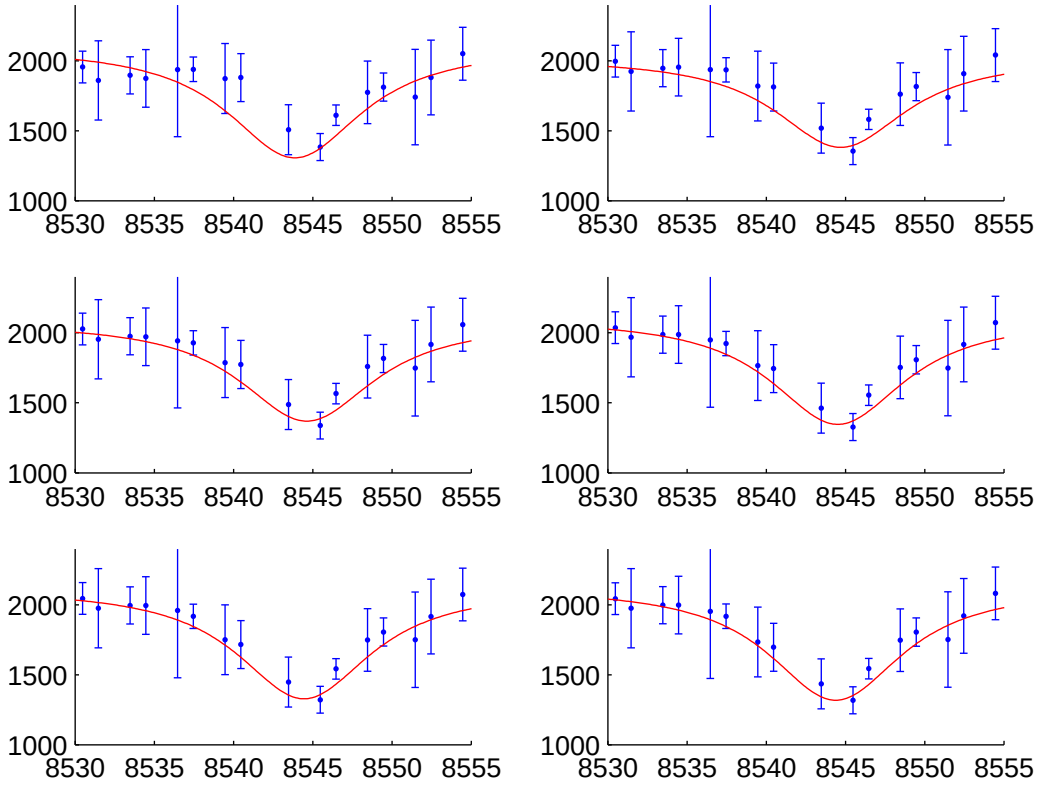

Figure 3.19: Plots showing the progression (left-to-right, descending) of the flux normalization. By the sixth iteration, the difference from the previous iteration is less than 1%. The shape of the fitted function does not vary greatly with each iteration, and most of the points do not change in position greatly.

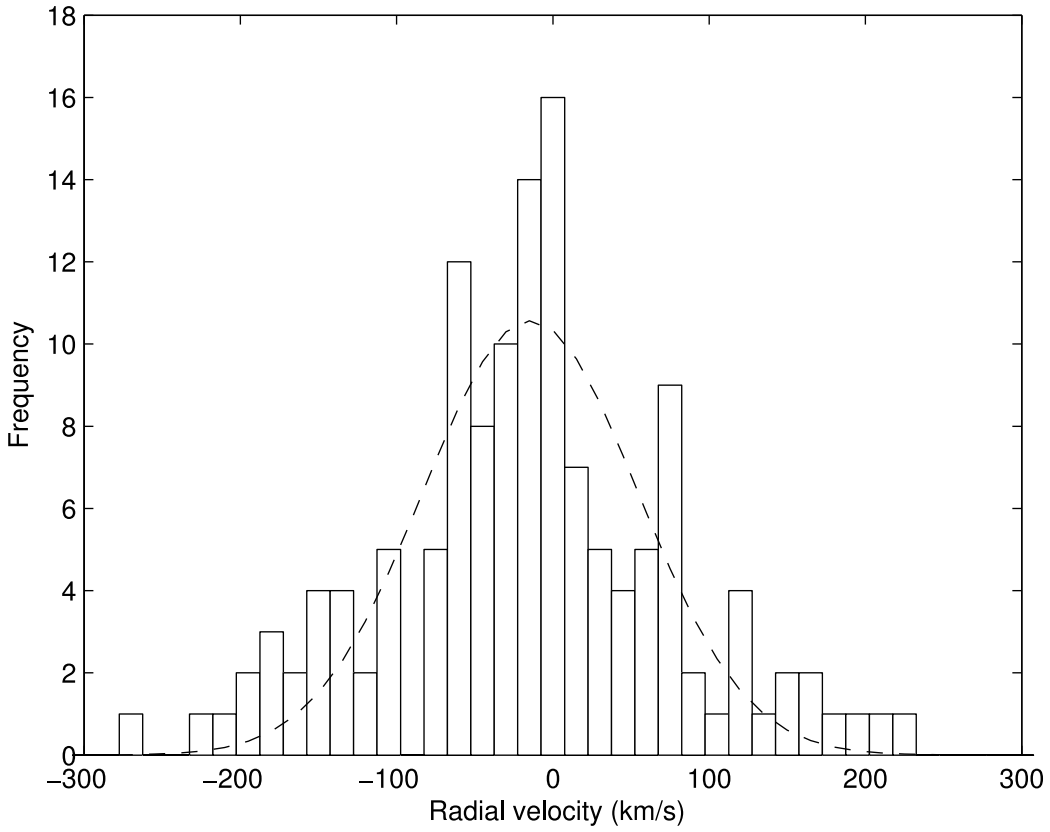

Figure 3.20: Distribution of radial velocity values found for stars in the images from Rangwala. The Gaussian curve has the values of $A = 10.6$, $\mu = -14.4$ km s^{-1} and $\sigma = 68.8$ km s^{-1}.

error in the data and so it was decided to ignore it for this research.

The best fit for the radial velocity histogram shown in Figure 3.20 is $A = 10.6$, $\mu = -14.4$ km s^{-1} and $\sigma = 68.8$ km s^{-1}. Comparing to Figure 3.10 which is taken from Rich et al. (2007), they appear to have much the same shape. These authors had found that for galactic coordinates $l = 1.04$ & $b = -3.95$, $\mu = -1.1 \pm 12.9$ km s^{-1} and $\sigma = 110.2 \pm 9.1$ km s^{-1}. There is however an almost factor of two difference in σ. The cause of this is unknown.

The equivalent width values are presented in Figure 3.21. A Gaussian curve has been fitted to the distribution, although this is almost certainly not the correct distribution for this data. It was merely fitted as an attempt to provide some statistics.

Since information on the temperature of the individual stars was not available until near the end of this research, it was not possible to calculate the actual abundance of calcium in the stars. Instead, the equivalent widths of the CaII line in Å is simply plotted in Figure 3.21. This show that most of the stars have equivalent widths in the 3 to 7 Å range and show a roughly Gaussian profile.

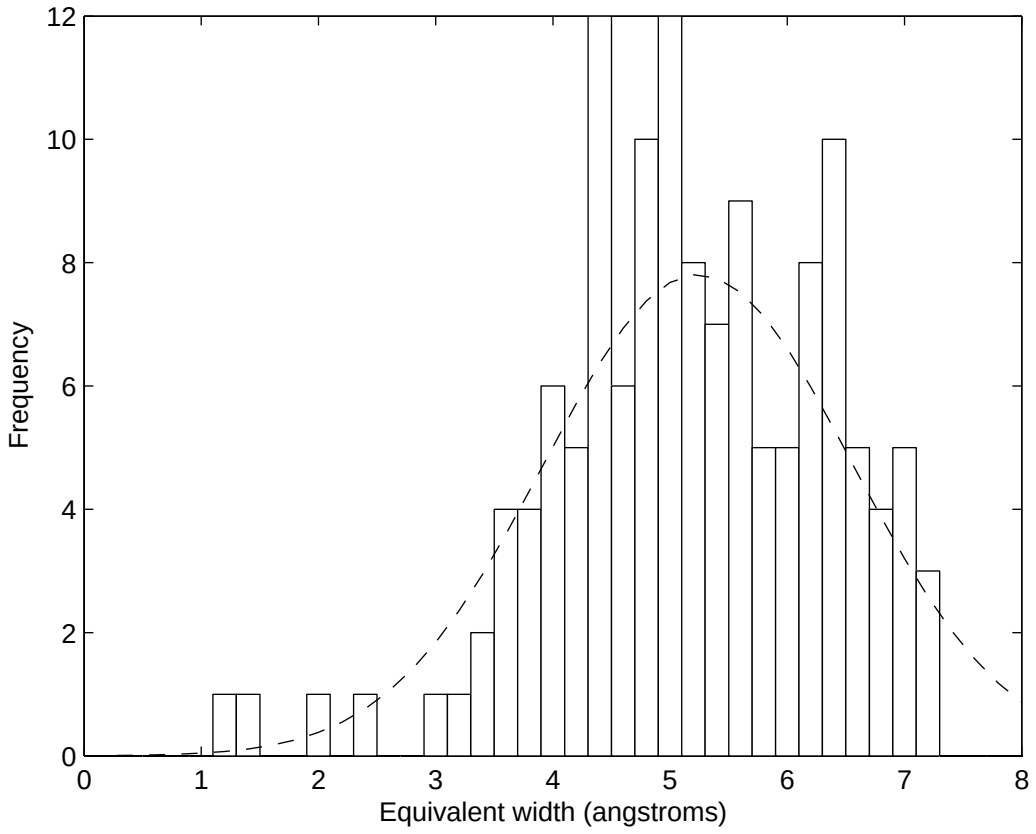

Figure 3.21: Distribution of abundance values (in Å) found for the stars in the images from Rangwala. $A = 7.81$, $\mu = 5.24$ Å, and $\sigma = 1.32$ Å.

3.7 Conclusions for this chapter

The techniques discussed in this chapter will be extremely useful for future research in this area. In particular, the knowledge learned from continuum determination and comparing a distribution to a discrete number of points will be particularly important.

One of the important lessons from this chapter is that the radial velocity can be more precisely determined than the equivalent width (and the subsequent abundance values). This is because the velocity relies on determining only one aspect of the line — the minimum. Whereas for the abundance, three pieces of information are required — the minimum, the half-width and the continuum. The abundance is very dependent on an accurate determination of the continuum, as was seen in the comparison of the biggest differences in equivalent width between this research and that of Rangwala.

Although the CaII line fitting was an important step in the process of elemental abundance determination using an FPI, the eventual aim of this research is to find abundances of s-process elements. Since the s-process lines do not have strong Voigt profiles, or are in clean regions of the spectrum, it will be necessary to fit a spectrum to the data, not just a calculated curve.

Chapter 4

Spectrum simulation

The main purpose of this research was to investigate whether it will be feasible to determine elemental abundances using the Fabry-Pérot interferometer (FPI). To this end, valuable experience was gained from the reduction of images of the singly-ionized calcium (CaII) spectral line, and the analysis of the data. This chapter concentrates on the process of simulating a line of an s-process element and the results that can be expected from observations of this line.

In Section 4.1 is a discussion of the selection process of the singly-ionized barium (BaII) spectral line and spectrum simulation. Section 4.2 describes the script that was written to fit the synthetic spectrum to the simulated data. Section 4.3 discusses the results found when comparing the inputted values to the outputted fits of the script.

4.1 Spectral line selection & atomic parameters

The main criteria for the line to be investigated was that it was a strong, unblended line of an element that is formed primarily through the s-process. An investigation of the literature, primarily in Moore (1972), showed that the best line was a singly-ionized line of barium at 6496.9 Å (Figure 4.1).

Although there are other unblended s-process lines, it was important that a strong line was chosen. There are two reasons for this. First, a strong line means that shorter exposures can be used, increasing the number of data points that can be acquired. Second, stronger lines have a larger width so that data points farther apart in wavelength can be used to define the spectral line. This allows for a larger field of view to be used as per Equation 2.22.

Examples of the other possible lines that could have been investigated are shown in Figure 4.2. These are the five strongest lines of BaII. 4554 Å and 4934 Å are from the first multiplet, while the other three are from the second multiplet. 4554 Å is in just as crowded a region as 6496.9 Å but even at high resolution it cannot be separated from a zirconium line at 4553.96 Å. Since this is also an s-process element, it would be impossible to extract abundances for these two species. The other lines suffer from similar problems,

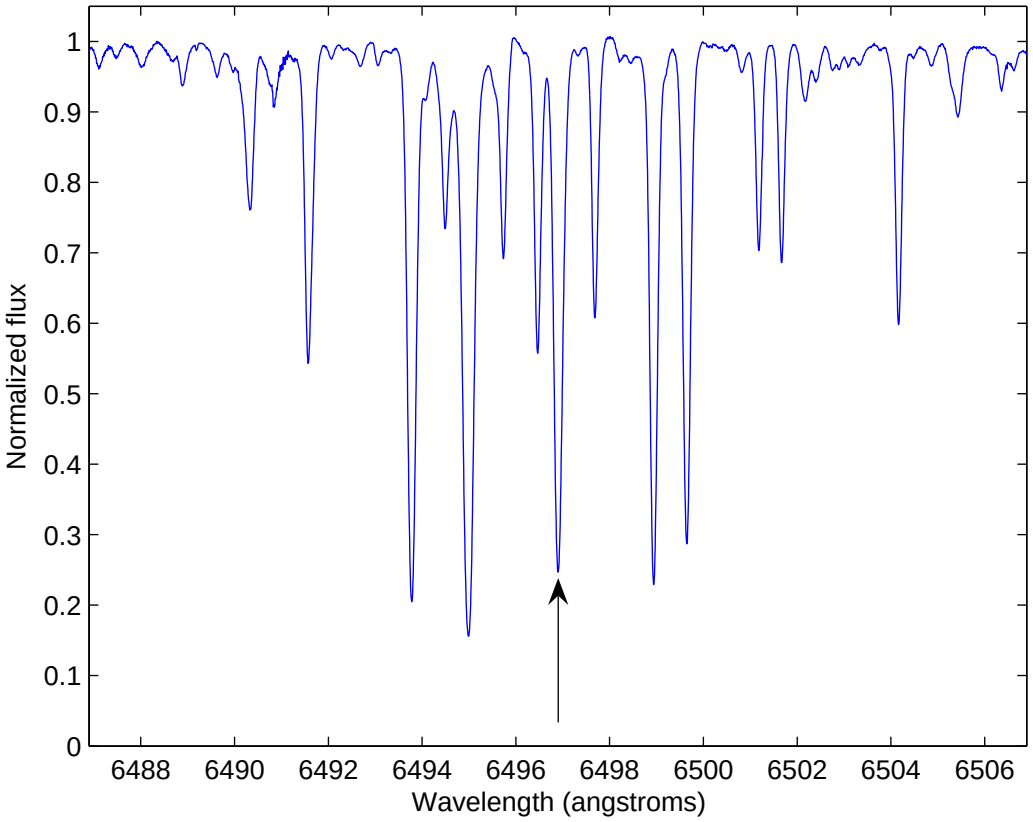

Figure 4.1: The section of spectrum containing the BaII line, marked with an arrow. This spectrum was taken from Arcturus (Hinkle et al. 2000).

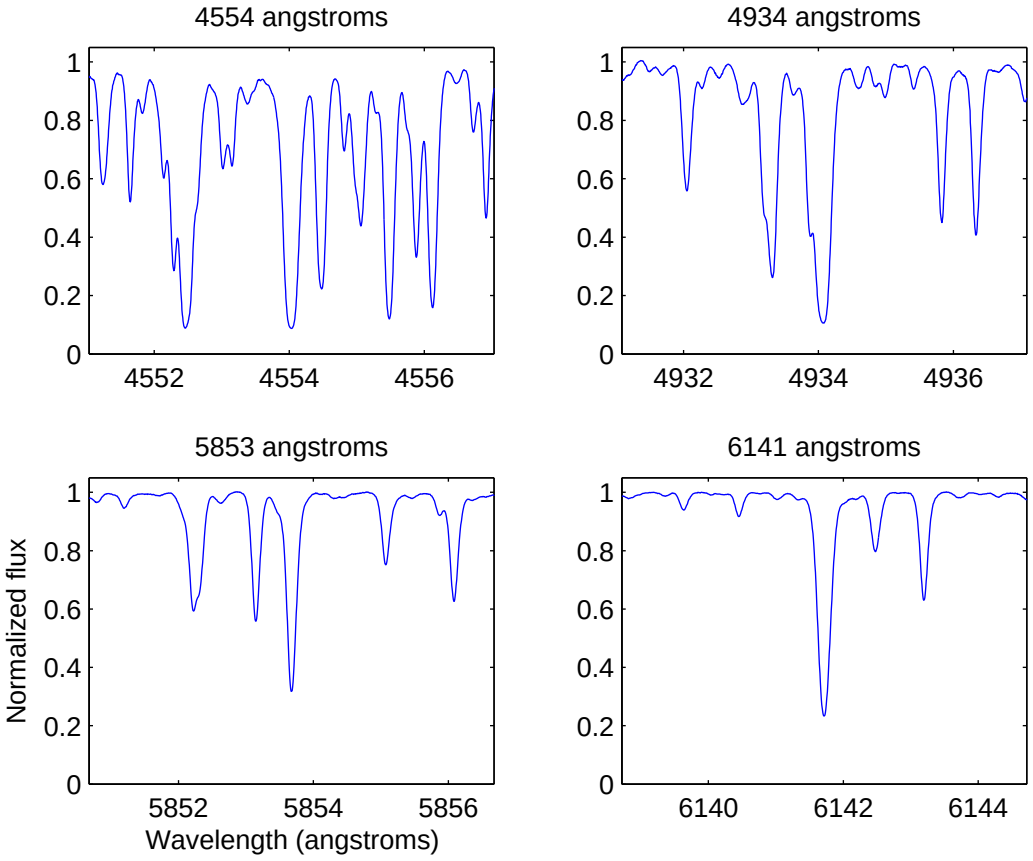

Figure 4.2: Examples of strong BaII lines that were considered for this research. All these spectrum segments are from Arcturus (Hinkle et al. 2000).

such as 5854 Å, which sits atop an aluminium line. Only 6496.9 Å was found to be completely unblended at high resolution.

In order to fully cover the region, a 30 Å section of spectrum was selected that included the strong BaII feature. Although the line only covers about 1 Å, it was necessary to consider the wavelength variation that occurs across the field of view of an FPI system (Equation 2.22).

With the aim of this research being to find abundances for stars along the giant branch and main sequence of 47 Tuc, it was necessary to produce synthetic spectra for a wide range of stellar atmospheres. MOOG[1] was used to produce synthetic spectra. MOOG is a stellar line analysis package developed by Chris Sneden at the University of Texas at Austin, as part of his PhD (Sneden 1973) and has been updated regularly. The version used in this project was released in 2002. It is written in FORTRAN code and uses local thermodynamic equilibrium equations to generate a synthetic spectrum based on a spectral line list and a stellar atmosphere model.

[1] `http://verdi.as.utexas.edu/moog.html`

The first task was to build up a spectral line list that had parameters that provided good fits to observational data. For atomic lines there are five parameters of interest — wavelength, excitation potential, oscillator strength ($\log gf$), damping paremeters and hyperfine splitting (Gratton 1999). The first two generally require little correction and have been extensively investigated with accurate tables being produced, such as by Kurucz (1993). However, for this research corrections were required to the $\log gf$ values.

The method used was to compare the synthetic spectrum with high-resolution spectra of the Sun (Delbouille et al. 1973) and Arcturus (Hinkle et al. 2000). The $\log gf$ values in the line list were corrected to fit the synthetic spectrum to high-resolution spectra.

The model stellar atmospheres used were produced by Robert Kurucz at the Harvard-Smithsonian Center for Astrophysics[2]. Although stars come with a wide variety of temperatures, only one type of star was used as the basis for the synthetic spectra — a 4,500 K giant-branch star.

4.2 Multiple fitting of line profiles

In order to determine the abundance, several pieces of information are required about the star. From the star's position in the colour-magnitude diagram, it will be possible to estimate its surface temperature and gravity. As such, this is a two-parameter problem — determining the radial velocity of the star and the abundance of barium in the star. Both of these can be done simultaneously. Due to the small parameter space, it was decided to determine these values using a brute-force method of exhaustively examining all possible values and finding the best fit through a least squares minimization.

This section describes the MATLAB code that was developed for this purpose. It features portions of the code, with the full code being found in Appendix A.3.

```
load('spec4500_45.mat')
spectrum4500(:,2:42)=1-spectrum4500(:,2:42);
waves=spectrum4500(:,1);
wavelengths=[6487.2 6487.5 6487.8 [6495.50:(2.5)/9:6498.00] 6502.8 6503.0 6503.3];
signaltonoise=100;
```

Throughout the testing, synthetic spectra produced for an AGB star of $T_{\rm eff} = 4,500$ K was used. As described in Section 4.1, this was produced by MOOG. The normalized spectra were preformatted into a large array that was loaded into MATLAB. For this work, it was more useful to have the continuum at zero and no flux at one.

The variable `wavelengths` set the particular wavelengths that the script would "observe". If the star was at the centre of the field and had no radial velocity shift, then the first- and last-three wavelength points were situated where there was no flux depression

[2] `http://kurucz.harvard.edu`

due to any spectral lines. They sampled the continuum. The middle points covered the BaII line.

```
[data velshift abund R continuum_initial]=fpidata(wavelengths,signaltonoise);
```

The data to which the synthetic spectrum would be fitted was produced by a separate function called `fpidata.m`. This took in the wavelength positions and the signal-to-noise ratio (S/N) to be used. Below are some portions of the code from this function,

```
R=350*rand(1);
wavelengths=wavelengths/(sqrt(1+(R/22000)^2));
velshift=floor(25*randn(1))/100;
abund=floor(-20 + 40*rand(1))/20;
```

As discussed in Section 2.2, specifically Equation 2.22, the position in the field of view affects the wavelength that is observed by the FPI. So the first randomized thing was the position in the field. This was in pixel numbers. Although the field of view had a larger radius than 350 pixels, anything larger than this shifted the spectrum too far and the BaII would not be observed.

A random radial velocity shift is then found. Since the velocity dispersion is to first-order normally distributed, the velocity shift is produced by the `randn` function of MATLAB. This produces a random number from a normal distribution with $\mu = 0$ and $\sigma = 1$. In the code this velocity shift is not computed in $\mathrm{km\,s^{-1}}$, but instead is in the array index. It can be converted to $\mathrm{km\,s^{-1}}$ for comparison with real spectra.

The last randomly generated value is the abundance of barium in the star. From MOOG, synthetic spectra were calculated from -1.00 to $+1.00$ dex around the solar barium abundance in 0.05 dex steps. As such there are 40 possible values for the variable `abund`.

```
continuum_initial=signaltonoise^2+signaltonoise*rand(1,1);
```

Instead of having the data still normalized to one, the data was multiplied by $[(\mathrm{S/N})^2 + X \times \mathrm{S/N}]$, where X is the output of `rand`[3] to provide some random "noise" in the synthetic data.

The flux values were randomly adjusted by adding to them

$$X(\mathrm{S/N})^{-1}. \tag{4.1}$$

For objects with high S/N, the random amount that the flux is adjusted by is small.

The random velocity shift, position in the field and abundance were then used to create an array of data containing wavelengths, flux values and flux errors. Once the random data had been created, it was passed back to the original script.

[3] MATLAB script that produces a random number from -1 to $+1$.

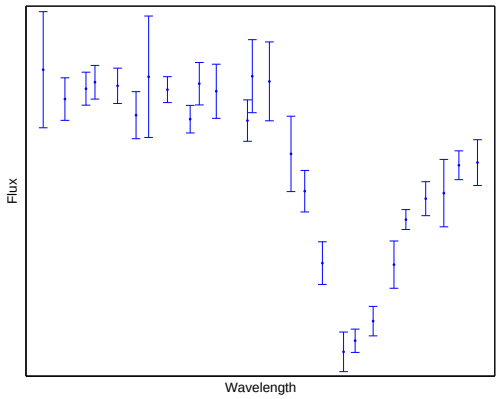

Figure 4.3: Example of CaII line where the reddest data points are not on the continuum. Using the three reddest and three bluest points to find the continuum would result in an erroneous value. This is avoided by comparing the left and right sides.

The next task was to determine the velocity shift and abundance from this adjusted synthetic data. The first step in this process was to find the continuum.

```
mean_left=sum(data(1:3,2)./data(1:3,3).^2)/sum(1./data(1:3,3).^2);
mean_right=sum(data(length(wavelengths)-2:length(wavelengths),2)
           ./data(length(wavelengths)-2:length(wavelengths),3).^2)
           /sum(1./data(length(wavelengths)-2:length(wavelengths),3).^2);
if abs(mean_left-mean_right)/mean_left>0.01
    continuum=max([mean_left mean_right]);
else
    continuum=mean([mean_left mean_right]);
end
```

Since the profile of the spectrum segment was known, points that are on the continuum were selected. In this case it was the far-left and far-right portions of the data. Even if the spectral line was shifted by the radial velocity and/or position in the FOV, either the left or right side should have contained the continuum.

From the data analysis of the CaII line described in Chapter 3, it was found to be important to make sure to compare the left and right sides to each other. If the left and right sides were just averaged, then a highly depressed side could drag the continuum level down (e.g. Figure 4.3). If the continuum levels of the left and right sides differed by more than 1%, then the script selected the highest value.

Once the continuum level had been determined, the spectrum could be normalized. This made it easier to fit the spectrum back to the data, since the synthetic spectra were normalized.

The determination of the velocity and abundance was performed with nested `for`

loops. Since there were many local minima in the parameter space, the easiest method for finding the best fitting values of velocity and abundance was to examine the entire space via a brute force method. This is feasible in the velocity space because the velocity dispersion of 47 Tuc is about 12 $\mathrm{km\,s^{-1}}$ (Meylan & Mayor 1986). This equates to a change in wavelength of only 0.26 Å from the rest wavelength.

The fit of the synthetic spectrum to the adjusted data was determined in the same way as described in Section 3.2, specifically Equation 3.9.

When the script was run for just one star, the script outputted two plots, as shown with two examples in Figures 4.4 and 4.5. The top plot in each of these figures has the inputted spectrum, the fitted spectrum, the inputted points that were used and the corresponding points on the fitted spectrum. The bottom plot shows how good the correlation was between the inputted and fitted spectra. In the case of Figure 4.4, this is clearly an excellent fit, since the points fall almost exactly on the one-to-one line, whereas in Figure 4.5, the points are scattered about the line. This is because the fit that the script has come up with is wrong in both the abundance value and the radial velocity.

4.3 Predictions of simulations

The main purpose of the simulations was to determine how precisely one can recover the inputted parameters. In particular what will be the range of uncertainties with different wavelength resolution, signal-to-noise ratio and distance from the centre of the image.

Simulation runs were over 10,000 stars. This also gave an idea of the time it will take to process the real data. For 10,000 stars it took on average about 10 minutes. Since the aim is to obtain data for less than 1,000 stars, data analysis will be quick to perform.

As the inputted values are known, the fitted result can be compared for the abundance, velocity and continuum. Overall, the continuum and the radial velocity were found more precisely than the abundance. The abundance is affected by the determination of the continuum, wavelength shifts due to the radial velocity and position in the FOV and by the number of sampling points covering the spectral line.

4.3.1 Number of data points

The first results presented here are for changing the number of data points. Throughout these simulations there were always 6 points defining the continuum. The number of points that were being varied were the points covering the spectral line. They were evenly divided between 6495.5 Å and 6498.0 Å. So for two points, there were data points at 6495.5Å and 6498.0Å, while for four, there were points at 6495.5 Å, 6496.3 Å, 6497.2 Å and 6498.0 Å. The only variation from this was for the one-point plot. Here the data point was placed at 6497.2 Åwhich was the closest of these points to the centre of the

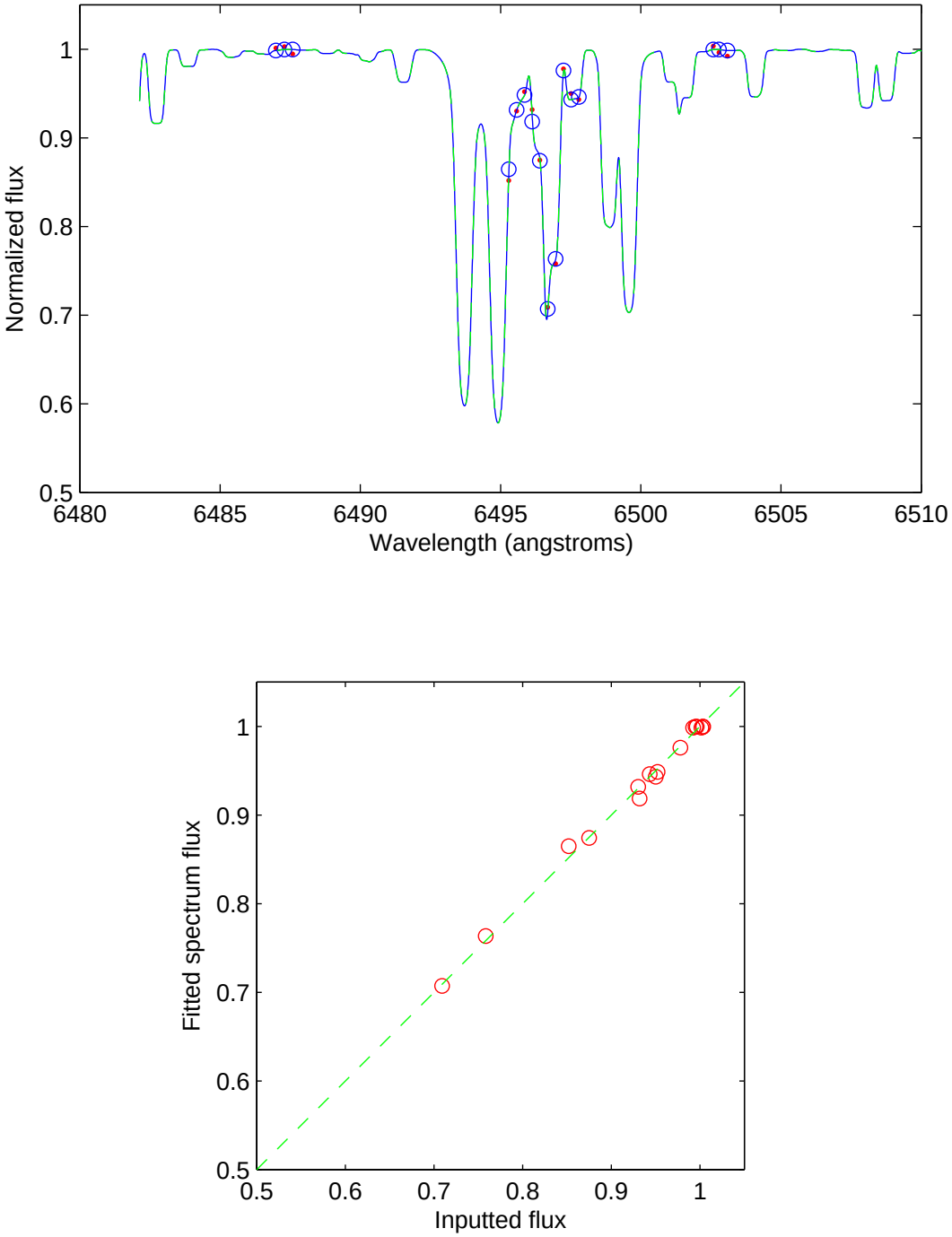

Figure 4.4: An example of a perfect fit as found by the script described in Section 4.2. The top graph shows the fitted spectrum (solid line) and the inputted source spectrum (dashed line) are plotted over the top of each other. The points are the simulated data, while the circles show the point on the fitted spectrum that is at the same wavelength as the data. The bottom plot shows the correlation between the fitted spectrum and the data. The dashed one-to-one line shows a perfect fit.

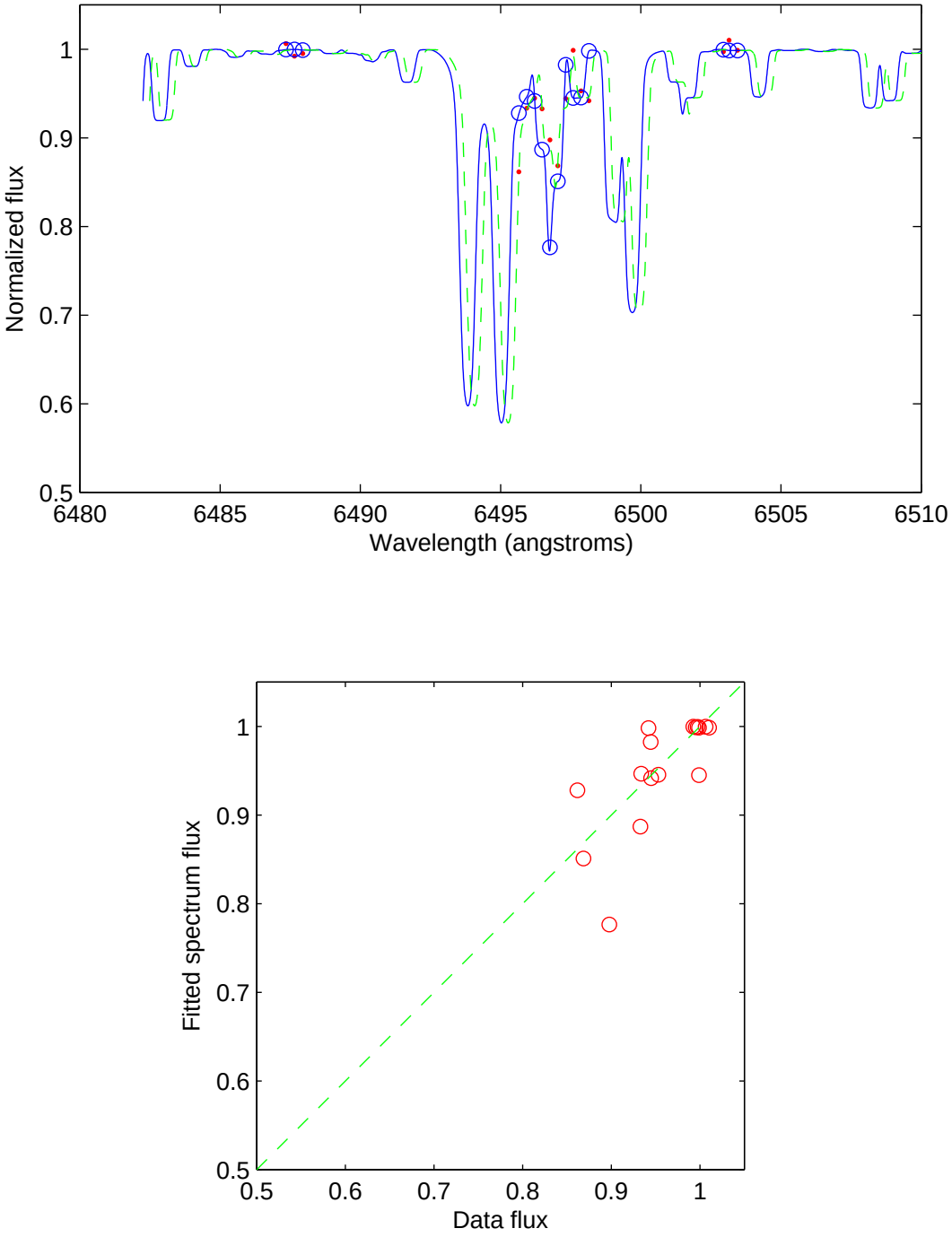

Figure 4.5: An example of a bad fit as found by the script described in Section 4.2. The top graph shows the fitted spectrum (solid line) and the inputted source spectrum (dashed line) are very different. The points are the simulated data, while the circles show the point on the fitted spectrum that is at the same wavelength as the data. The bottom plot shows the correlation between the fitted spectrum and the data. The dashed one-to-one line shows a perfect fit.

line.

Changing the number of points does not affect the determination of the velocity greatly (as shown in Figure 4.6 and Table 4.1). The data points 6495.5 Å and 6498.0Å are common to all the sets of data. These two points fall outside the range of the BaII spectral line and they are not affected by any abundance changes. In addition to this, there is no noise introduced into the wavelength information provided from `fpidata`. In other words, as long as there is at least some data coming from a spectral line, the velocity can be determined to some precision.

The abundance variation is shown to be very dependent on the placement of the data points. With only two points, the spectral line is "observed" at 6495.5 Å and 6498.0 Å, which do not fall in the spectral extent of the BaII line. This means that it is little more than luck if the script results in the correct value. The top-centre histogram in Figure 4.7 (whose parameters are given in Table 4.2) shows that it is almost a flat distribution.

Since the profiles in Figure 4.7 appear asymmetric, a Gaussian distribution was fitted and the parameters determined, including the skewness and kurtosis. The fitting of the Gaussian was done in the same way as described in Section 3.3.1. The skewness (y) of the distributions was found using the MATLAB `skewness` function, defined as

$$y = \frac{E(x-\mu)^3}{\sigma^3}, \tag{4.2}$$

where μ is the mean of x, σ is the standard deviation and $E(t)$ represents the expected values of the quantity of t. If skewness is negative, the data are spread out more to the left of the mean than to the right. If skewness is positive, the data are spread out more to the right. The skewness of the normal distribution (or any perfectly symmetric distribution) is zero.

The kurtosis (k) is a measure of how outlier-prone a distribution is, with the kurtosis of the normal distribution being equal to three. A high kurtosis distribution has a sharper peak and longer, fatter tails, while a low kurtosis distribution has a more rounded peak and shorter thinner tails. Like the skewness, it was calculated using the MATLAB `kurtosis` function. It is defined as

$$k = \frac{E(x-\mu)^4}{\sigma^4}. \tag{4.3}$$

Examples of kurtosis of different distributions is given in Table 4.3.

For the velocity and abundance error distributions, the Gaussian parameters are presented in Tables 4.1 and 4.2 respectively. These parameters confirm the qualitative assessments that can be made from looking at the plots — for large numbers of points, the radial velocity error distributions are very stable, especially A, μ and σ values.

These same radial velocity error plots also show a definite skewness to the right, with all but one of the plots in Figure 4.6 showing a positive skewness. For these plots, a

Table 4.1: Gaussian parameters for Figure 4.6, the radial velocity error distributions from varying the number of points covering the BaII spectral feature (Section 4.3.1).

№ of points	Peak value A	μ ($\mathrm{km\,s^{-1}}$)	σ ($\mathrm{km\,s^{-1}}$)	skewness	kurtosis
1	290	0.7	5.9	0.3	3.5
2	2440	−0.1	0.6	−2.1	18
4	940	0.1	1.6	0.9	11
7	920	0.0	1.7	2.1	10
10	850	0.0	1.9	1.5	7.8
13	980	0.0	1.7	1.4	8.6
16	990	0.1	1.7	1.6	9.2
19	969	0.1	1.7	1.4	8.2

positive skewness indicates that the script tends to fit a value smaller than the inputted value. Looking at the plots, this skewness is not caused by asymmetry per se, but by a bump on the right-hand side. The origin for this bump is found when the fitted values are investigated. Instead of being a slightly normal distribution, as would be expected since the inputted values were from a normal distribution, there is a definite asymmetry. When only stars that have errors greater than zero are used, then there is a dearth of stars fitted with the highest radial velocities.

The contour plots (Figure 4.8) show interesting behaviour. These combine the information from the histograms into a two-dimensional representation of the parameter space. With only one point, they show that there is a diagonal trend across the space. Stars are either fitted with smaller velocity and abundance than that inputted, or to have a larger velocity and abundance. This trend seems to continue through all contour plots in Figure 4.8. As more points are added, this diagonal region diminishes in size and also becomes narrower. Confirming the behaviour seen in the histograms, increasing the wavelength sampling does not seem to decrease the error in the fitted value significantly for either abundance or velocity.

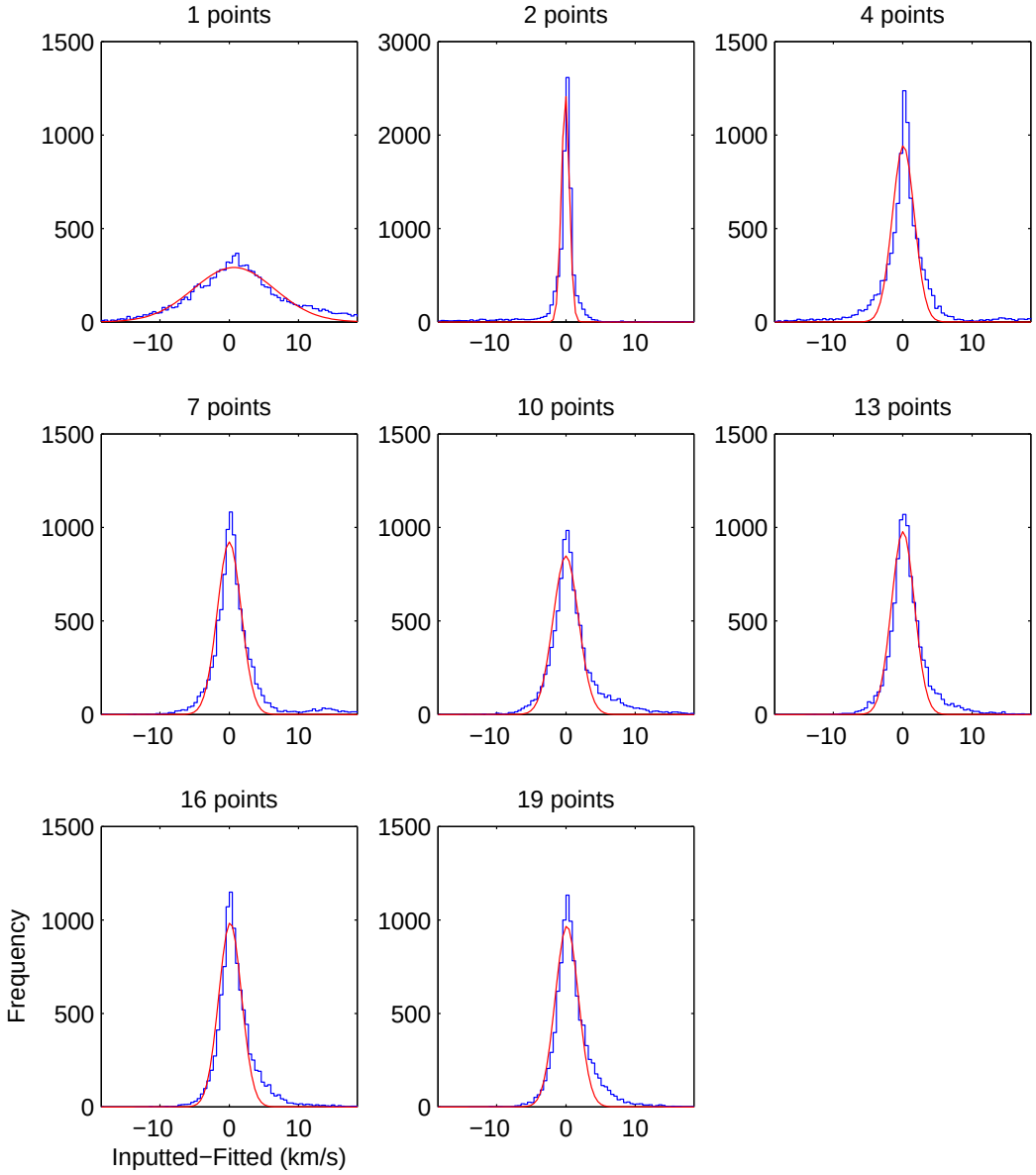

Figure 4.6: Error in velocity with changing number of points covering the spectral line as discussed in Section 4.3.1. Unlike with the abundance (Figure 4.7), the velocity is not nearly as affected by reducing the number of points. The 2-point plot has the narrowest error distribution. The reason for this is the placement of the data points. They fall outside the range of the BaII line and therefore are unaffected by the changing abundance.

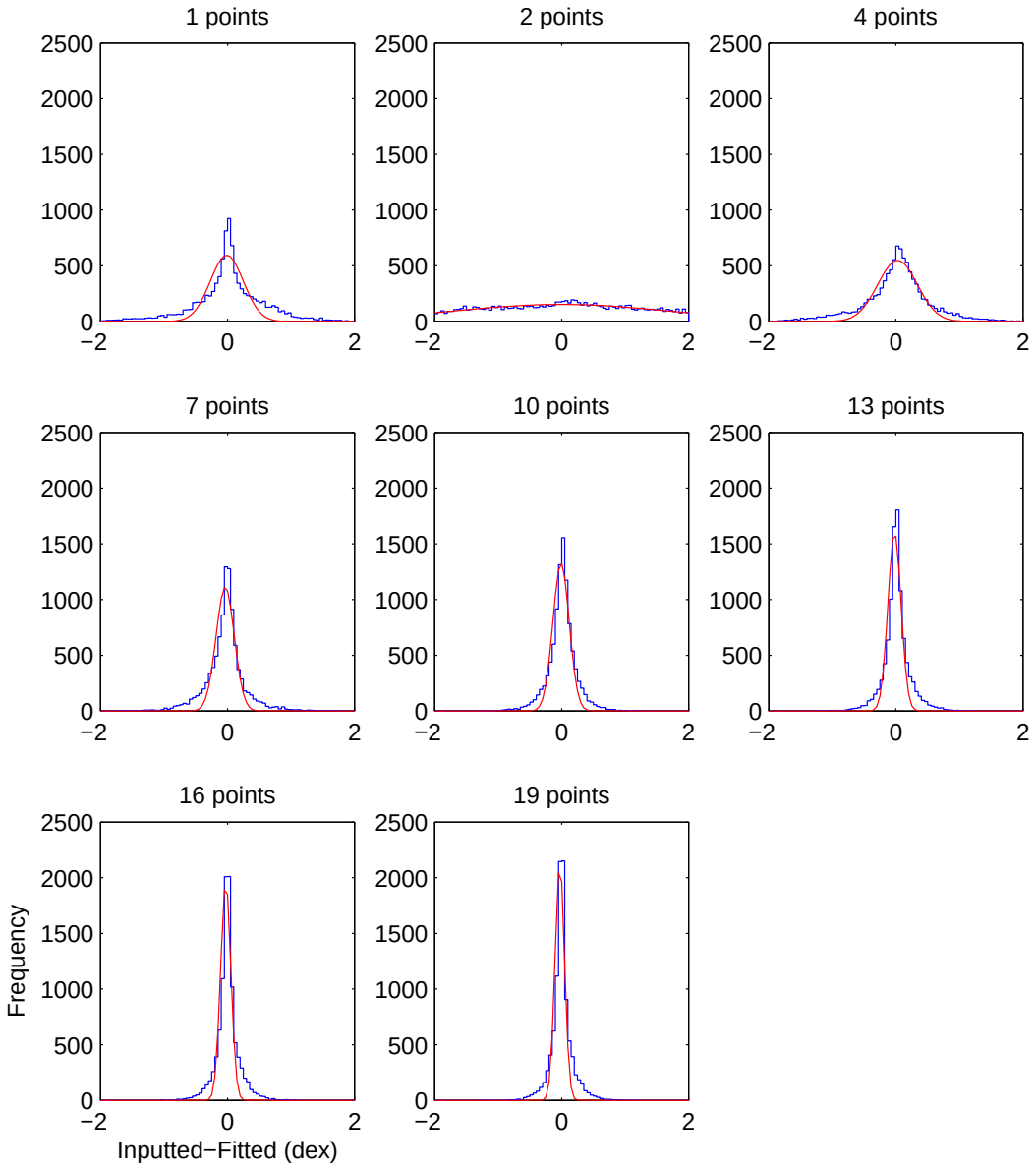

Figure 4.7: The error in the determined abundance varies with the number of data points covering the BaII spectral line, as discussed in Section 4.3.1. At two points it is almost completely random. This is actually not the fault of just having two points but the placement of the two points. They fall outside the range of the BaII spectral line. For the one point plot, a point was placed in the middle of the BaII line. The difference between 10 and 16 points appears to be negligible and even 7 points looks to provide minimum errors.

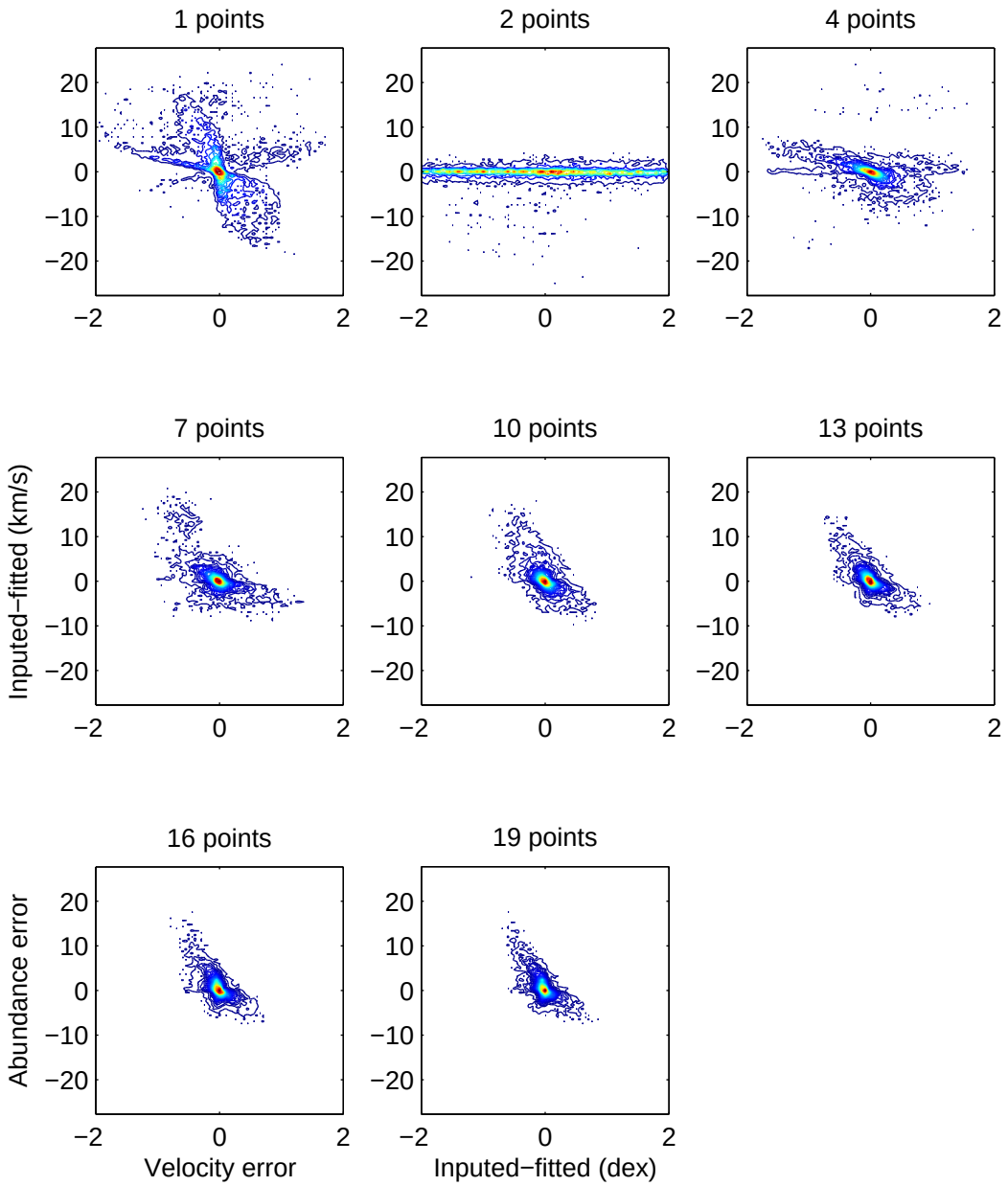

Figure 4.8: Combining the information from Figure 4.6 and 4.7 into a contour plot as discussed in Section 4.3.1. This clearly illustrates the almost random abundance that is determined with only two points covering the spectral line region. Since the velocity was relatively unaffected by the number of points, these contour plots merely reiterate what was seen from the abundance plot in Figure 4.7. The difference between the plots for 13 and 16 points are negligible, meaning that adding more points will probably not increase the quality of the information. The contours have a spacing of five units, starting at 2 and with a maximum of 8000.

Table 4.2: As for Table 4.1 but for Figure 4.7, the abundance error distributions from varying the number of points covering the BaII spectral feature (Section 4.3.1).

№ of points	Peak value A	μ (dex)	σ (dex)	skewness	kurtosis
1	590	0.0	0.3	−0.2	4.5
2	150	0.0	1.7	0.0	2.0
4	5508	0.0	0.3	−0.2	4.4
7	1110	0.0	0.1	0.0	7.0
10	1330	0.0	0.1	−0.2	6.8
13	1610	0.0	0.1	0.2	6.5
16	1960	0.0	0.1	0.2	6.8
19	2120	0.0	0.1	0.2	7.1

Table 4.3: Examples of the kurtosis of different distributions (Weisstein 2009) . The kurtosis is defined in Equation 4.3.

Distribution	kurtosis
Gaussian	3
Lorentzian	undefined[a]
double exponential	6
chi-squared	$12/r$[b]

[a]Numerical approximations give a value of the order of 6,000 (NIST 2006).

[b]where r is the degrees of freedom.

4.3.2 Distance from centre of the field

The next variable varied was the distance from the centre of the field of a given image. Earlier trials had shown that with the previously discussed range of 6495.5 Å and 6498.0 Å, it is only possible to observe out to a radius of 350 pixels from the centre of the field of view.

Initially six circular regions were investigated — stars within $R = 0$, $R < 50$, < 100, < 200, < 300, and $R < 350$. The last circular area equates to the 10-point plot shown in Figures 4.6, 4.7 & 4.8. For these and subsequent simulations 10 points were used in the wavelength range covering the BaII line unless otherwise stated.

The most obvious feature of the histograms in Figure 4.9 is the asymmetry (see also Table 4.4). This was totally unexpected and initially did not make any sense. There was no obvious feature of the spectrum or the fitting scheme that would cause any asymmetry in the resulting error plots. The velocity plots (Figure 4.10 and Table 4.5) are even more asymmetric, showing bumps.

The reason for the behaviour can be seen in Figure 4.11. The top plots show the inputted velocities, while the plots directly below show the fitted velocities for the same R range. The fitted histograms show very odd behaviour. First, the fact that they show a negative slope and not any symmetry around zero as would be expected. If all the inputted stars had resulted in perfect fits, then these plots would look like the plots above them. Instead, they show that most stars were fitted with a radial velocity of -12.5 km s^{-1}, the maximum allowed by the script. So the bumps in the error histograms of Figure 4.9 are the result of this negative slope and the normally distributed input values. Clearly this is quite probably a fundamental flaw in the script. It will be necessary to understand and correct the cause before it is used for reduction of real data.

The second odd feature of these fitted histograms is the lack of any fits for velocities of -12.93 km s^{-1} and 0.46 km s^{-1}. The reason for this is currently unknown. It appears in all the simulations.

The contour plots in Figure 4.12 show the bigger picture. At the inner radius, there is the long tail of the velocity errors. The top three plots all show the same basic shape. The bottom three show a similar shape as well, but slightly different, being more like the contour plots in Figure 4.8.

Looking at how the distance from the centre affects the quality of the fit shows that this fitting script is very dependent on the placement of the points. At certain positions, a lot of stars end up with bad fits due to the points not adequately providing coverage of the spectral line. This will require more careful investigation in future work.

Although the plots described above gave the first clues as to some odd behaviour related to the placement of the points, it is only possible to directly compare different plots in Figures 4.9 and 4.10. This is because the $R < 100$ plot also includes stars that

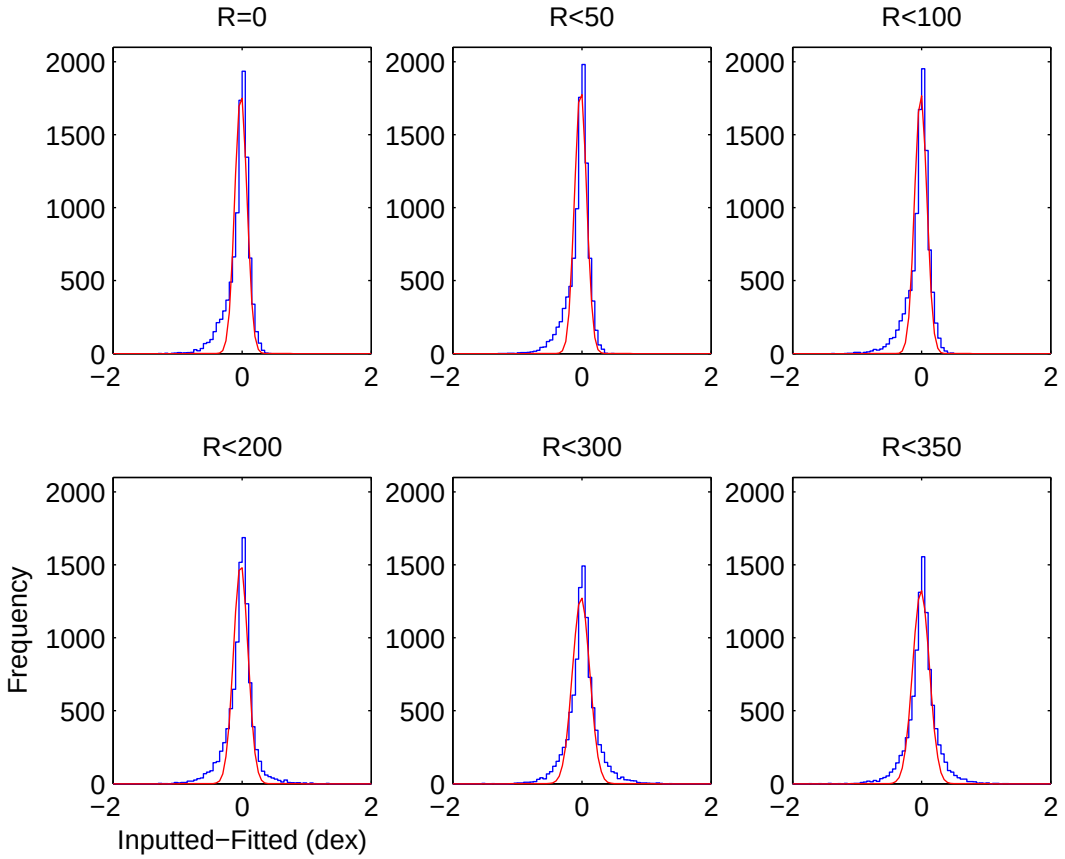

Figure 4.9: Error in abundance at different radii from the centre. The top-left plot shows the error for stars at the centre. The subsequent plots are at radii less than 50, 100, 200, 300 and 350 pixels respectively. At small radii there is an asymmetry of the profile. It is more likely for the stars to be found to be more abundant in barium than the inputted values. The parameters of the Gaussian distributions are given in Table 4.4.

Table 4.4: Gaussian parameters for Figure 4.9, the uncertainty distributions for abundance for different distances from the centre of the FOV (Section 4.3.2).

R range (pixels)	Peak value A	μ (dex)	σ (dex)	skewness	kurtosis
$R = 0$	1790	0.0	0.1	−1.5	6.5
$R < 50$	1820	0.0	0.1	−1.5	7.0
$R < 100$	1790	0.0	0.1	−1.5	7.2
$R < 200$	1510	0.0	0.1	−0.4	7.1
$R < 300$	1280	0.0	0.1	0.1	6.2
$R < 350$	1330	0.0	0.1	−0.2	6.8

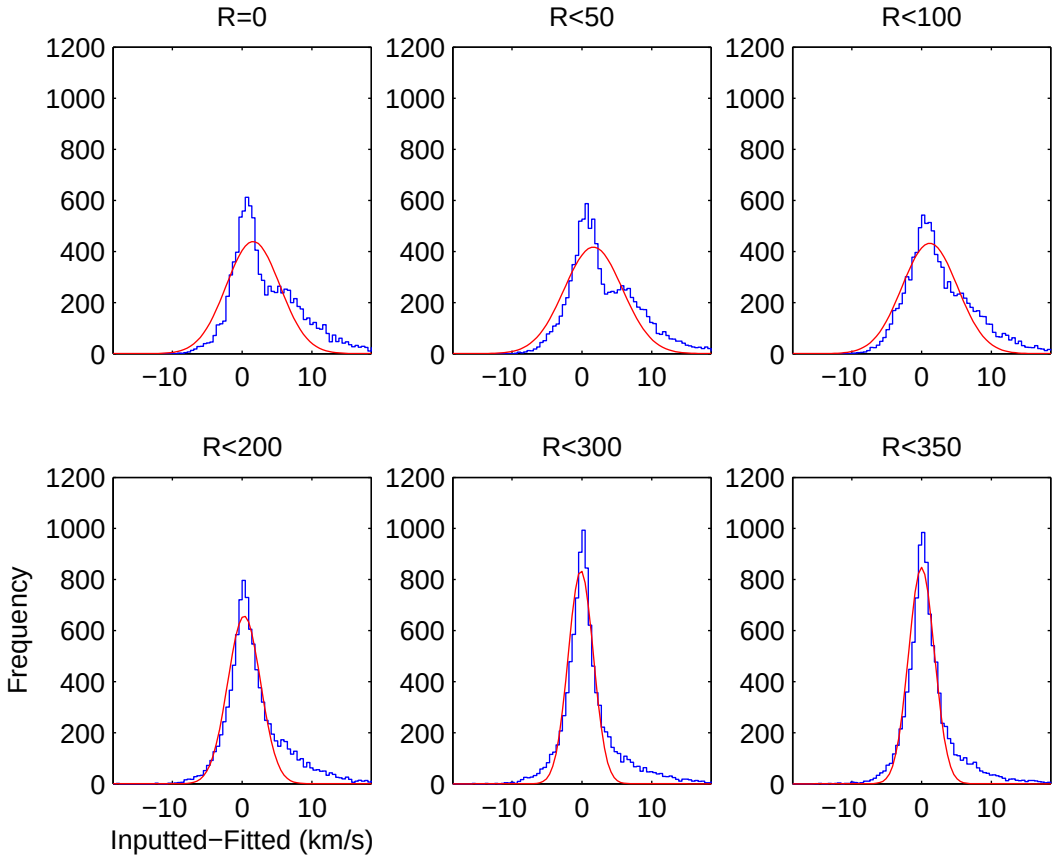

Figure 4.10: This figure shows how the error in velocity changes with radius from the centre of the field of view. This has the mirror distribution of that for the abundance, with a tendency to find a lower velocity than the inputte dvalue. This is especially evident at the smaller radii. The parameters of the Gaussian distributions are given in Table 4.5.

Table 4.5: Gaussian parameters for Figure 4.10, the uncertainty distributions for radial velocity for different distances from the centre of the FOV (Section 4.3.2).

R range (pixels)	Peak value A	μ (km s^{-1})	σ (km s^{-1})	skewness	kurtosis
$R = 0$	440	1.6	3.9	0.9	3.7
$R < 50$	420	1.6	4.2	0.8	3.8
$R < 100$	430	1.2	4.0	0.9	4.2
$R < 200$	660	0.3	2.4	1.3	5.8
$R < 300$	830	−0.3	1.8	1.4	6.8
$R < 350$	850	0.0	1.9	1.5	7.8

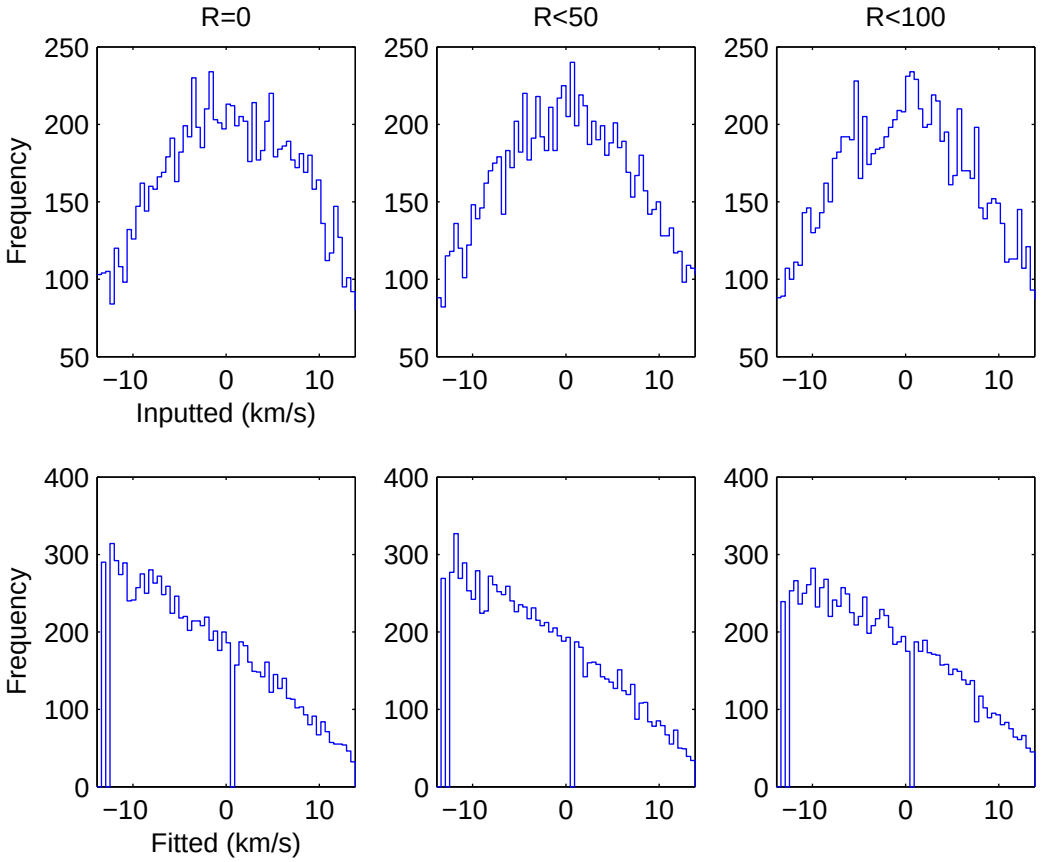

Figure 4.11: The top three histograms show the inputted values of velocity for the $R = 0$, $R < 50$ and < 100 simulations. They confirm that the inputted velocities are random numbers drawn from a normal distribution. The lower plots show the fitted values. Instead of showing a flat or normal distribution, it has a negative linear slope (see Section 4.3.2)

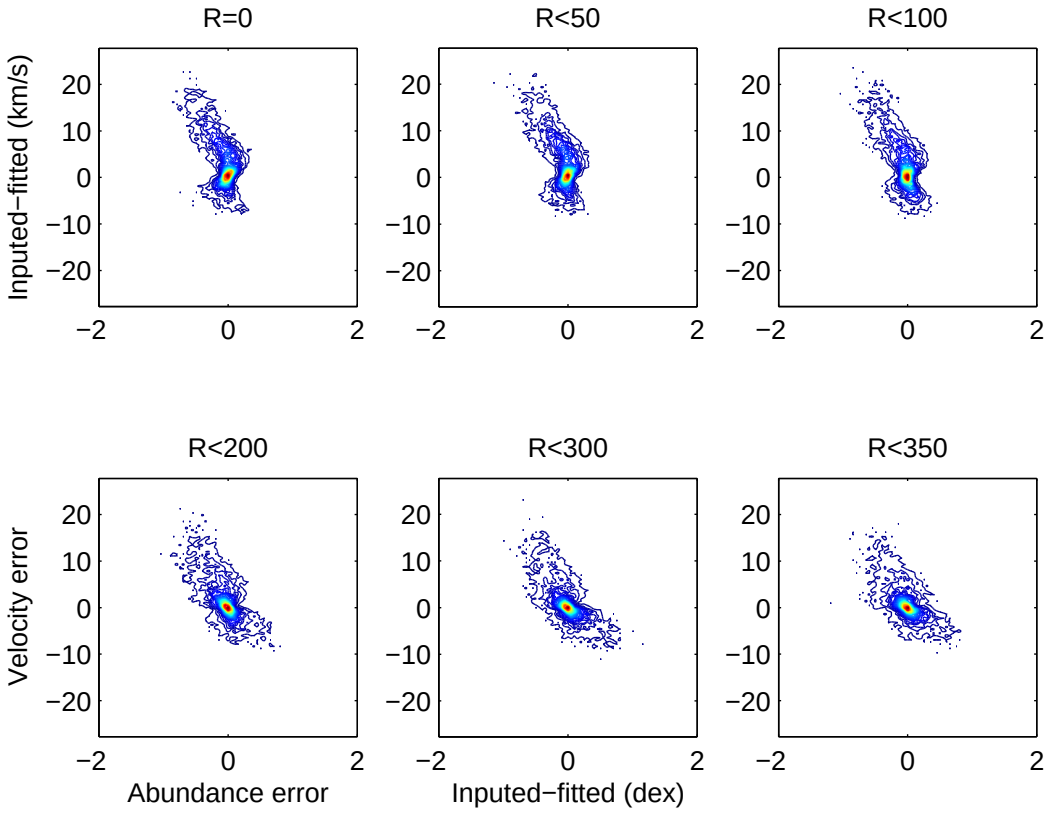

Figure 4.12: Combining the information from Figure 4.9 and 4.10 into a contour plot. At the smaller radii, there is a definite tail of abundance errors. Positive errors equate to the fitted spectrum having a smaller abundance than the true value. This tail appears to shrink in size at larger radii. The exact reason for this change with radius is unknown. The contours have a spacing of five units, starting at 2 and with a maximum of 8000.

are $R < 50$. It cannot be seen if the odd shapes of the profiles are caused by stars closer to the centre, at the edge or in the middle.

To investigate this further, equal-area annuli were calculated. Each annulus has the same area as a circle with a radius of 100 pixels, $\pi \times 10^4$ square pixels. Creating plots of this form allows for more quantitative comparisons to be made.

Overall there is no definite pattern through the annuli. No progressive improvement or deterioration in the quality of the fits.

First, looking at the radial velocities (Figure 4.13 and Table 4.6), the annuli closest to the centre are the worst in terms of high σ and low A. This is probably caused by the issue alluded to at the end of the previous section — that there seems to be a strong effect on the quality of the fits based upon the placement of the wavelength points. This distribution for the annulus closest to the centre also has positive skewness — fitted values are smaller than the inputted values. From the $200 < R < 223$ annulus onwards, the shift is towards a negative skew, until the $316 < R < 331$ annulus.

The opposite effect is seen in the abundance distribution's skewness (Figure 4.14 and Table 4.7). For the closest to the centre annulus, there is a negative skew, which changes to a positive skew and then back to a negative skew for the outermost annulus.

For all the distributions the kurtosis shows that all these distributions are all more peaked than a normal distribution. All this confirms that there is a strong link between placement of the points and the quality of the fits.

Figure 4.15 shows that moving to the outer annuli results in smaller and more circular contours. This is important for future planning in terms of the placement of the data sampling points. Although the shape of the contour rotates and shrinks, the short axis stays about the same size. This shows that excluding the outliers, there is a general uncertainty distributions that is common to all the annuli.

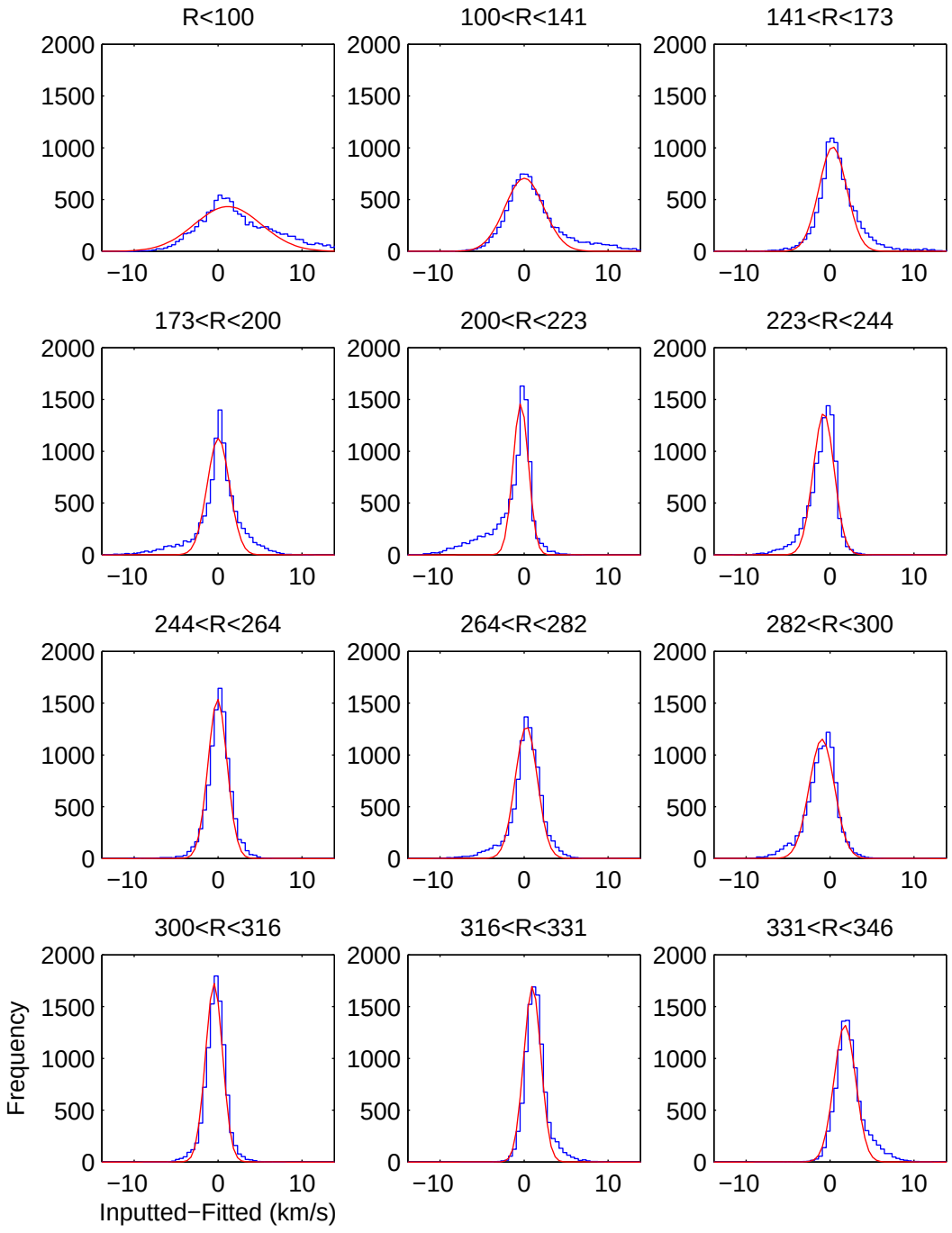

Figure 4.13: Velocity errors in equal area concentric rings. Overall the uncertainty distributions are generally Gaussian but with definite asymmetry. These extra bumps to the left and right of the central distribution are caused by the behaviour shown in Figure 4.11 — the code seems to be preferring the smallest radial velocity values allowed in the script. The reason for this unknown. The parameters of the Gaussian distributions are given in Table 4.6.

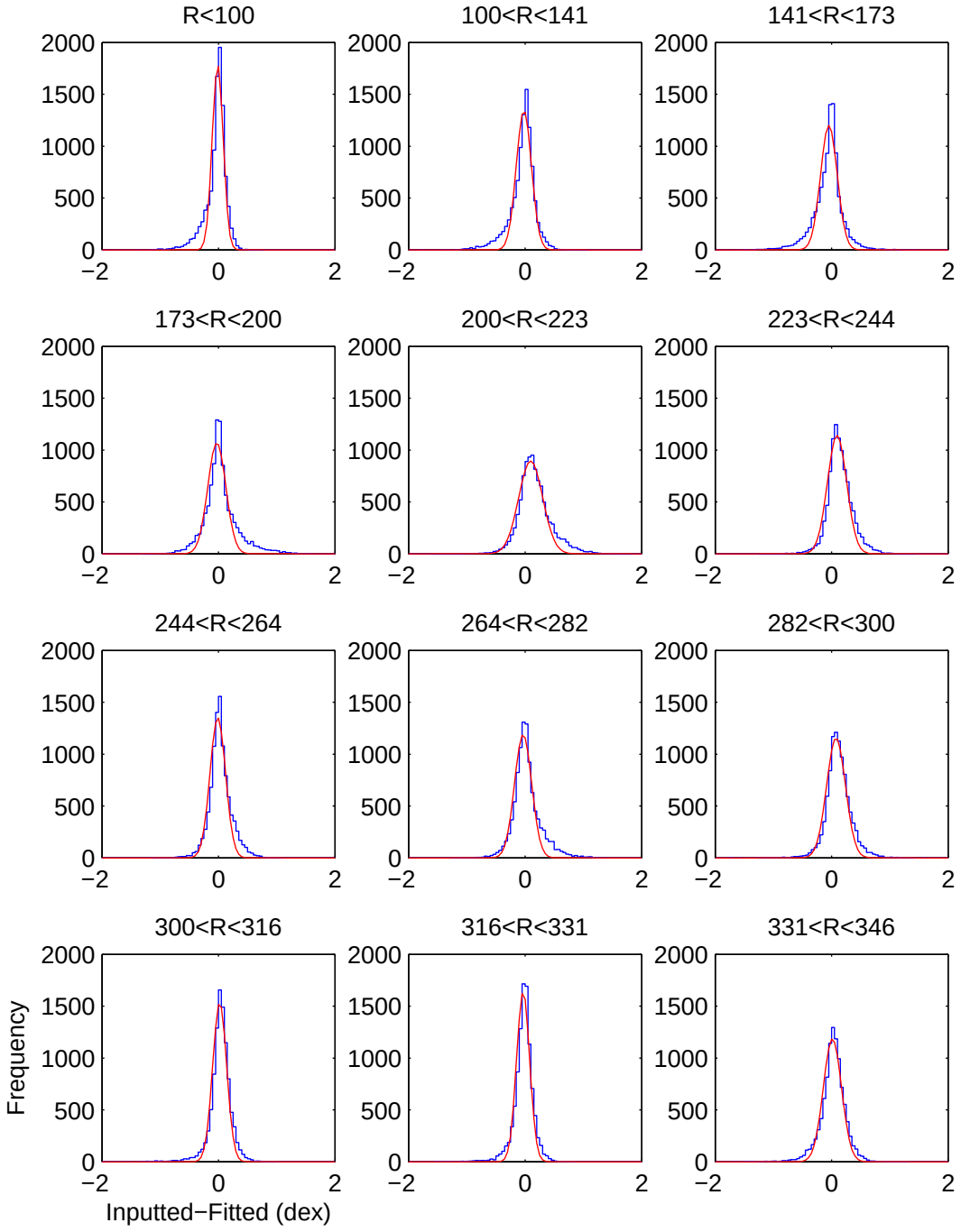

Figure 4.14: Abundance errors in equal area concentric rings. These do not show the bumps of Figure 4.13, but still do show some asymmetry, as can be seen in the parameters given in Table 4.7.

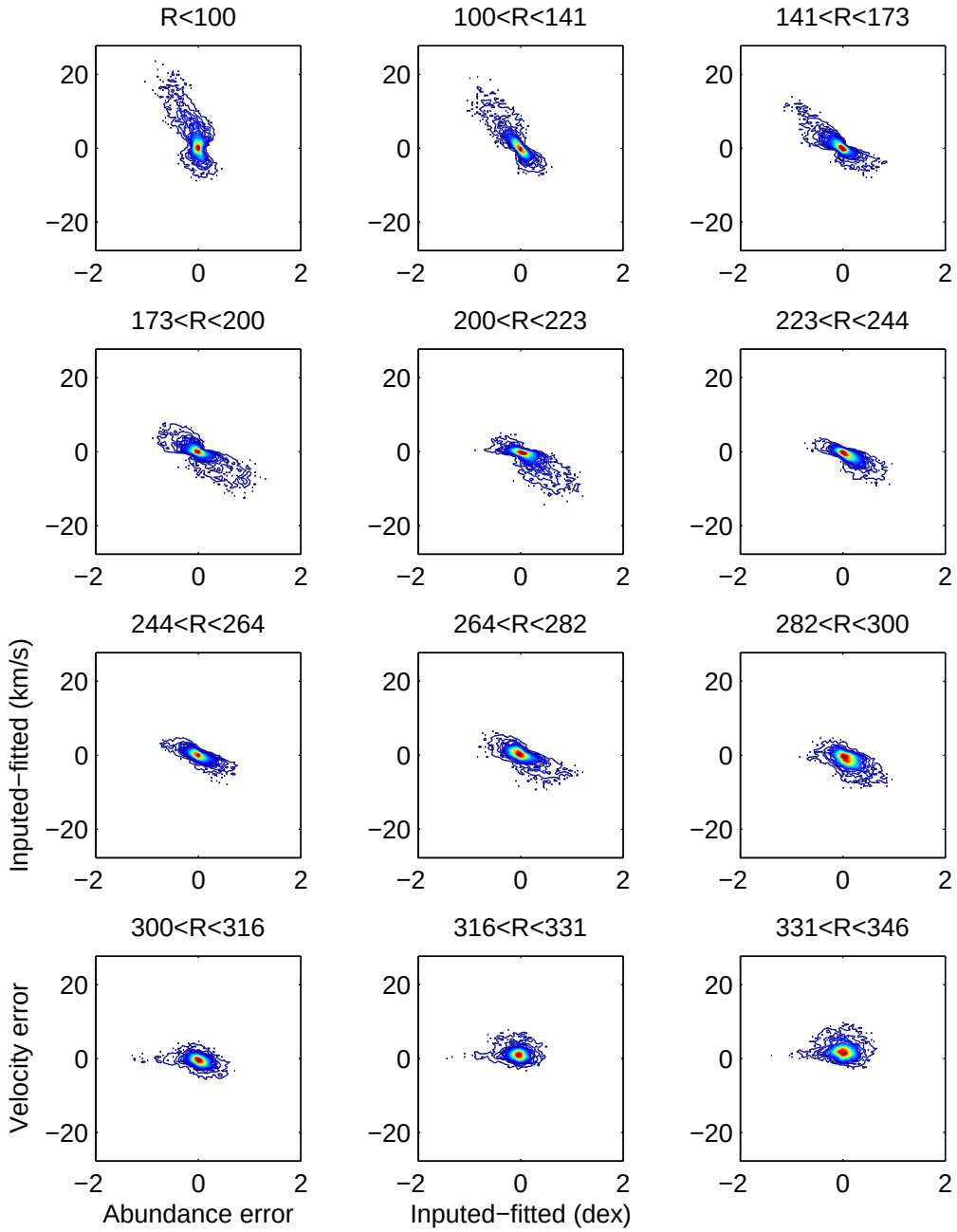

Figure 4.15: Contour plots combining the information in Figures 4.13 and 4.14. The contours have a spacing of five units, starting at 2 and with a maximum of 8000.

Table 4.6: Gaussian parameters for Figure 4.13, the uncertainty distributions for radial velocity for different equal-area annuli (Section 4.3.2).

R range (pixels)	Peak value A	μ ($\mathrm{km\,s^{-1}}$)	σ ($\mathrm{km\,s^{-1}}$)	skewness	kurtosis
$R < 100$	430	1.2	4.0	0.9	4.2
$100 < R < 141$	710	0.0	2.3	1.4	6.0
$141 < R < 173$	1010	0.3	1.7	1.2	8.0
$173 < R < 200$	1120	0.0	1.3	−0.8	5.7
$200 < R < 223$	1460	−0.4	0.9	−1.4	5.4
$223 < R < 244$	1370	−0.8	1.2	−1.2	5.8
$244 < R < 264$	1540	−0.1	1.1	−0.5	6.1
$264 < R < 282$	1280	0.3	1.3	−0.9	5.6
$282 < R < 300$	1150	−1.0	1.5	−0.7	4.3
$300 < R < 316$	1720	−0.5	1.0	−0.2	4.7
$316 < R < 331$	1700	1.0	1.0	1.0	5.8
$331 < R < 346$	1320	1.8	1.3	0.1	4.8

Table 4.7: Gaussian parameters for Figure 4.14, the uncertainty distributions for abundance for different equal-area annuli (Section 4.3.2).

R range (pixels)	Peak value A	μ (dex)	σ (dex)	skewness	kurtosis
$R < 100$	1790	0.0	0.1	−1.5	7.2
$100 < R < 141$	1340	0.0	0.1	−1.2	6.3
$141 < R < 173$	1200	−0.1	0.1	−0.6	6.4
$173 < R < 200$	1070	0.0	0.2	0.8	5.5
$200 < R < 223$	890	0.1	0.2	0.6	4.6
$223 < R < 244$	1140	0.1	0.2	0.3	4.6
$244 < R < 264$	1350	0.0	0.1	0.2	4.8
$264 < R < 282$	1190	0.0	0.2	0.8	5.6
$282 < R < 300$	1150	0.1	0.2	−0.1	7.3
$300 < R < 316$	1540	0.0	0.1	−1.8	15
$316 < R < 331$	1640	0.0	0.1	−1.5	11
$331 < R < 346$	1190	0.0	0.2	−0.9	7.4

4.3.3 Signal-to-noise ratio

The last variable that was varied was the signal-to-noise (S/N) ratio. This was varied from 10 up to 1,000. It was at S/N= 10 that a peculiar phenomenon was discovered in the fitting algorithm. In the top-left histogram of Figure 4.16 (whose parameters are given in Table 4.8) there are practically no stars with fitted values less than the inputted values. The reason for this can be seen in Figure **??**. At this low signal-to-noise the fitting has defaulted to a value of +1 dex, or −1 dex for a smaller number of them.

The reason for this is not fully understood. It is probably caused by the extremely large error bars that the data has at a S/N ratio of 10. Since the least-squares fitting is weighted by the uncertainty of each point, the S/N could mean that the best fit is for an abundance of +1 dex, or −1 dex, even though this is clearly not the best fit that would come from hand fitting.

Both the abundance (Figure 4.16 and Table 4.8) and radial velocity (Figure 4.17 and Table 4.9) uncertainty distributions show the obvious behaviour that increasing the signal-to-noise decreases σ and causes μ to converge to zero.

In the case of the very high S/N ratio distributions, they are definitely non-Gaussian distributions. For the S/N= 1000 distribution, the kurtosis is 9.0 for the abundance and 9.7 for the radial velocity uncertainties. This is similar to the values for an exponential distribution which is nine (Table 4.3 and Weisstein 2009). It appears to be a Lorentzian distribution, for which the kurtosis can be numerically calculated to be about $\sim$ 6,700 (NIST 2006). This high value is caused by the extended tails. The uncertainty distributions shown in this thesis could actually be Lorentzian but due to the finite number of data points, do not show the extended tails needed for the extremely large kurtosis values.

The contour plots in Figure 4.18 show that overall there is a consistent shape of the badly fitted data for S/N> 100. As the ratio is increased there is still a general distribution of outliers but most of the stars are fitted correctly. By varying the S/N ratio it has been shown that better signal-to-noise will result in more precise data with less uncertainty in the abundance determination.

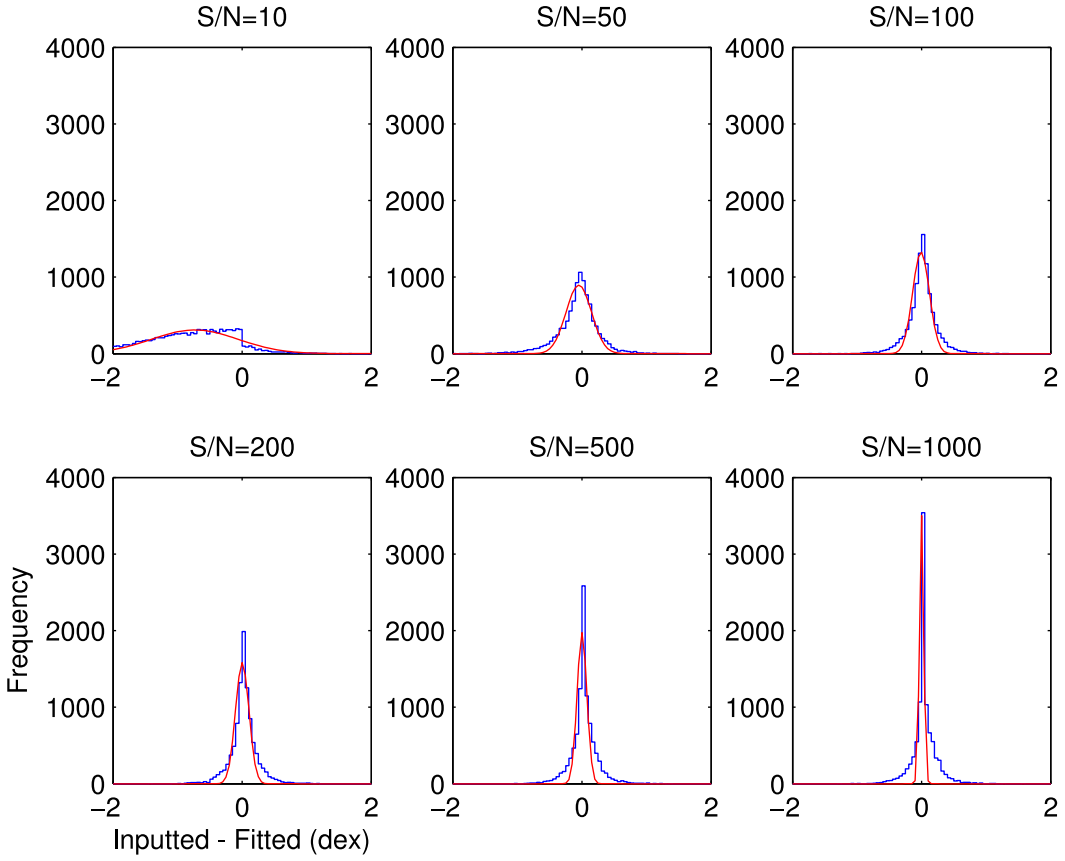

Figure 4.16: Error in abundance with changing signal-to-noise. At very low signal to noise, the abundance determination does not even conform to a symmetrical distribution. The Gaussian parameters are given in Table 4.8.

Table 4.8: Gaussian parameters for Figure 4.16, the uncertainty distributions for abundance for changing signal-to-noise ratios (Section 4.3.3).

S/N ratio	Peak value A	μ (dex)	σ (dex)	skewness	kurtosis
10	310	−0.7	0.7	0.0	2.6
50	890	−0.10	0.2	−0.6	6.0
100	1330	0.0	0.1	−0.2	6.8
200	1580	0.0	0.1	0.1	7.1
500	1970	0.0	0.1	0.3	7.9
1000	3500	0.0	0.0	0.1	9.0

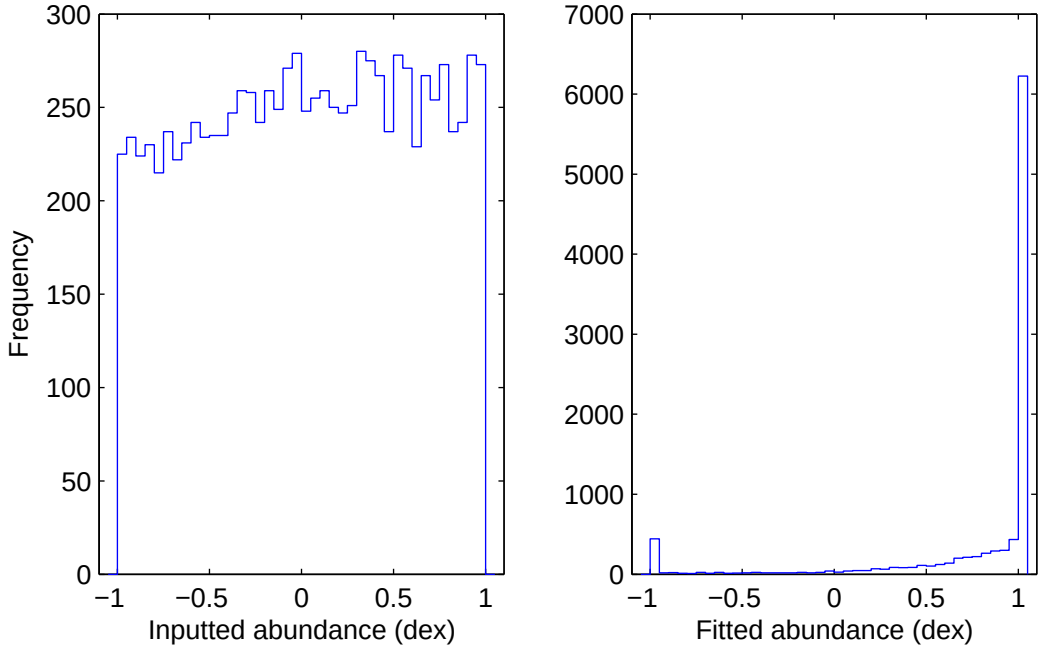

Table 4.9: Gaussian parameters for Figure 4.17, the uncertainty distributions for radial velocity for changing signal-to-noise ratios (Section 4.3.3).

S/N ratio	Peak value A	μ ($\mathrm{km\,s^{-1}}$)	σ ($\mathrm{km\,s^{-1}}$)	skewness	kurtosis
10	430	−1.2	4.0	0.2	5.3
50	580	−0.1	2.8	1.0	6.4
100	850	0.0	1.9	1.5	7.8
200	960	0.0	1.6	1.6	7.9
500	1100	0.0	1.3	1.7	8.6
1000	2710	0.0	0.3	1.9	9.7

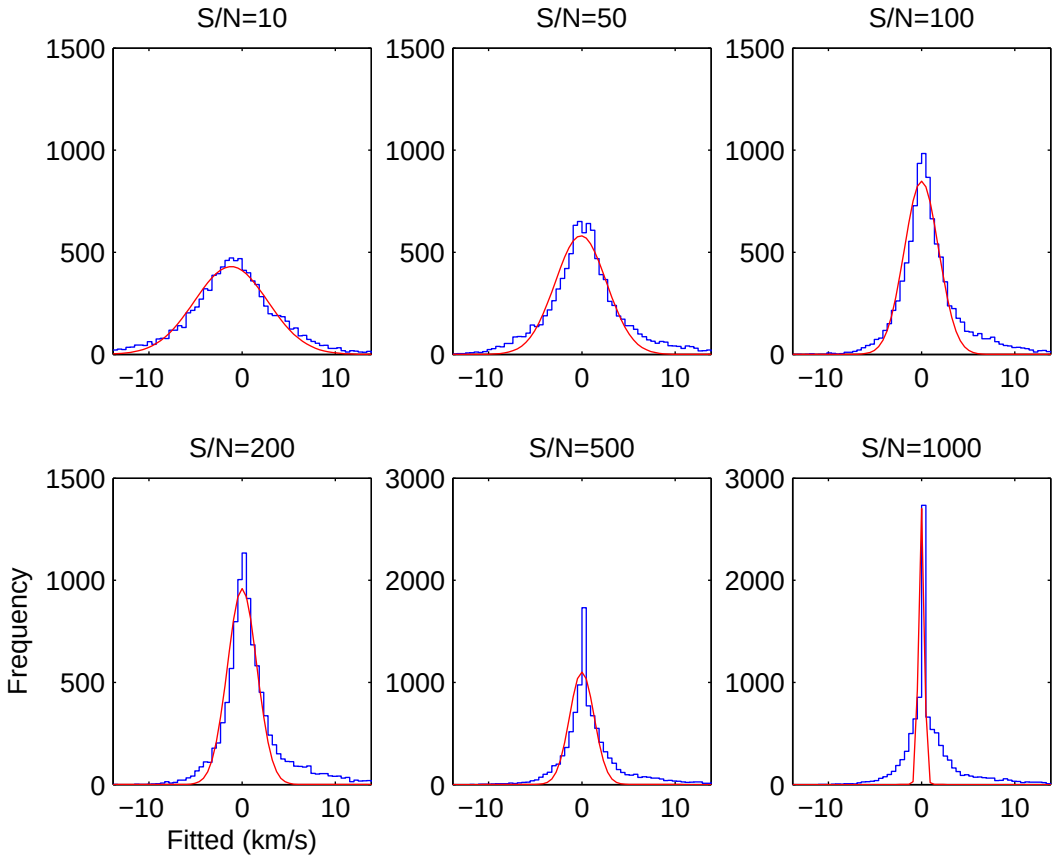

Figure 4.17: As for Figure 4.13, but for radial velocity. These distributions are symmetrical even at the lowest S/N, although at the higher S/N there does seem to be some asymmetry. This could just be a small-number statistics issue, with those error ranges only having frequencies a few percent of the central peak. The Gaussian parameters are given in Table 4.9.

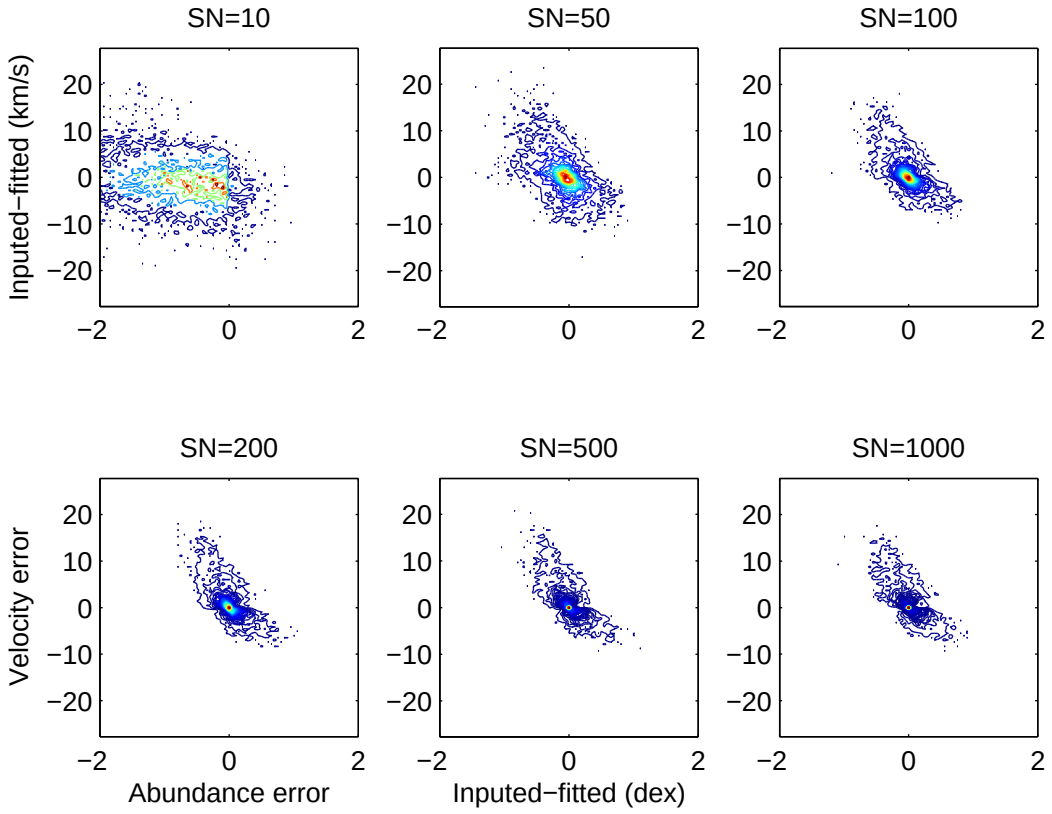

Figure 4.18: Combining the information from Figure 4.16 and 4.17 into a contour plot. These show the obvious result that at the highest S/N there is little error in either the abundance or the velocity. From this it would appear that a S/N=50 will be inadequate for determining abundances or velocities to any sort of precision. Even a S/N of 100 seems to have a large spread of values. The contours have a spacing of five units, starting at 2 and with a maximum of 8000.

4.4 Discussion

Overall the analysis of the simulations have shown that the spectrum fitting script does retrieve the inputted values for most stars. The fitted Gaussian distributions have μ values close to zero and a σ values of less than 0.1 dex for the abundance errors. They have shown that with higher signal-to-noise ratios, σ values of 0.05 dex could be achievable. Such values are critical for the future aims of this research — large-scale elemental abundance determination of stars in globular clusters.

In determining the abundance, the radial velocity of the star must also be found. These values will prove useful for dynamical studies. These were shown to have uncertainties of the order of ± 3 km s^{-1}. This is an order of magnitude higher than the errors in high-resolution échelle spectrographs, but will still provide useful survey information of clusters. The placement of the sampling points was not critical for precise radial velocity determination.

What other insights have the simulations given? As shown in Section 4.3.1, once there are seven points in the wavelength range of the BaII spectral line, there are no significant improvements in the precision of the fits. This is important to know in terms of planning observations. Of course increasing the number of data points does slightly decrease the σ values as can be seen in Table 4.2, but there would be a significant increase in the observing time for example.

However there are obvious problems with the fitting script. These can be clearly seen in for example Figure 4.6. What in the script is causing there to be a bump of erroneous stars to the right of the distribution? It is these sorts of errors that need to be investigated further. Is there a way to stop the script defaulting to abundance values of -1 or $+1$ dex for low signal-to-noise ratios?

The placement in wavelength space of the data points is also critical. This will have to be carefully considered as there are two effects that will shift the wavelength of the observed points — the radial velocity of the star and its distance from the centre of the field of view. The former is completely uncontrollable, although its range is known from the velocity dispersion of 47 Tuc or other targets. The latter is well within the control of the observer.

It will require future work to understand fully how the placement of the points is affecting the determination of the radial velocity and the abundance. It could be shown that having points centred on the line for a star at the centre of the field is not the most optimal positioning. It could be more useful to have the points centred for a star at 200 pixels, for instance.

Another possibility is to observe a second, much stronger spectral line for each star. For instance, observing the CaII line from Chapter 3 would allow the radial velocity to be

determined more accurately, making the determination of the barium abundance to a one parameter problem, instead of the current two. A single, strong line has the advantage of only requiring curve fitting. The downside of this is obvious — double the observations will be required.

Chapter 5

Conclusion

This thesis investigated the use of a Fabry-Pérot interferometer (FPI) for stellar elemental abundance determination, with particular focus on s-process elements in stars of the globular cluster 47 Tuc. It has shown that it should be possible to determine the abundance of stars in this cluster with a $\sigma = 0.1$ dex. This is of the order of the variations found by previous researchers for s-process elements in 47 Tuc (Table 1.1).

The FPI is a tunable narrow-bandwidth filter. It can be used to sample a spectral line in each star in the field of view simultaneously. This will allow hundreds and perhaps thousands of stellar spectra to be obtained without the overhead involved in other multi-object spectroscopy techniques. The particular FPI it is planned to use for observations is a mode on the Robert Stobie Spectrograph (RSS) of the Southern African Large Telescope (SALT). Using this 10-metre class telescope it will be possible to observe asymptotic giant branch (AGB) stars with the possibility of observing the fainter main sequence stars. By using the FPI mode of RSS it will be possible to observe the 6496.9 Å line of BaII with a spectral resolution of about 8,000.

Since the RSS was unavailable during the period of this thesis, observations of other groups of stars and spectral simulations were utilized instead.

The data was in the form of spectrum segments and images provided by Rangwala (2008). This proved invaluable for this thesis, in terms of understanding the spectrum fitting processes that will be required for real data. One of the most important lessons from this was that the correct fitting of the continuum is critical for precise equivalent width determination.

Since the CaII line is not typical of the spectral line that will be observed in 47 Tuc, it was necessary to look at synthetic spectra. The script developed for fitting Voigt profiles to the CaII data was modified to fit a synthetic spectrum to simulated FPI data. These simulated data were created using MOOG. It was adjusted with random abundance, continuum and radial velocity values. The MATLAB script developed in this thesis then attempted to retrieve the inputted values using its fitting process. This was found to be mostly successful with some idiosyncratic behaviour that needs to be investigated further.

The simulations showed that it should be possible to recover abundance information

with an uncertainty of about 0.1 dex if 10 points are observed with a S/N of about 100. But with SALT it will be possible to achieve a signal-to-noise ratio of about 500 with a reasonable exposure. This will decrease the uncertainty significantly. This should result in future research in this area being able to conduct large scale surveys of globular cluster stars for elemental abundance determination.

5.1 Future work

With the groundwork laid for understanding the data reduction and fitting for FPI data, the next step in this research will be obtaining images of 47 Tuc with SALT. Based on the simulations of Chapter 4, this would consist of obtaining at least 16 data points covering the BaII spectral line. The exact placement of these points will have to be determined after future investigation of the spectrum fitting script.

Chapter 4 showed that at least 10 points across the line will be sufficient for $\sigma < 0.1$ dex fitting. It is necessary to obtain observations with this uncertainty or smaller in order to prove whether the s-process element enhancements are real.

Moving on from 47 Tuc this method of abundance determination is equally applicable to other globular clusters. It is also useful for dynamical research since the radial velocity of the individual stars is determined as part of the fitting process.

This abundance determination technique could be applied to other types of objects such as open clusters. With much smaller numbers of stars (less than 1,000) in the cluster it would be possible to observe all the members at the same time. And with the dynamical information, a complete picture of the cluster could be developed from one set of observations. Current research in the literature has samples of less than 10 stars.

Once observations have been made of the BaII line and their reduction to elemental abundances understood fully, it would be useful to investigate other lines. It may be found that weaker lines could be used for abundance extraction, which means weaker or more blended lines of other elements could be used.

Bibliography

Alves-Brito A, Barbuy B, Ortolani S, Momany Y, Hill V, Zoccali M, Renzini A, Minniti D, Pasquini L, Bica E & Rich R M 2005. *VLT-UVES analysis of 5 giants in 47 Tucanae.* A&A **435**, 657–667.

Born M & Wolf E 1964 *Principles in Optics* Pergamon Press.

Brown J A & Wallerstein G 1992. *High-resolution CCD spectra of stars in globular clusters. VII - Abundances of 16 elements in 47 Tuc, M4, and M22.* AJ **104**, 1818–1830.

Buisson H, Fabry C & Bourget H 1914. *An application of interference to the the study of the Orion nebula.* ApJ **40**, 241–258.

Burbidge E M, Burbidge G R, Fowler W A & Hoyle F 1957. *Synthesis of the Elements in Stars.* Reviews of Modern Physics **29**, 547–650.

Carretta E, Gratton R, Bragaglia A, Bonifacio P & Pasquini L 2004. *Abundance Analysis of Turn-Off and Early Subgiant Stars in the Globular Cluster 47 Tuc (NGC 104).* A&A **416**, 925.

Cohen J G, Briley M M & Stetson P B 2005. *C and N Abundances in Stars at the Base of the Red Giant Branch in M15.* AJ **130**, 1177–1193.

de Vaucouleurs G 1981. *Surveying velocity fields in galaxies.* Sky and Telescope **62**, 406–410.

Delbouille L, Roland G & Neven L 1973 *Atlas photométrique DU spectre solaire de λ 3000 a λ 10000* Liege: Universite de Liege, Institut d'Astrophysique, 1973.

Fabry C & Pérot A 1901. *On a New Form of Interferometer.* ApJ **13**, 265–+.

Fabry C & Pérot A 1902. *Measures of Absolute Wave-Lengths in the Solar Spectrum and in the Spectrum of Iron.* ApJ **15**, 73–+.

Freeman K C & Rodgers A W 1975. *The Chemical Inhomogeneity of Omega Centauri.* ApJL **201**, L71+.

Gilliland R L, Bono G, Edmonds P D, Caputo F, Cassisi S, Petro L D, Saha A & Shara M M 1998. *Oscillating Blue Stragglers in the Core of 47 Tucanae.* ApJ **507**, 818–845.

Gratton R G 1999. *Early nucleosynthesis and chemical abundances of stars in globular clusters.* in '10th Canary Islands Winter School of Astrophysics: Globular clusters' pp. 155–206.

Gratton R G, Bragaglia A, Carretta E, Clementini G, Desidera S, Grundahl F & Lucatello S 2003. *Distances and ages of NGC 6397, NGC 6752 and 47 Tuc.* A&A **408**, 529–543.

Gratton R, Sneden C & Carretta E 2004. *Abundance Variations Within Globular Clusters.* ARA&A **42**, 385–440.

Harris D L 1948. *On the Line-Absorption Coefficient due to Doppler Effect and Damping.* ApJ **108**, 112–115.

Hartung M, Lidman C, Ageorges N, Marco O, Kasper M E & Clenet Y 2004. *Commissioning of the NACO Fabry-Perot interferometer at the VLT.* in A. F. M Moorwood & M Iye, eds, 'Society of Photo-Optical Instrumentation Engineers (SPIE) Conference Series' Vol. 5492 of *Society of Photo-Optical Instrumentation Engineers (SPIE) Conference Series* pp. 1531–1541.

Hernandez G 1986 *Fabry-Perot interferometers* Cambridge Studies in Modern Optics, Cambridge: University Press, 1986.

Hesser J E, Harris W E, Vandenberg D A, Allwright J W B, Shott P & Stetson P B 1987. *A CCD color-magnitude study of 47 Tucanae.* PASP **99**, 739–808.

Hinkle K, Wallace L, Valenti J & Harmer D 2000 *Visible and Near Infrared Atlas of the Arcturus Spectrum 3727-9300 A* San Francisco: ASP.

Hook I M, Jørgensen I, Allington-Smith J R, Davies R L, Metcalfe N, Murowinski R G & Crampton D 2004. *The Gemini-North Multi-Object Spectrograph: Performance in Imaging, Long-Slit, and Multi-Object Spectroscopic Modes.* PASP **116**, 425–440.

Iben I 1985. *The life and times of an intermediate mass star - In isolation/in a close binary.* QJRAS **26**, 1–39.

James G, François P, Bonifacio P, Carretta E, Gratton R G & Spite F 2004. *Heavy elements and chemical enrichment in globular clusters.* A&A **427**, 825–838.

Kashikawa N, Aoki K, Asai R, Ebizuka N, Inata M, Iye M, Kawabata K S, Kosugi G, Ohyama Y, Okita K, Ozawa T, Saito Y, Sasaki T, Sekiguchi K, Shimizu Y, Taguchi H, Takata T, Yadoumaru Y & Yoshida M 2002. *FOCAS: The Faint Object Camera and Spectrograph for the Subaru Telescope.* PASJ **54**, 819–832.

Kurucz R 1993. *SYNTHE Spectrum Synthesis Programs and Line Data.* Kurucz CD-ROM No. 18. Cambridge, Mass.: Smithsonian Astrophysical Observatory, 1993. **18**.

Lamla E, Beyer M, Waldmeier M, Petri W, Hoffmeister C, Thomas H, Kippenhahn R, Scheffler H, van den Bergh S & Böhm-Vitense E 1965 *Astronomy and Astrophysics* Vol. 1 of *Landolt-Börnstein - Group VI Astronomy and Astrophysics* Springer-Verlag.

Lenzen R, Hartung M, Brandner W, Finger G, Hubin N N, Lacombe F, Lagrange A M, Lehnert M D, Moorwood A F M & Mouillet D 2003. *NAOS-CONICA first on sky results in a variety of observing modes.* Vol. 4841 SPIE pp. 944–952.
URL: `http://link.aip.org/link/?PSI/4841/944/1`

Merrill P 1952. *Technetium in the stars.* Science **115**, 484.

Meylan G & Mayor M 1986. *Studies of dynamical properties of globular clusters. II - The rotation, velocity dispersion and mass of Omega Centauri and 47 Tucanae.* A&A **166**, 122–142.

Moore C 1972 *A Multiplet Table of Astrophysical Interest* National Bureau of Standards.

NIST 2006 'NIST/SEMATECH e-handbook of statistical methods' HTML.
URL: `http://www.itl.nist.gov/div898/handbook`

O'Dell C R 2001. *Structure of the Orion Nebula.* PASP **113**, 29–40.

Padmanabhan T 2001 *Theoretical Astrophysics, Volume 2: Stars and Stellar Systems* Cambridge University Press.

Ramsey B P & Cleveland E L 1941. *Criteria and the intensity-epoch slope.* Journal of the Optical Society of America (1917-1983) **31**, 26–+.

Rangwala N 2008 private communication.

Rangwala N, Williams T B, Pietraszewski C & Joseph C L 2008. *An Imaging FABRY-PÉROT System for the Robert Stobie Spectrograph on the Southern African Large Telescope.* AJ **135**, 1825–1836.

Rangwala N, Williams T B & Stanek K Z 2009. *Fabry-Perot Absorption Line Spectroscopy of the Galactic Bar. I. Kinematics.* ApJ **691**, 1387–1399.

Rich R M, Reitzel D B, Howard C D & Zhao H 2007. *The Bulge Radial Velocity Assay: Techniques and a Rotation Curve.* ApJL **658**, L29–L32.

Sharp R, Saunders W, Smith G, Churilov V, Correll D, Dawson J, Farrel T, Frost G, Haynes R, Heald R, Lankshear A, Mayfield D, Waller L & Whittard D 2006. *Performance of AAOmega: the AAT multi-purpose fiber-fed spectrograph.* in 'Society of Photo-Optical Instrumentation Engineers (SPIE) Conference Series' Vol. 6269 of *Society of Photo-Optical Instrumentation Engineers (SPIE) Conference Series.*

Sneden C 1999. *Abundances in Globular Clusters.* Ap&SS **265**, 145–152.

Sneden C A 1973 Carbon and Nitrogen Abundances in Metal-Poor Stars. PhD thesis The University of Texas at Austin.

Stetson P B 1987. *DAOPHOT - A computer program for crowded-field stellar photometry.* PASP **99**, 191–222.

Sugai H, Kawai A, Hattori T, Ozaki S, Kosugi G, Shimono A & Okita Y 2006. *The Kyoto tridimensional spectrograph II.* New Astronomy Review **50**, 358–361.

Suntzeff N B & Kraft R P 1996. *The Abundance Spread Among Giants and Subgiants in the Globular Cluster Omega Centauri.* AJ **111**, 1913–+.

Vaughan J M 1989 *The Fabry-Perot interferometer. History, theory, practice and applications* The Adam Hilger Series on Optics and Optoelectronics, Bristol: Hilger, 1989.

Weisstein E W 2009 'Kurtosis' HTML.
URL: `http://mathworld.wolfram.com/Kurtosis.html`

Wylie E C, Cottrell P L, Sneden C A & Lattanzio J C 2006. *Heavy-Element Abundances in Giant Stars in 47 Tucanae.* ApJ **649**, 248–257.

Appendix A

MATLAB code written for this thesis

A.1 Code for producing Voigt profile

In order to numerically calculate the Voigt profile, code from MOOG (Sneden 1973) was used. This code uses the algorithm from Lamla et al. (1965).

The two variables past to the function are v, the independent variable, and a, the "voigt parameter", which gives the shape of the profile.

```
function voigt=voigtf(v,a)

voigt=0;

if a==0
    voigt = exp(-v^2)/sqrt(pi);
    return
elseif a<=0.2
    if v>=5
        voigt = a/(sqrt(pi)*v^2)*(1 + 1.5/v^2 + 3.75/(v^4));
        voigt = voigt/sqrt(pi);
        return
    elseif v<5
        h0 = exp(-v^2);
        if v>=2.4
            h1=(0.554153432+0.278711796*v-0.188325687*v^2+0.042991293*v^3-0.003278278*v^2)/(v^2-1.5);
        elseif v>=1.3 & v<2.4
            h1=-4.48480194+9.39456063*v-6.61487486*v^2+1.98919585*v^3-0.2204165*v^4;
        else
            h1=-1.12470432-0.15516677*v+3.28867591*v^2-2.34357915*v^3+0.42139162*v^4;
        end
        h2 = (1.0 - 2.0*v^2)*h0;
        if a <= 0.2
            voigt = h0 + h1*a + h2*a^2;
            voigt = voigt/sqrt(pi);
            return
        end
        h1 = h1 + 1.1283790*h0;
        h2p = h2;
        h2 = h2 - h0 + 1.1283790*h1;
        h3 = 0.37612635*(1.0-h2p) - (2/3)*v^2*h1 + 1.1283790*h2;
        h4 = (2/3)*v^2*v^2*h0 - 0.37612635*h1 + 1.1283790*h3;
        voigt = u*(h0 + h1*a + h2*a^2 + h3*a^3 + h4*a^4);
        voigt = voigt/sqrt(pi);
        return
    end
elseif (a<=1.4 & a+v<=3.2)
    u=0.979895023-0.962846325*a+0.532770573*a^2-0.122727278*a^3;
    h0 = exp(-v^2);
    if v>=2.4
        h1=(0.554153432+0.278711796*v-0.188325687*v^2+0.042991293*v^3-0.003278278*v^2)/(v^2-1.5);
    elseif v>=1.3 & v<2.4
        h1=-4.48480194+9.39456063*v-6.61487486*v^2+1.98919585*v^3-0.2204165*v^4;
    else
        h1=-1.12470432-0.15516677*v+3.28867591*v^2-2.34357915*v^3+0.42139162*v^4;
    end
    h2 = (1.0 - 2.0*v^2)*h0;
```

```
    if a < 0.2
        voigt = h0 + h1*a + h2*a2;
        voigt = voigt/sqrt(pi);
        return
    end
    h1 = h1 + 1.1283790*h0;
    h2p = h2;
    h2 = h2 - h0 + 1.1283790*h1;
    h3 = 0.37612635*(1.0-h2p) - (2/3)*v^2*h1 + 1.1283790*h2;
    h4 = 2/3*v^2*v^2*h0 - 0.37612635*h1 + 1.1283790*h3;
    voigt = u*(h0 + h1*a + h2*a^2 + h3*a^3 + h4*a^4);
    voigt = voigt/sqrt(pi);
    return
else
    u = sqrt(2)*(a^2 + v^2);
    voigt = sqrt(2/pi)*a/u*(1.0 + (3.0*v^2-a^2)/u^2+(15.0*v^4-30.0*a^2*v^2+3.0*a^4)/u^4);
    voigt = voigt/sqrt(pi);
end
```

A.2 Code for finding common stars in multiple images

This is the MATLAB function that finds common stars in multiple images. It takes as input arrays of x and y coordinates, and the variable `closeness` which defines in the same units as the coordinates how close the stars have to be to each other between images.

```
function [runIntersect holder_x holder_y]=closeintersect(varargin)

flag = 0;
if isempty(varargin),
    error('No inputs specified.')
else
    setArray = varargin(1:end-1);
    closeness= varargin{end};
end

runIntersect = setArray{1};

i=2;

for i = 2:length(setArray)
    k=1;
    saved_mags=[];
    holder_x=[];
    holder_y=[];
    for j=1:length(runIntersect(:,1))
        I=find(runIntersect(j,1)-closeness<setArray{i}(:,1)
          & runIntersect(j,1)+closeness>setArray{i}(:,1)
          & runIntersect(j,2)-closeness<setArray{i}(:,2)
          & runIntersect(j,2)+closeness>setArray{i}(:,2),1);
        if length(I)~=0 & i~=2
            saved_mags(k,:)=[runIntersect(j,:) I];
            k=k+1;
        elseif length(I)~=0
            saved_mags(k,:)=[runIntersect(j,:) j I];
            k=k+1;
        end
    end
    runIntersect=saved_mags;
    for m=1:i
        holder_x(:,m)=setArray{m}(saved_mags(:,m+2),1);
        holder_y(:,m)=setArray{m}(saved_mags(:,m+2),2);
    end
    runIntersect(:,1)=mean(holder_x,2);
    runIntersect(:,2)=mean(holder_y,2);
end
```

A.3 Multiple fitting of line profiles script

```
clear all
```

```
clc
rand('state', sum(100*clock));
randn('state', sum(100*clock));
load('spec4500_45.mat')
spectrum4500(:,2:42)=1-spectrum4500(:,2:42);
waves=spectrum4500(:,1);
wavelengths=[6487.2 6487.5 6487.8 [6495.50:(2.5)/9:6498.00] 6502.8 6503.0 6503.3];

signaltonoise=100;

i=1;
tic
stars=1;
velshift=0.1;
p_old(2:3)=0;
abund=0.1;
while stars~=10000

    [data velshift abund R continuum_initial]=fpidata(wavelengths,signaltonoise);

    Ind=round((data(:,1)-6482.21)/0.01 +1);
    %
    %     %This is now our data. Has a velocity shift added to the wavelengths. A
    %     %random abundance value is picked, some noise added. And an uncertainty
    %     %with some random size related to the signal to noise
    %
    mean_left=sum(data(1:3,2)./data(1:3,3).^2)/sum(1./data(1:3,3).^2);
    mean_right=sum(data(length(wavelengths)-2:length(wavelengths),2)
               ./data(length(wavelengths)-2:length(wavelengths),3).^2)
               /sum(1./data(length(wavelengths)-2:length(wavelengths),3).^2);
    if abs(mean_left-mean_right)/mean_left>0.01
        continuum=max([mean_left mean_right]);
    else
        continuum=mean([mean_left mean_right]);
    end
    clear mean_left mean_right

    p_old=[100 0 0 0 100];
    x=data(:,2)/continuum;
    w=1./(data(:,3)/continuum).^2;

    xsquared=x.^2;
    wtimesx=w.*x;
    sum_w=sum(w);
    sum_wtimesx=sum(wtimesx);
    sum_wtimesx2=sum(w.*xsquared);
    Delta=sum_w*sum_wtimesx2-sum_wtimesx^2;
    for deltawave=-0.30:0.01:0.30
        for abundance=-1.0:0.05:1.0
            y=spectrum4500(Ind+floor(deltawave*100),floor(abundance*20+22));
            p_new(2)=(sum_wtimesx2*sum(w.*y)-sum_wtimesx*sum(wtimesx.*y))/Delta;
            p_new(1)=(sum_w*sum(wtimesx.*y)-sum_wtimesx*sum(w.*y))/Delta;
            if p_old(1)>abs(1-p_new(1))+abs(p_new(2))
                p_old=[abs(1-p_new(1))+abs(p_new(2)) -deltawave abundance p_new(1) p_new(2)];% correlation];
            end
        end
    end
    if abs(p_old(2))~=0.3
        output(stars,:)=[p_old(1) velshift p_old(2) abund p_old(3) R continuum_initial continuum {data}];% p_old(4) p_old(5)];
        stars=stars+1;
    end
end
toc

output(1)
output(2:3)
output(4:5)

figure(1)
clf
subplot(2,1,1)
hold on
plot(data(:,1),data(:,2)./continuum,'r.') %the data
% errorbar(data(:,1),data(:,2)./continuum,data(:,3)./continuum,'r.') %the data
plot(waves+p_old(2),spectrum4500(:,floor(p_old(3)*20+22))) %The fitted spectrum
plot(waves(Ind),spectrum4500(Ind-floor(p_old(2)*100),floor(p_old(3)*20+22)),'o')
plot(waves+velshift,spectrum4500(:,floor(abund*20+22)),'g--')
hold off
```

```
xlim([6480 6510])
ylim([0.5 1.05])
xlabel('Wavelength (angstroms)')
ylabel('Normalized flux')
box on

% figure(2)
% clf
subplot(2,1,2)
hold on
plot(x,spectrum4500(Ind-floor(output{3}(1)*100),floor(output{5}(1)*20+22)),'ro') %,data(:,3)./continuum
% plot(x,spectrum4500(Ind-floor(velshift*100),floor(abund*20+22)),'kx') %,data(:,3)./continuum
plot([0.5:0.01:1.05],[0.5:0.01:1.05],'g--')
xlim([0.5 1.05])
ylim([0.5 1.05])
hold off
xlabel('Data flux')
ylabel('Fitted spectrum flux')
axis square
box on
```

A.4 Function for creating simulated data

This is the function `fpidata.m`.

```
function [data velshift abund R continuum_initial]=fpidata(wavelengths,signaltonoise)

load('spec4500_45.mat')
waves=spectrum4500(:,1);
R=350*rand(1);
wavelengths=wavelengths/(sqrt(1+(R/22000)^2));
velshift=floor(25*randn(1))/100;
abund=floor(-20 + 40*rand(1))/20;

%This loop identifies the index number of the wavelength points

Ind=round((wavelengths-6482.21)/0.01 +1);

continuum_initial=signaltonoise^2+signaltonoise*rand(1,1);

x=spectrum4500(Ind,1)+velshift;
y=spectrum4500(Ind,floor(abund*20+22))+1/signaltonoise * (-1 + (2).*rand(length(wavelengths),1));%;+1/signaltonoise;% * (-1 + (2).*rand(length(wavelengths),1));
dy=continuum_initial/signaltonoise*(1+rand(length(wavelengths),1));
data=[x (1-y)*continuum_initial dy];
```